M M & S
M T
M C

By

Mátyás Benke

A C U
I P F R
D
D P

Cranfield University
Department of Aerospace Sciences
Cranfield, UK
September 2010

E ’ C

Mesoscale Modelling & Simulation of Macromolecule Transport in Microfluidic Channels

Mátyás Benke

September 7, 2010

CRANFIELD UNIVERSITY

School of Engineering

Ph.D. Thesis

Academic Year: 2009-2010

Mátyás Benke

Mesoscale Modelling & Simulation of Macromolecule Transport in Microfluidic Channels

Supervisors:

Prof. Dimitris Drikakis and Dr. Evgeniy Shapiro

Except where acknowledged in the customary manner, the material presented in this thesis is, to the best of my knowledge, original and has not been submitted in whole or part for a degree in any university.

Abstract

This thesis concerns the numerical simulation of dilute macromolecular solutions. Present work details the development of a novel mesoscale simulation method.

The developed modeling approach is capable to describe both the macroscopic flow field of the carrier liquid and the micromechanical behaviour of the transported large molecules. In this modeling method, the concept of micromechanical structures is introduced in order to represent macromolecules. The motion of the considered mechanical structures is governed by forces arising from the motion of the bulk fluid phase and microscopic forces arising from stochastic Brownian motion of the solvent molecules.

This document presents the motivation, the objectives and systematic steps of the model development. The work presents detailed discussion, verification and validation of the developed modeling method.

Acknowledgements

First and foremost, I am very grateful to my parents, my brother Martin, my whole family and my friends for their continuous support and encouragement throughout the duration of my Ph.D. It is really hard to express my appreciation and gratitude to them. I am afraid words are hardly enough.

I am extremely grateful to my supervisors, Prof. Dimitris Drikakis and Dr. Evgeniy Shapiro for their conscientious, honourable and hard work to keep me on the right track. I am very thankful for the fruitful conversations, the productive arguments and the constructive criticism. I really appreciate the countless inputs, recommendations, the continuous guidance and the considerable amount of time devoted to help me. Many thanks for challenging my ideas, providing objective judgements, performing sanity-tests and pointing me in the right direction.

Special thanks to Dr. Evgeniy Shapiro for his enthusiastic work, patience, supportive suggestions and general guidance he has given me, as well as his company and friendship. He has always been there when I needed help or guidance.

The financial support from DINAMICS EU project (Project: DINAMICS, NMP4-CT-2007-026804) is highly appreciated.

And last, but not least, I would like to thank all of my colleagues and friends who turned these past years into quite an experience. Many thanks

to Angela Sutherland and Dr. Laszlo Konozsy for the countless chats, discussions and the encouragement throughout these years. Deepest gratitude to Marjorie and Tom Nagy for their friendship and their support in times of need. Many thanks to Chris, Vicky and Martin Tebbs for improving the quality of this work. Special thanks to Dr. Vladimir Titarev for his company and his friendship, not to mention his short lectures on the history of Russian aviation, the Red Army and the great battles of World War II.

My deepest gratitude to all of my Cranfield friends, who turned the sad moments into pure sarcasm in "Cranfield Mental Hospital". Their "always-up-for-a-smile" attitude and their cleverly twisted humour created a truly unique atmosphere, which helped me through the sorrowful periods and the hardest times. I will never forget the countless night-shifts I have spent debugging F90 codes with a cup of coffee, accompanied with Ioannis in the next office fighting his own war with another code. Also, I will never forget the good times we had watching South Park episodes, discussing abstract physics, space invasions or terra-formation of planets, or just happily 'shooting' each-other online, playing Urban Terror.

Great thanks to the following guys: Ioannis W. Kokkinakis, a.k.a. "El Bastardo", Massimo Lai, a.k.a. "Le Chef", Max Starr, a.k.a. "Mad Max", Marc Spiller, a.k.a. "The German Guy", Pierre Jameson, a.k.a. "Peter Pan", Filipe Inok, a.k.a. "P. Pirata", Mathis Dahlquist, a.k.a. "The Viking", Kostas Karantonis from Lesbos, Ben "Kenobi" Obadia, Klementina Gerova, a.k.a. "Kleo", Zeshan Malick, Nicholaos Asproulis, Philip Barton, Marco Hahn "Solo", Sanjay Patel, Ben Thornber, Bowen Zhong, "The Kebab-King" and the friendly staff of Mitchell Hall.

Contents

List of Figures

Abbreviations

Acronyms

MEMS	Micro-Electro-Mechanical Systems
RF MEMS	Radio Frequency Micro-Electro-Mechanical Systems
MNFD	Micro- and Nanofluidic Devices
POC	Point Of Care
DNA	Deoxyribonucleic Acid
RNA	Ribonucleic Acid
dsDNA	Double-Stranded DNA
ssDNA	Single-Stranded DNA
AC	Alternating Current
DC	Direct Current
MD	Molecular Dynamics
CM	Continuum Mechanics
BD	Brownian Dynamics
CFD	Computational Fluid Dynamics
HSI	Hybrid Solution Interface
EBT	Embedding Based Techniques
EFA	Equation Free Approach
FJC	Freely Jointed Chain
WLC	Wormlike Chain
PET	Polymer Ensemble Transformation
WLC-PET	Wormlike Chain with Polymer Ensemble Transformation
CB	Characteristics-Based

Greek Symbols

ξ, η, ζ	coordinate directions
ν	kinematic viscosity
η	dynamic viscosity
ρ	density
ε	strain rate
τ_{xx}	viscous stress tensor component
$\boldsymbol{\omega}$	angular velocity
ϱ_{wall}	slip length
τ_{diff}	diffusion time scale
τ_{flow}	flow time scale
δ_0	distance from channel wall
δ_i	interval length
λ	molecular free path
τ_1	longest relaxation time
τ_i	mode relaxation time
λ_p	persistence length
λ_p^{eff}	effective persistence length
ζ_{coil}	drag coefficient of a coil
ζ_{rod}	drag coefficient of a rod
χ	number of persistence lengths in a spring
γ	inverse phenomenological relaxation time
$\boldsymbol{\phi}$	sum of all non-hydrodynamic forces
$\boldsymbol{\varphi}$	Brownian force

β	artifitial compressibility parameter
$\lambda_{0,1,2}$	eigenvalues of hyperbolic systems
Λ	metric coefficient
τ	pseudo-time
$\Delta\tau$	pseudo-time step
ϑ	transformed time
δ_ϵ	smoothed Dirac function
ϵ	length scale of the Dirac function
Φ	force transfer function
σ	Brownian force amplitude
σ_v	Brownian velocity amplitude
σ_x	Brownian displacement amplitude
δ	variance of a distribution function
$\sigma_{n,n-1}$	bond deviation for bead $n-1$ and n
$\lambda_{n,i}$	parameter for constraint force
ϵ	under-relaxation factor
α_{ij}	angle between bond i and j
$\Delta\alpha$	average angular displacement

Latin Symbols

Re	Reynolds number
Kn	Knudsen number
De	Deborah number
Pe	Peclet number
Ar	ratio of channel height to length
t	real time
m	mass
Δt	real time step
p	pressure
Δp	pressure drop
T	temperature
k	spring coefficient
k_B	Boltzmann's constant
x, y, z	spatial coordinates
$\Delta x, \Delta y, \Delta z$	cell dimensions
u, v, w	velocity components
u_{bulk}	bulk velocity
u_{max}	maximum velocity
$u\|_0$	wall slip velocity
Q	volume flow rate
L	length scale
U	velocity scale
h_c	channel height
w_c	channel width
l_c	channel length

J	determinant of the transformation matrix
δV	elementary volume
s	artifitial speed of sound
u^*	nondimensional streamwise velocity component
v^*	nondimensional cross-stream velocity component
p^*	nondimensional pressure
L_{ssDNA}	length of a ssDNA molecule
L_c	contour length of a molecule
$d_{molecule}$	molecule diameter
R_g	radius of gyration
p_{helix}	helix pitch
r_i	spring length
D	diffusion coefficient
C	species concentration
a	rod/segment length
b	bead radius
F	force magnitude
$\mathcal{L}^{-1}$	inverse Langevin function
l	fully extended length of a sub-molecule
N	number of beads
N_s	number of springs
N_K	number of Kuhn steps
DL	bond elongation
DLN	normalised bond elongation
wf_i	weighting function
wx_i, wy_i, wz_i	weighting function components
Δd	average deviation from prescribed bond length
$\tilde{f}$	approximation function

$\boldsymbol{r}$	position vector
$\boldsymbol{f}$	force
$\boldsymbol{g}$	constraint force
$\boldsymbol{\mathcal{F}}$	volumetric force
$\boldsymbol{u}$	fluid velocity vector
$\boldsymbol{v}$	particle velocity vector
$\boldsymbol{n}$	unit normal vector
$\boldsymbol{F}^d$	drag force
$\boldsymbol{T}$	torque
$\boldsymbol{RHS}$	right-hand-side vector
$\boldsymbol{R}_{x,n}$	vector of random displacement components
$\boldsymbol{R}_{v,n}$	vector of random velocity components

$\mathbf{U}$	compact vector for pseudo-time part
$\mathbf{U}_r$	compact vector for real time part
$\mathbf{E}_{\mathrm{I}}^{\mathrm{C}}$	compact vector of inviscid fluxes along x
$\mathbf{F}_{\mathrm{I}}^{\mathrm{C}}$	compact vector of inviscid fluxes along y
$\mathbf{G}_{\mathrm{I}}^{\mathrm{C}}$	compact vector of inviscid fluxes along z
$\mathbf{E}_{\mathrm{V}}^{\mathrm{C}}$	compact vector of viscous fluxes along x
$\mathbf{F}_{\mathrm{V}}^{\mathrm{C}}$	compact vector of viscous fluxes along y
$\mathbf{G}_{\mathrm{V}}^{\mathrm{C}}$	compact vector of viscous fluxes along z
$\mathbf{F}^{\mathrm{C}}$	compact vector of volume force (Cartesian)
$\mathbf{E}_{\mathrm{I}}$	compact vector of inviscid fluxes along ξ
$\mathbf{F}_{\mathrm{I}}$	compact vector of inviscid fluxes along η
$\mathbf{G}_{\mathrm{I}}$	compact vector of inviscid fluxes along ζ
$\mathbf{E}_{\mathrm{V}}$	compact vector of viscous fluxes along ξ
$\mathbf{F}_{\mathrm{V}}$	compact vector of viscous fluxes along η
$\mathbf{G}_{\mathrm{V}}$	compact vector of viscous fluxes along ζ
$\mathbf{F}$	compact vector of volume force (Curvilinear)

Introduction

1 Introduction

This thesis concerns the numerical investigation of physical processes occurring in micro- and nanofluidic devices. Micro- and nanofluidics is a relatively new, but very promising and rapidly evolving branch of engineering sciences. It concerns the physical behaviour, the control and manipulation of liquids in devices with typical sizes on the sub-millimeter scales.

Present study is focused on phenomenon occurring on the domain of mesoscopic scales. The region of mesoscopic scales lies in-between the length scales comparable to the size of individual atoms and the typical macroscopic length scales describing systems comprising a large number of atoms or molecules.

The domain of mesoscopic scales is relevant to macromolecules with relatively intermediate sizes, for example polymers, enzymes, proteins,

DNA and RNA. Typical sizes of such large molecules is orders of magnitude larger than the usual atomic sizes and in many cases, length of the molecules is in the range of microns.

This work is aimed to describe the physics of large molecules in aqueous solutions. In such systems, the transported macromolecules are significantly larger than the solvent ones. This considerable length scale difference leads to various challenges when modelling the solvent-solute system.

The study discusses the transport, the micromechanical behaviour and the orientation of the studied long-chain molecules. The considered problems have extensive relevance in biology, life sciences and various biomedical and engineering applications.

1.1 Microfluidics in Everyday Life

Due to the fact that targeted scientific research related to micro- and nanofluidics is a relatively new branch of physical sciences, most engineers and scientists regard it as a new discipline. Although this statement is correct, practical micro- and nanofluidic applications are just as old as the first life forms on our planet.

Taking this thought further, let us consider the basic building block of a living organism, a cell. A cell is the smallest functional unit of life. The volume of a typical living cell is filled with cytoplasm, a water-based organic mixture. This solution acts as a medium for vital micro- and nanoscale processes related to living creatures. Nutrient transport, cell multiplication and a wide range of other fundamental micro- and nanoscale reactions related to living creatures occur in this aquaeous solution.

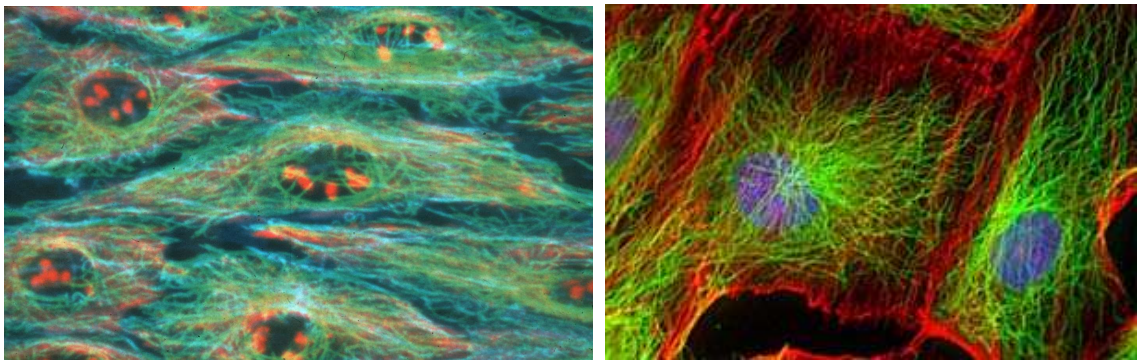

(a) Actin filaments and microtubes in cells[1] (b) Epithelial cells[2]

F 1.1: Images of human cells

[1] source: http://www.jacobsschool.ucsd.edu/uploads/news-release/2005/Cells.jpg
[2] source: https://nic.med.harvard.edu/gallery/Human%20Cells.jpg

Since relevant micro- and nanoscale reactions occur even on sub-cell level, it is accurate to state that every living organism exhibits cell, and even sub-cell level transport processes, chemical and biochemical reactions. Therefore, from the purely engineering aspect, living cells and more complicated life forms can be considered as organic microscale reaction chambers, literally, living microfluidic devices and systems.

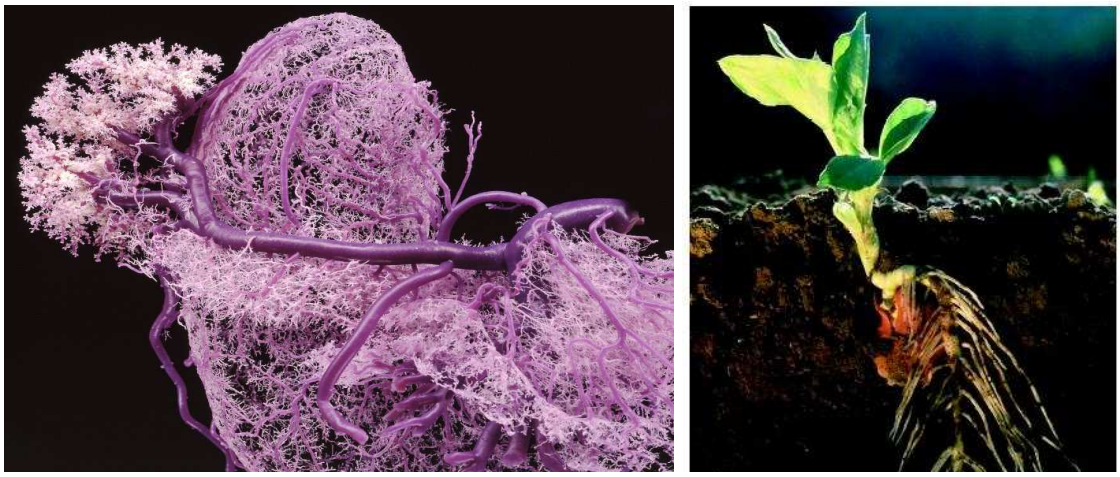

(a) Human vascular system[3] (b) Vascular system of a plant[4]

F 1.2: Natural microfluidic systems on larger scales

Let us consider biological systems on a slightly larger length scale. The vascular system of living organisms is an illustrative example of organic micro- and nanofluidic complexes. It is a complicated fluidic network consisting of pipes with varying diameter, a series of valves and a number of reservoirs.

The main purpose of this system is the fluidic transport of molecules and molecule complexes. However, the overall circulation system has other vital functions as well. Its alternative roles involve filtering, separating, mixing, adsorbing gases and incubating reactions. Again, vascular systems

[3]source: http://www.spiegel.de/images/image-35932-galleryV9-yquh.jpg
[4]source: http://www.biologyreference.com/images/biol_04_img0404.jpg

can be considered as complex microfluidic networks designed for specific tasks.

Apart from the examples taken from biology, practical microfluidics occurs in many simple forms and applications in our everyday life. As a matter of fact, these micro- and nanofluidic applications have already became parts of our lifestyle.

In order to list some items, one does not have to think about sophisticated high-tech devices in pharmaceutical companies and research labs. On the contrary, one should consider some of the most trivial everyday goods. When thinking about the simplest and cheapest examples, one should consider paper tissues, cotton buds and coffee filters.

However, more enhanced and more illustrative microfluidic systems can be found in consumer electronics goods and home-use medical devices. These devices are, for example liquid cooling systems for PC's, inkjet printers and blood glucose sensors.

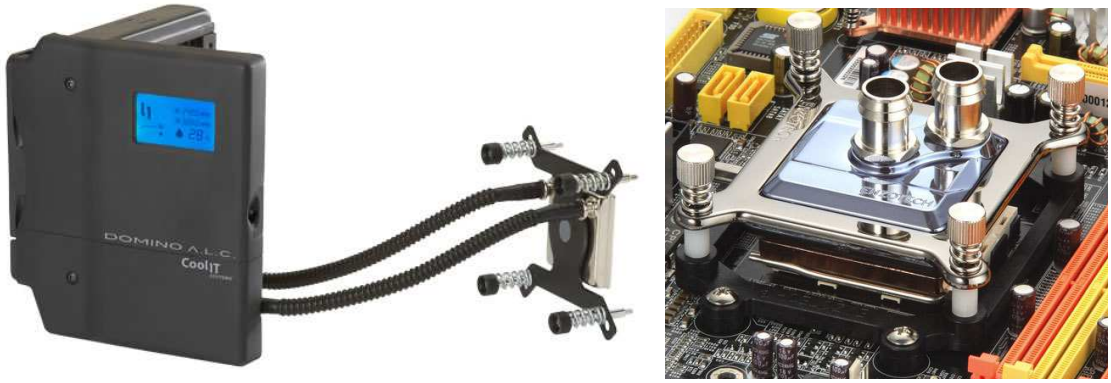

(a) "Cool-IT" commercial system[5] (b) Installed cooling unit on the chip[6]

F 1.3: Water cooling system for PC's

[5]source: http://hi-techreviews.com/Reviews_2009/Domino/Dom1.jpg
[6]source: http://www.techpowerup.com/img/07-08-28/sapphire_cpu_photo4.jpg

1.2 Background and Perspectives

In the past decades, scientific interest and strategical research was strongly oriented towards micro- and nanoscale technologies. Recent developments in micro- and nanoscale manufacturing techniques facilitated rapid evolution of small scale devices.

As a result of the invested resources and efforts, a new branch of engineering, Micro-Electro-Mechanical Systems (MEMS) technologies have started to materialise. MEMS are cutting-edge systems, based on high-precision microfabricated components, such as sensors, actuators, pumps, microchannels and microvalves.

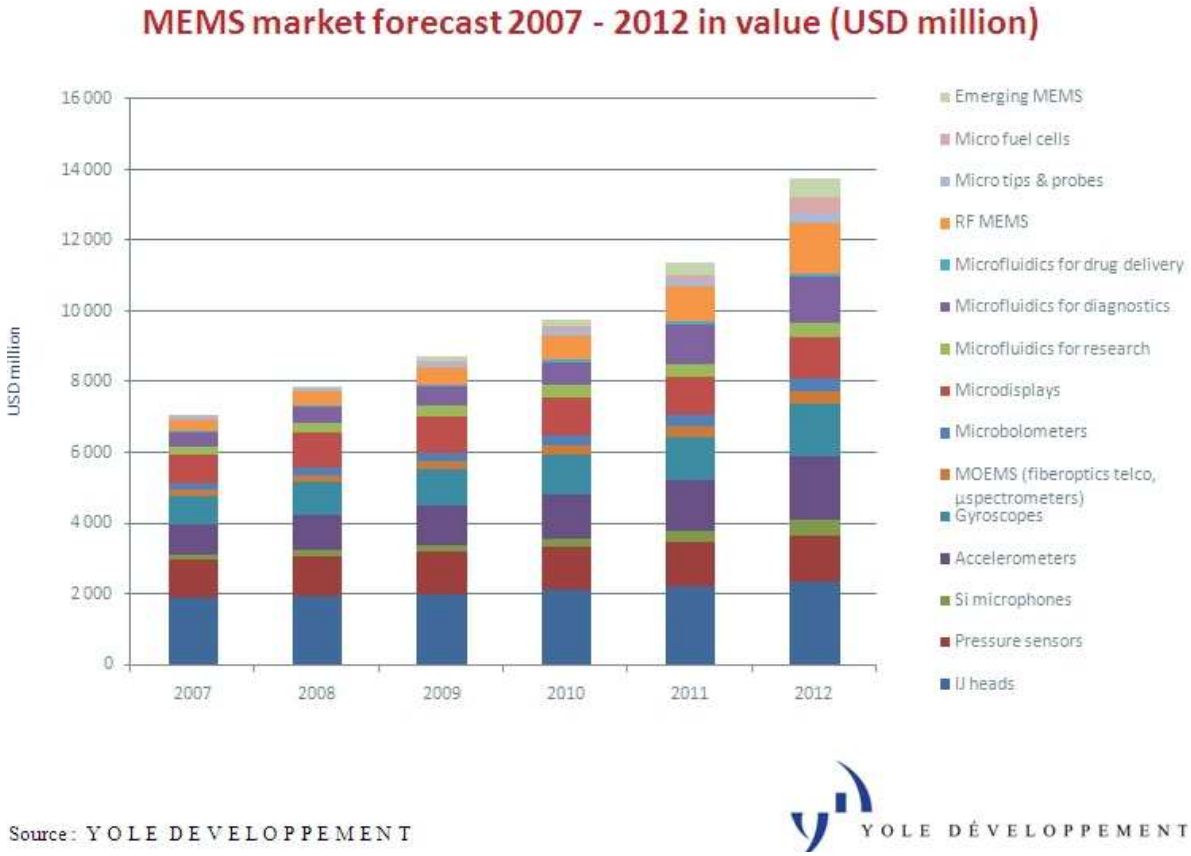

F 1.4: Estimation of MEMS market by Yole Développement[7]

[7] source: http://www.i-micronews.com/upload/Interviews/MEMS%20vol.jpg

Due to the moderate manufacturing costs and the extensive capabilities lying in these technologies, the market for such devices is rapidly increasing. As a recent market research by Yole Développement shows (Fig. 1.4), MEMS market has grown rapidly between 2007 and 2010, from ~$7 B to ~$10 in only 3 years time. According to their estimation, the market will reach ~$14 B by 2012, doubling itself in merely 5 years.

The major segment of the market is covered by the inkjet applications, with a balanced demand over the years. However pressure sensors, accelerometers and microdisplays also represent a considerable and steady fraction. The most rapidly emerging MEMS applications are microfluidic devices for diagnostics and RF MEMS, radio-frequency based applications.

1.3 Fluidic Applications

Amongst the large variety of newly developed micro- and nanosystems, micro- and nanofluidic devices (MNFD) represent a major segment.

The application of micro- and nanofluidic devices covers a wide range of disciplines, including chemistry [3–5], biology [6–8], engineering [8–10] and life sciences [11, 12]. Typical applications include heat-exchangers [13–15], particle separators [7], bubble separators [9, 10], chemical reactors [16], filters [17], analysis and detection systems [11, 12, 18, 19], point-of-care (POC) devices, drug delivery systems [20, 21] and micromixers [5, 22].

These small scale devices offer significant advantages compared to the macroscopic ones. The main benefits are improved accuracy, enhanced process- and reaction control, reduced sample volumes and analysis times. Microscale devices also offer unique functionalities, which are simply impossible to achieve by macroscopic systems.

Shrinking device dimensions provides the ability to investigate fundamental processes occurring on microscopic scales. Microtechnology allows us to study single molecules, analyse the structural changes of biopolymers and measure the elastic response of macromolecules. The revolutionary features and the numerous benefits of microscale systems make them especially advantageous for micro-reactors, bio-analysis and detection technologies.

Design of bio-detection systems is mainly focused on the recognition of hazardous biological/biowarfare agents such as bacteria and viruses. Based on the available technologies, these organisms can be detected in various media (air-borne or water-borne agents) [6, 23, 24].

1.4 Aims and Objectives

The aim of the thesis is to investigate computational methods and models for the controlled transport of DNAs through channels. During our research, microchannel transport of DNA strands was investigated using numerical simulation.

Computational modelling is a powerful and cost-effective research tool to support engineering design. In many cases, numerical modelling is performed in order to guide functionality-oriented design and prove design concepts. Simulation of the fundamental processes aids the understanding of device operation and provides accurate estimation of performance. Considering the wide range of length- and time scales involved, accurate description of the phenomenon required the application of novel multi-scale methods.

The purpose of this Ph.D. work was to develop, validate and utilise efficient numerical tools to model the transport of large molecules in microchannels. The topic raises a number of challenges, which are mainly originated from the inherently multi-scale nature of the problem. The numerical model should be able to capture fine scale physics of the investigated macromolecules, without prohibitive computational requirements. On the other hand, the modelling method should be able to consider the effect of the macroscopic flow field of the carrier liquid on the transport process.

The objectives of the performed research work can be identified as:

- Develop an efficient modelling approach to describe the behaviour of macromolecules on mesoscopic scales, especially focusing on transport and micromechanical behaviour.
- Verify and validate the applied modelling tool against available experimental data.
- Investigate micromechanical behaviour of ssDNA and dsDNA molecules, concerning microfluidic transport, extension and relaxation processes.

1.5 Review of Microscale Phenomenon

Development of realistic models requires understanding of the fundamental physics, identification of the dominant effects and careful consideration of the parameter ranges.

Micro- and nanofluidic research is aimed to investigate processes relevant to gases and liquids on the microscopic scales. Based on rational considerations, scales of the applied devices should match the scales of the studied phenomenon. This section is aimed to briefly summarise the consequences of decreasing device dimensions below the millimeter scales.

Focusing on microfluidic devices, typical length scales are around a few micrometers. Therefore, surface-to-volume ratio of such devices is large compared to the macroscopic ones. Length scale is a significant factor during the identification of dominant forces relevant to the investigated physical phenomenon.

Estimation of fluid forces shows that decreasing the length scale significantly reduces the magnitude of volume forces, since they scale with L^3. Surface forces scale with L^2, therefore their drop is moderate compared to the volumetric ones. As a result of decreasing length scales, the relative importance of surface forces increases compared to the volumetric ones [25]. The increasing significance of surface forces in microfluidic devices results unique requirements regarding the fluid transport techniques.

Considering typical microchannels, the practically achievable flow rates are pico- or nanoliters per hours. Such slow flows are often referred as "creeping flows" or "Stokes flows". The typical flow rates and the concerning length scales indicate moderate Reynolds numbers in general ($Re <\sim 10$). This nondimensional parameter shows the ratio of inertia and viscous

forces:

$$\mathrm{Re} = \frac{UL}{\nu},$$

with U characteristic fluid velocity, ν kinematic viscosity of the fluid and L characteristic length scale (channel height, for example). Small Reynolds numbers ($\mathrm{Re} < 1$) indicate the dominance of viscous forces over the inertia effects.

Decreasing the dimensions of the confining geometry may also result in different physical behaviour of the investigated fluid. The effects of reducing the length scales have been extensively detailed by Karniadakis *et al.* [26]. The authors pointed out that shrinking the channel size below a critical limit leads to the breakdown of the continuum theory. When continuum models fail to describe the relevant physical processes, the application of atomistic models must be considered.

1.5.1 Microscale Behaviour of Gases

When investigating gases, the flow becomes rarefied as the length scales shrink below the limit [26]. In order to determine the validity of the continuum approach for the given gas flow problem, the Knudsen number must be considered. The parameter represents the relationship between characteristic length scale and mean free path of molecules:

$$\mathrm{Kn} = \frac{\lambda}{L}.$$

Here, λ is the molecular mean free path which is the measure of molecular collision intensity. Based on the Knudsen number, the following flow regimes and valid models can be defined for gases:

$1 < \mathrm{Kn}$	Molecular Dynamics (MD) approach
$10^{-1} < \mathrm{Kn} < 1$	Transition / Continuum approach
$\mathrm{Kn} \sim 10^{-2}$	Continuum approach with slip boundary
$\mathrm{Kn} < 10^{-2}$	full Continuum Mechanics (CM) approach

1.5.2 Microscale Behaviour of Liquids

Focusing on microscale phenomenon related to liquids, the most significant observation is the granular behaviour, when decreasing the length scales below the limit [26]. Apart from the granular effects, anomalous diffusion, wall slip, dramatic changes in wetting and adsorption properties can be observed as well.

Megaridis [27] carried out systematic experiments in order to investigate the physics of fluids in channels with consistently reduced sizes. Their experimental observations clearly indicated the existence of a stable and continuous liquid meniscus separating the fluid from the confining gas bubbles in channels with approximate diameter of $\sim$ 80 nanometers [26]. However, reducing the pipe diameter with an order of magnitude, the fluid interfaces become instable, and the molecules apparently form long clusters.

The authors have concluded that the continuum model for liquids is valid down to the approximate channel size of $\sim$ 50 nanometers [26]. Consequently, continuum hypothesis is valid for the micro- and mesoscopic scales and starts to break down on the nanoscales in case of liquids.

1.5.3 General Microscale Effects

On the usual macroscopic scales, phenomenon like capillarity, surface tension, Van der Waals, Columbic and steric forces are negligible. These forces however, have significant effects on the micro- and nanoscales [25]. The listed interactions are different appearances of intermolecular forces. Although such phenomenon are short range interactions ($L < 1\,\text{nm}$), their effect is sensible on longer lengths scales as well ($L > 0.1\,\mu\text{m}$).

Macroscale behaviour of fluid-solid interfaces is mainly governed by the surface topology. While on the micro- and nano scales, fluid-solid interactions and contact effects are governed by intermolecular forces. Depending on fluid-surface material combinations, strong hydrophobic and hydrophilic fluidic behaviour can be observed on such small scales. These effects can be amplified or weakened using additional electric charges.

Strong hydrophobicity leads to apparent slip on microchannel walls. Therefore, applicability of the widely used "rule of thumb" no-slip wall boundary condition must be revised. When slip occurs, one should utilise the general wall boundary condition proposed by Navier [28]:

$$u|_0 = \varrho_{wall} \left(\frac{dv}{dy} \right) \Bigg|_{y=0}$$

with ϱ_{wall} slip length.

Wall slip effect must also be accounted during the calculation of the volume flow rate. Consider for example the incompressible flow through a high aspect ratio channel of height h_c, width w_c and length l_c, according to wall slip velocity of $u|_0$. Solution of the governing momentum equations

yields the flow rate Q for the applied pressure drop Δp along the channel:

$$Q = \underbrace{\frac{2w_c h_c^3}{24\eta}\frac{\Delta p}{l_c}}_{Q_{Poiseuille}} + \underbrace{h_c w_c u|_0}_{Q_{Slip}}$$

Wall slip phenomena has been observed by a number of researchers [29–31]. Some of them investigated the nature of the phenomena. Ruckenstein [32] for example, suggested that slip does not occur directly at the solid surface, but over a gap which could be generated by soluble gases. De Gennes [33] postulated the formation of thin, continuous gas films on channel walls. Lagua and Stone [34] observed nano size bubbles formed on the wall and Tretheway [35] suggested that slip develops from depleted low density fluid or vapour region formed close to the solid surface.

Although the exact nature of fluid slip is still not fully understood, the resulting effects must be considered when prescribing boundary conditions for numerical calculations.

1.6 Microchannel Flow Driving Techniques

Manipulation and control of microfluidic flow rates raises specific problems and requirements compared to macroscale devices. Usual total volume of microchannels is relatively small and depending on molecular forces acting between solid surfaces and the fluid, hydrodynamic resistance can become considerable.

Therefore, improvement of common pumping methods and consideration of alternative fluid driving forces is necessary. A large variety of available effects (pressure, capillarity, surface tension, electric, magnetic, magnetohydrodynamic, piezo, centrifugal forces, etc.) can be successfully adapted solely, or in various combinations [10, 11, 36].

Electrokinetic fluid transport is a completely new phenomena developed specifically for microfluidic applications. This alternative flow driving concept offers several varieties. In case of electro-osmosis, the polarisable fluid moves due to the streamwise variation of the stationary wall charge.

During dielectrophoresis, an interface (often formed by solid particles) is forced to move by electrostatic gradient. It is known that electric field modifies wetting properties of solid surfaces. If the flow is generated due to electrically modified wetting properties of surfaces, electrowetting occurs.

Amongst the mentioned electrokinetic flow driving mechanisms, electro-osmosis is the most common technique. It is easy to control and it can provide continuous fluid transport. The phenomena is characterised by the presence of the electrical double layer (EDL) formed on the solid-liquid interface. The applied surface charge is shielded by soluble counter-ions from the fluid. Fluid motion is generated by ion drag upon application of tangential electric field, which drives the motion of counter-ions.

The resulting velocity field varies rapidly in the relatively thin electric double layer, but uniform outside this region [37]. Besides the flow transport applications, AC and DC electro-osmosis is a very effective technique to separate and collect polarizable particles from the surrounding fluid [38–40].

Although electrokinetic pumping methods offer various advantages, these flow driving mechanisms can only be applied in electrically compatible systems. Considering systems where introduction of electric fields is permitted, alternative flow driving techniques must be utilised. In such cases, mechanical pumps provide a possible solution.

Microfluidic pumps differ from conventional ones in several aspects. Their aim is to provide extremely small flow rate with high precision. Amongst the traditional constructions, injection and syringe pumps can be used for microfluidic applications.

Recently, Auroux *et al.* [11] and Stone *et al.* [10] revised a large variety of new ideas. The reported pumping methods included magnetohydrodynamic systems, pumps operated with maintained hydrostatic pressure difference between the inlet and outlet reservoir and devices pumping by growing and collapsing bubbles. Syringes operating with magnetically activated ferrofluid plugs and centrifugal pumping with microchannels attached to spinning disks are also functional constructions. Capillary-based self-filling devices and peristaltic pumps based on local collapse of the flexible channel are also achievements of microfluidic technologies [9, 10].

As the presented brief overview of microchannel pumping methods demonstrate, the reduction of channel sizes resulted in a number of innovative engineering solutions and flow driving mechanisms.

In order to choose the most suitable flow transport method for a given problem, operation of the whole system as one functional unit must be considered. During the design process, restrictions and requirements arising from the applied technologies and conditions determined by the connected sub-units must be considered.

1.7 Parameter Analysis of the Problem

The following section provides the parameter study of the considered microchannel transport process. Aim of this section is to determine the operating conditions and give a rough estimation of the concerning length- and time scales involved. Detailed investigation of the relevant parameters will allow us to define the most suitable modelling approach to describe fundamental processes - mainly different varieties of transport - occurring in the channel section.

From the beginning of the research, main objective was to identify predefined substances present in the carrier liquid. Therefore, the system must be able to sense molecules in extremely dilute solutions. In such cases, solute material content cannot be defined as a *concentration field*, but rather referred as *number density* of the diluted material present in the solution. This extreme requirement governs the development of the applied modelling methods.

1.7.1 Flow Field

Following the initial design considerations, high aspect ratio channels are favoured. This requirement is defined by the preferred manufacturing technology of the microchannels. According to the first estimations, width of the channel section is approximately $w_c = 2\,\text{mm}$ and the height of the channel is around $h_c = 100\,\mu\text{m}$.

Based on the preliminary information about the flow regimes provided by our partners, the bulk velocity is in the range of $u_{bulk} = \left[5.0 \cdot 10^{-4} - 2.5 \cdot 10^{-1}\,\text{m/s}\right]$. Considering 2-D laminar channel flow, this results the maximum velocity in the region of $u_{max} = \left[7.5 \cdot 10^{-4} - 3.75 \cdot 10^{-1}\,\text{m/s}\right]$. Assuming that the flowing fluid is drinking water with constant viscosity

of $\nu = 10^{-6}\,\mathrm{m}^2/\mathrm{s}$, the Reynolds number range based on channel height and maximum flow velocity is as follows:

$$\mathrm{Re} = \frac{u_{max}\, h_c}{\nu} = 0.075 - 37.5. \tag{1.1}$$

This results laminar flow in the microchannel for the whole range of operating velocities.

According to the manufacturer's preferences, syringe pumps are favoured to drive the working liquid. This pumping method will result steady pressure-driven flow. Considering the necessary functionalisation of the microchannel walls, strong hydrophilicity of the surfaces will be assured.

Due to the wetting properties resulting from the liquid-surface material combination, no-slip wall boundary condition is appropriate when performing numerical simulations of the investigated problem. Considering fully developed channel flow with uniform, high aspect-ratio rectangular channel cross-section, parabolic velocity profile and linear shear-stress distribution with maximal shear stresses at the walls is predicted.

Since final operating parameters of the pre-processing unit are not decided yet, no information is available regarding the distribution of molecules entering the considered channel section.

1.7.2 Length Scales

Considering the necessary sample preparation steps prior the investigated channel section, the substances present in the microchannel are fragments of single-stranded DNA (ssDNA) molecules with the length of 1400 – 2000 nucleotides.

Taking the unit nucleotide length of 6.3 Å, typical length range of the fractions is $L_{ssDNA} = [882 - 1260\,\text{nm}]$. The length of the investigated molecules compared to the channel height is $L_{ssDNA}/h_c \approx 0.01$, relatively small. Figure 1.5 demonstrates the sketch of the concerning microchannel dimension and the approximate relative size of a transported ssDNA strand.

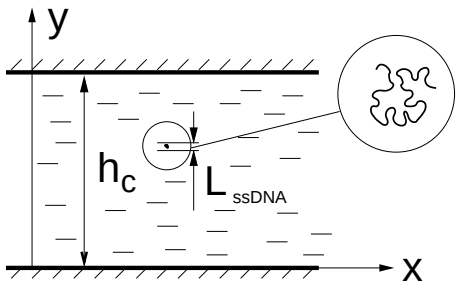

F 1.5: Approximate dimension of the channel and the considered ssDNA strand

1.7.3 Time Scales

Now we focus our interest on the time scales involved in the processes occurring in the detector section of the microchannel.

Fundamental processes are transport of ssDNA strands and base-pairing reactions. Investigating molecule transport, atomic motion of small solvent molecules has a typical time scale of $\sim 10^{-12} - 10^{-9}$ seconds, while fine scale motion of ssDNA strands - involving conformational changes - can be described on the scale of $\sim 10^{-9}$ seconds.

Brownian motion of large molecule segments involves time scales of $\sim 10^{-6}$ seconds. Figure 1.6 demonstrates the concerning approximate time scales of motions.

Focusing on the DNA reactions, estimation of time scales is more challenging. Although the phenomena is not fully understood, experimental

results of Chung [41] suggests that DNA base-pairing reactions require approximately some seconds, or even minutes.

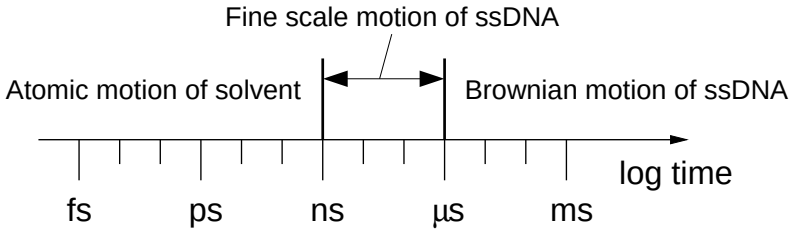

F 1.6: Characteristic time scales of different processes

1.7.4 Transport Mechanisms

Mobility of macromolecules in solutions can be characterised by the diffusivity of the molecule. According to empirical relations confirmed by diffusion experiments [42], DNA diffusion coefficients can be derived as:

$$D = 4.9 \cdot 10^{-6} \cdot [bpsize]^{-0.72}\,\mathrm{cm}^2/\mathrm{s} \tag{1.2}$$

Taking the DNA size as 2000 nucleotides, the calculated diffusion coefficient is $D = 2.058 \cdot 10^{-12}\,\mathrm{m}^2/\mathrm{s}$.

Once the value of the diffusion coefficient is known, it is possible to estimate the associated timescale. The governing equation for the single species concentration C and spatially constant binary diffusion coefficient D is given by

$$\frac{\partial C}{\partial t} \sim D\frac{\partial^2 C}{\partial x^2} \tag{1.3}$$

Applying dimensional analysis to the above equation, it is possible to estimate the order of magnitude of diffusion time τ_{diff} as

$$\tau_{diff} \sim \frac{h_c^2}{D}, \tag{1.4}$$

where h_c is the characteristic length of diffusion given, for example, by the microchannel height.

On the other hand the characteristic time of the flow motion in a microchannel with length l_c and bulk velocity u_{bulk} is given by

$$\tau_{flow} \sim \frac{l_c}{u_{bulk}}. \tag{1.5}$$

The ratio of flow diffusion timescale to flow timescale is then given by

$$\frac{\tau_{diff}}{\tau_{flow}} = \frac{h_c^2\, u_{bulk}}{D\, l_c} = \frac{h_c\, u_{bulk}}{D}\frac{h_c}{l_c} = \mathrm{PeAr} \tag{1.6}$$

where $\mathrm{Ar} = h_c/l_c$ is ratio of channel height to length and $\mathrm{Pe} = h_c\, u_{bulk}/D$ is the Peclet number measuring the relative importance of convection in comparison with diffusion.

Estimating the ssDNA diffusion coefficient at $\sim 2 \cdot 10^{-12}\,\mathrm{m}^2/\mathrm{s}$ [42], we can estimate, in the order of magnitude, the length of a straight microchannel in terms of the microchannel height necessary for the ssDNA sample to spread throughout the channel cross-section

$$\frac{l_c}{h_c} = \mathrm{Pe} = \frac{h_c\, u_{bulk}}{D} = \frac{100 \cdot 10^{-6}\,[0.5 - 250] \cdot 10^{-3}}{2 \cdot 10^{-12}} = [0.25 - 125] \cdot 10^5. \tag{1.7}$$

The analysis indicates that during a given time interval, the convective mechanism transports the ssDNA molecules five orders of magnitude further than the diffusive mechanism.

Let us consider the main transport mechanisms in both cross-stream and stream-wise directions. Cross-stream molecule transport is governed only by molecular diffusion and stream-wise motion is dictated by the dominating convection.

Considering transport directions, timescale analysis results that a minimum channel length of $l_c \approx 10\,\mathrm{m}$ is necessary for the molecules to diffuse across the channel height of $h_c = 100\,\mu\mathrm{m}$, starting from the opposite wall.

1.8 Overview of Modelling Approaches

The following section is intended to give a brief overview of the available modelling methods. In the discussion, advantages and drawbacks of the considered approaches are analysed, in regard to the considered microchannel transport problem. Review of the methods allowed us to identify the most suitable modelling approach to describe fundamental processes occurring in the investigated detection section.

Since the first attempts to describe physical processes, a variety of refined modelling techniques have been developed. The aim of the developed techniques is to capture processes occurring on a limited range of pre-defined length and time scales. However, construction of models capable of dealing with multi-scale phenomenon represents a real challenge [1, 26, 43].

Considering the common simulation tools, it is possible to identify two main streams of modelling methods. Both of them can be utilised to describe transport processes in MNFDs, based on the length scales separation.

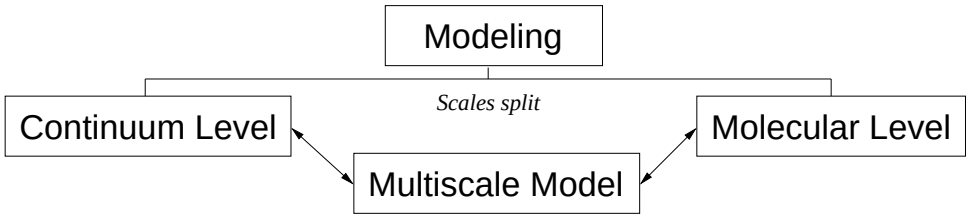

F 1.7: Main branches of modelling microchannel phenomenon

The first alternative is the *continuum level modelling*, based on the Navier-Stokes system of equations with additional models describing the sample transport. The other option is the *molecular level modelling*, based on the equation of motion of individual particles in the flow.

The choice of the most suitable approach depends on the characteristic length scale of the flow and the level of detail required from the physical model (see for example, [1, 26, 43]).

1.8.1 Continuum Level Models

Continuum models are widely used to describe macroscopic behaviour of systems. However, application of the approach is not limited to macro-scale systems, since continuum models are often used to determine hydraulic characteristics of microfluidic devices [26, 43]. Due to the significant enhancement of numerical methods in the past decades, continuum-based modelling has become a reliable and time-efficient simulation tool [1].

The approach assumes that the studied fluid fills out the available space continuously. As a direct consequence, fluid properties can be described by continuous functions of space and time. Due to the characteristic time ($\sim$ 1 s) and length ($\sim$ 10^{-2} m) scales of the approach, continuum models average fine time- and length scale processes. Therefore, fundamental phenomenon occurring on finer scales can only be resolved in statistical sense.

Although continuum assumption is suitable for a variety of microchannel applications, the model screens out small time- and length scale processes. Since phenomenon occurring on microscopic scales are not resolved properly, the model alone cannot fully predict fine scale phenomena. Moreover, the simple Eulerian continuum approach is unable to describe the transport of solute material with low number densities, which usually occurs in separators and detection systems.

1.8.2 Atomistic Models

In the case when continuum models cannot fully capture the fine scale physics of a system, *molecular level models* have to be considered. Atomistic models provide detailed description of processes on the characteristic scales of $\sim 10\,\text{nm}$ in space and $\sim 10^{-9}\,\text{s}$, in time. Pure molecular models are based on the solution of Newton equations of motion written for individual particles.

The acting forces are resulted from pre-defined inter-molecular potentials. Solution of the Newton equations of motion is obtained by numerical integration of the governing equations for molecular positions. Despite the apparent simplicity of the model, calculations are extremely demanding computationally. The main shortcoming of molecular models is their high computational cost, which restricts their application to simulations of nanoscale system for very short time periods.

In order to reduce the computational requirements, various modelling alternatives have been developed within this modelling framework. When investigating a system comprising large number of molecules with various sizes, small molecules can be treated implicitly, rather than modeled individually. Since the concerning small molecules are usually the solvent ones, this method is known as "implicit solvent" technique.

The main idea of the implicit solvent approach is the individual description of large molecules, considering only the effects of the small ones. Although the implicit solvent approach decreases the computational requirements in terms of memory usage, the computational times are similar to the all-atom models.

An alternative solution to reduce computational times is to increase simulation time steps. This can be achieved by various coarse-graining methods. Such methods are sophisticated transformations applied to simplify all-atom models of large molecules. Depending on the level of coarse-graining, several atoms or groups of atoms are encapsulated into a model unit.

During the coarse-graining process, the superposition of atomic potentials must be assigned to the concerning units. The units of the simplified model are usually represented as beads with the concerning mass.

Coarse-graining of all-atom models of large molecules usually results bead-rod or bead-spring representations. Small molecules - usually the solvent - can be treated implicitly or explicitly as well. The application of coarse-grained models of large molecules, in combination with the implicit treatment of the solvent resulted the Brownian Dynamics modelling method (see e.g. [44]).

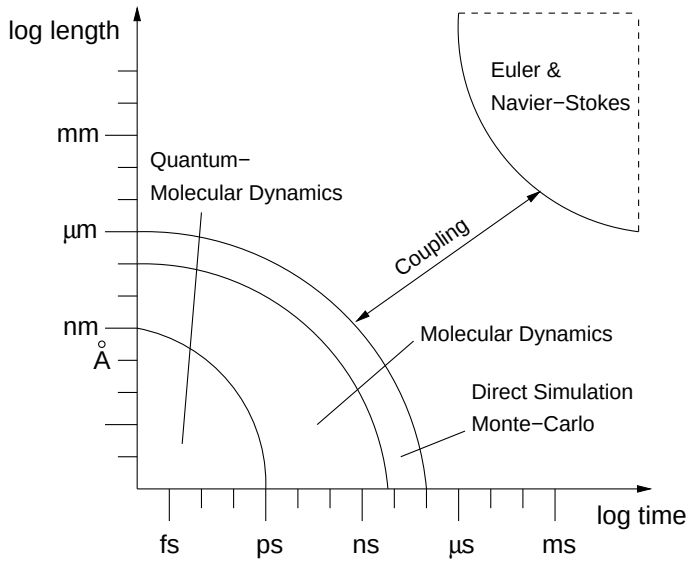

F 1.8: Applicability of models in terms of length and time scales (adapted from [1])

1.8.3 Multiscale Methods

Standard modelling techniques are designed to capture phenomenon occurring on a limited range of time and length scales. Obviously, processes arising on scales outside the applicability region of the given method, are not captured.

The general continuum-level description has been developed to model processes on the domain of macroscopic scales, therefore this approach is unable to capture fine scale microscopic effects. On the other hand, atomic level models provide detailed description of fine scale phenomenon, but the method is inefficient to describe processes on the macroscopic scales.

Due to the limitations of the classical continuum and the inefficiency of the atomic level models, scales between the typical "macro" and "micro" region are not captured accurately. Driven by the attempt to describe phenomenon on these intermediate scales, simulation methods involving multiple scales have been developed.

The most popular approach to unite the description of various scales is the family of *multiscale methods*. The aim of multiscale methods is to couple the microscopic and macroscopic descriptions of the investigated system. The idea of the approach is the combination of essentially segregated descriptions of length and time scales into one modelling tool.

The developed methods are based on the simultaneous application of molecular and continuum level models in pre-defined spatial regions of the computational domain. Local fine scale representation of fundamental processes avoids limitations of pure molecular models.

The resulting combined simulation tool is suitable to describe processes relevant to both macroscopic and microscopic scales. The dual modelling

approach necessitates information exchange between the models. The two-way information exchange between the molecular and continuum domains is achieved through a hybrid solution interface (HSI) connecting the corresponding interfaces.

Hybrid MD-continuum methods provide a unifying description of liquid flows from the nano scales to larger scales. The hybrid methods can be broadly classified into three groups: domain decomposition techniques, embedding based techniques (EBT) and the equation free approach (EFA).

Although multiscale models based on combined micro-macro calculations are widely used, the technique does not result in essential coarse-graining of microscopic scales.

1.8.4 Meta-Modelling

This section is aimed to introduce and discuss a novel modelling approach, first published by Trebotich *et al* [45] and improved and extended in the frame of present Ph.D. work.

The considered modelling method aims to describe mesoscale behaviour of large molecules, such as single-stranded DNA, double-stranded DNA, and various long-chain polymers. In order to enlight the novelty of the approach, brief discussion of the relevant mesoscale modelling methods is carried out.

In the previous section, various multiscale modelling techniques have been introduced. These aim to combine the atomistic and continuum descriptions. As a result, multiscale methods suffer from the limitations on time steps induced by the scale decoupling.

Mesoscale models on the other hand, aim to address not only the interaction of the continuum and molecular phenomena, but rather the physics

of the processes occurring in the grey area between the relevant scale domains.

One way to address the intermediate scales is to attempt to partially integrate the atomistic length scales. The resulting set of "coarse-grained" models has been successfully applied in the domain of MD simulations (see [46–49]). However, this approach is limited by the continuity of the integration process from the atomistic length scale.

A different point of view on the large-scale molecules can be provided by the models based on the equivalent mechanical representation. In these models, the concept of a micromechanical structure is introduced in order to represent a large molecule. Properties of the relevant mechanical structure are determined in order to provide correct behaviour of the structure with respect to the phenomena of interest. For example, it is possible to match diffusion and transport behaviour, elastic behaviour, etc.

The concept of mechanical model representation of macromolecules has been known for a long time in polymer physics. The relevant models have been used to analyse bulk behaviour of polymer solutions (see [50, 51]). However, the idea has also been applied as a method of modelling individual macromolecules in fluid flows ([52–55]).

In order to differentiate the approach presented in this thesis from other mesoscale models and underline the conceptual principles of the approach, we can draw on the analogy from the fields of software and systems engineering. In software engineering, models operating on other models are called "*meta-models*".

Originally, the term meta-model was used to define a model that defines the components of a conceptual model, process, or system [56]. The micromechanical models for fluid-molecule interaction are in effect, based on the definition of the components of the physical process and adjustment

of this definition required in order to capture the phenomena of interest. It seems therefore appropriate to use the term "meta-model" to refer to these models.

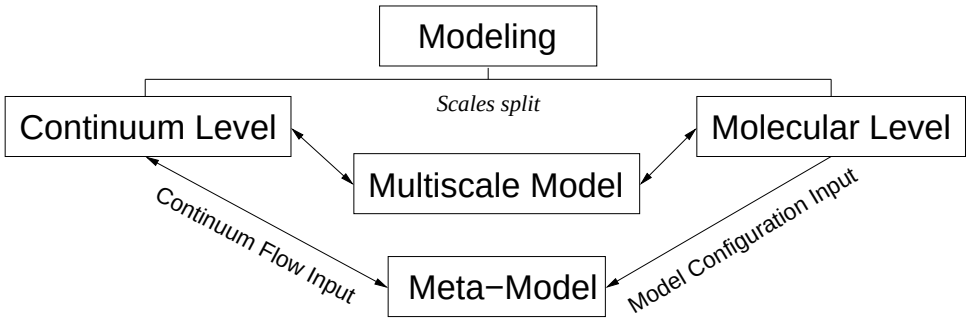

F 1.9: The place of meta-models amongst the existing approaches

The term *meta-modelling* refers to the exact modelling approach presented and discussed in this thesis. Although similar numerical techniques based on analogous ideas already exist in the technical literature, the modelling approach presented in this thesis is unique in many aspects. Probably the most relevant modelling method is the Brownian Dynamics simulation technique.

Similarly to the meta-modelling approach, Brownian Dynamics (BD) technique is based on the mechanical model representation of individual large molecules. BD technique also utilises the Langevin equation to describe fine scale behaviour of the concerning structure models.

However, numerical implementation of the BD method cancels out the inertia terms of the basic equations. Moreover, BD technique treats the solvent implicitly, while the meta-modelling approach models the solvent on the continuum level.

Such details result significant differences when considering complex and unsteady flow of the solvent.

Meta-modelling provides a viable solution to model processes occurring on the intermediate time scales. The technique was essentially developed to describe phenomenon occurring on typical time scales of $\sim 10^{-6} - 10^{-4}$ seconds, accounting for the effects of macroscopic scales. This method is therefore able to link two distinct modelling approaches.

The governing idea of the approach is the coarse-graining of atomistic scales in combination with the continuum-based description of phenomenon occurring on the macroscopic scales. Similarly to multiscale methods, meta-models are also based on selective refinement of scales. Instead of modelling the whole system on the same level of details, selected parts are described using fine scale resolution, while the remaining parts are treated with less detail.

One of the main differences of the meta-modelling technique compared to the combined micro-macro calculations lies in the scale-refinement method. In meta-modelling approach, description of fine scale physics is assigned to pre-defined molecules rather than to a selected spatial region of the computational domain.

In a meta-model, the investigated large molecules are represented as micromechanical structures derived from the atomic structure of the real molecule. Motion of the mechanical structures is governed by macroscopic forces arising from the motion of the bulk fluid phase and microscopic forces arising from stochastic Brownian motion of the solvent molecules. While macromolecules of interest are modelled individually and resolved on fine scales, the motion of the solvent is described on the continuum level.

Meta-modelling method successfully merges the Eulerian-based description of bulk continuum fluid field with the Lagrangian type tracking of

individual structures transported in the main flow. This approach is especially advantageous, when the size of the investigated molecules is large compared to the solvent molecules. The method is mainly used to describe transport processes in solutions with relatively low number densities of the solute material.

The technique draws information from molecular techniques in order to define model parameters, but the approach is essentially continuum-scale [45, 57]). The information exchange between the scales of the problem is one-way for the atomic part. Information exchange between the mechanical model and the continuum flow field can be either one-way or two-way, depending on the coupling strategy.

Considering meta-modelling technique, the required computational resources are similar to the requirements of conventional CFD simulations. The main advantage of this approach is the sufficiently detailed description of fine scale motion of selected individual macromolecules, without vast computational costs.

1.9 Micromechanics of DNA Molecules

The meta-modelling technique relies on mechanical models of real molecules. In order to construct accurate micromechanical representation of the considered macromolecules, their mechanical behaviour must be investigated.

Recent developments of laser-optical systems and microfluidic fabrication technologies triggered rapid evolution of single-molecule manipulation tools and visualisation devices. The developed single-molecule analysis systems facilitated fundamental studies of macromolecules.

The vast majority of the experimental investigations was focused on double-stranded DNA (dsDNA) molecules. However, mechanical measurements of single-stranded DNA molecules have been carried out as well.

1.9.1 Single-Stranded DNA

Our interest was primarily focused on the mechanical behaviour and the general properties of ssDNA molecules.

The natural form of nucleic acid molecules is the double-stranded configuration. The strand pairs form relatively rigid helical structures, which results in less flexible molecules [58–61]. Behaviour of single nucleic acid strands shows different character.

According to experiments carried out on detached DNA strands [58, 59], ssDNA molecules are more flexible than the helical dsDNA formations. Single molecule strands also possess shorter persistence lengths than the double-stranded configuration of the same strands. The persistence length characterises the flexibility of the molecule. By definition, it is the length over which the direction of the polymer molecule is uncorrelated.

Force-extension measurements indicated that single-stranded DNA can be extended almost to its contour length ($x/L_c <\sim 90\%$), without significant resistance. However when the molecule is extended over $\sim$ 90% of its contour length, considerable resistance against stretching was observed [58, 59].

The most suitable polymer model to describe this behaviour is the freely jointed chain (FJC) force-extension model [50]. In this model, the molecule is represented as a collection of spherical beads connected with non-extensible rods. End beads of the freely jointed chain can be distanced to $\sim$ 90% of the fully extended length of the chain, without significant resistance. When the chain end-to-end distance exceeds the limit value, the model resembles forces in order to contract the ends.

Considering the level of details and the phenomenon we are interested in, transported ssDNA molecules were described by a simplified model. Based on the FJC structure model, target molecules were represented as bead-rod chains. Concerning spherical particles were connected with freely rotating, non-extensible rods. The simple bead-rod model allows chain extension until the contour length, without producing contracting forces.

Investigating the flow conditions occurring in the microfluidic device, the transported ssDNA models will presumably not be subjected to strong streamwise velocity gradients. However, even if strong stretching of the molecules would occur, the simple bead-rod chain model will simply predict molecule conformations with higher end-to-end distance than the FJC model.

The slight difference in the predicted molecule lengths would not influence the investigated transport phenomenon and the resulting center-of-mass pathlines.

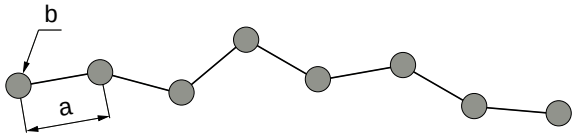

F 1.10: Bead-rod model of ssDNA with segment length *a* and bead radius *b*

1.9.2 Double-Stranded DNA

Due to their unique biological functions, double-stranded DNA molecules have been extensively investigated in the past decades. Smith *et al.* [58] carried out direct elasticity measurements of individual double-stranded DNAs.

During their experiments, single dsDNA molecules were tethered to a glass surface of a microfluidic device, with magnetic beads attached to the free end of the molecules. The molecules were exposed to external stretching forces resulting from drag and Lorentz forces acting on the attached beads.

The stretching force was carefully controlled by adjusting the flow parameters and the magnetic forces. The measured elastic response of the investigated molecules was compared against the freely jointed chain theory (FJC):

$$x = L_c \left(\coth \frac{Fa}{k_B T} - \frac{k_B T}{Fa} \right), \tag{1.8}$$

where F is the force magnitude, x is the mean force-dependent end-to-end distance, and L_c denotes the molecular contour length. Here, a denotes the length of a Kuhn segment and $k_B T$ is the thermal energy. Therefore, the force as the function of the extension x:

$$F = \frac{k_B T}{a} \mathcal{L}^{-1} \left(\frac{x}{L_c} \right), \tag{1.9}$$

with $\mathcal{L}^{-1}$ inverse Langevin function.

Smith *et al.* [58] observed strong deviations between their experimental results and the force curves predicted by the FJC model. Later, Bustamante *et al.* [60] summarised the experimental data of Smith *et al.* [58] in the following interpolation formula:

$$F = \frac{k_B T}{\lambda_p}\left(\frac{1}{4(1 - x/L_c)^2} - \frac{1}{4} + x/L_c\right), \tag{1.10}$$

where k_B is Boltzmann's constant, T is temperature, λ_p is the experimentally observed persistence length of the chain.

The formula was derived from experimental data of dsDNA with $L_c = 32.8 \pm 0.1\,\mu$m contour length and $\lambda_p = 53.4 \pm 2.3\,$nm persistence length. The referred persistence length is a characteristic property quantifying the flexibility of the polymer. Formula 1.10 is referred as the "inextensible wormlike chain" (WLC) force-elongation formula.

Perkins *et al.* [62] observed and reported the relaxation of individual dsDNA molecules after stretching by fluid flow. In their experiments, single latex microspheres were attached to one end of the molecules. The dsDNAs were optically trapped by the infrared laser beam focused on the latex beads. The molecules were stretched to their full extension by the fluid flow and allowed to relax after the flow was stopped. Video-enhanced fluorescence images of the stained molecules were recorded.

At this point, it is important to emphasise that the previously acknowledged single molecule studies [58, 62] were aimed to investigate the elastic behaviour of dsDNA molecules for relatively low extension forces [58] (typically $\sim 0.01 - 10\,$pN).

As the result of the applied moderate stretching forces, the molecules were not stretched over their contour length. The observed elastic response of the molecules in this force region is originated from the configurational

changes resulting from the imposed external forces.

Structure of dsDNA Molecules

A DNA molecule can be interpreted as a chain of uncorrelated linear segments [50]. This discretised representation of the real polymer is often referred as "bead-rod" structural model. The size of a chain subunit a, called Kuhn-step is twice the persistence length ($a = 2\lambda_p$). In the absence of external forces, DNA molecules resemble configurations close to a self-avoiding random-walk for a given end-to-end distance of the molecule [50, 63–65].

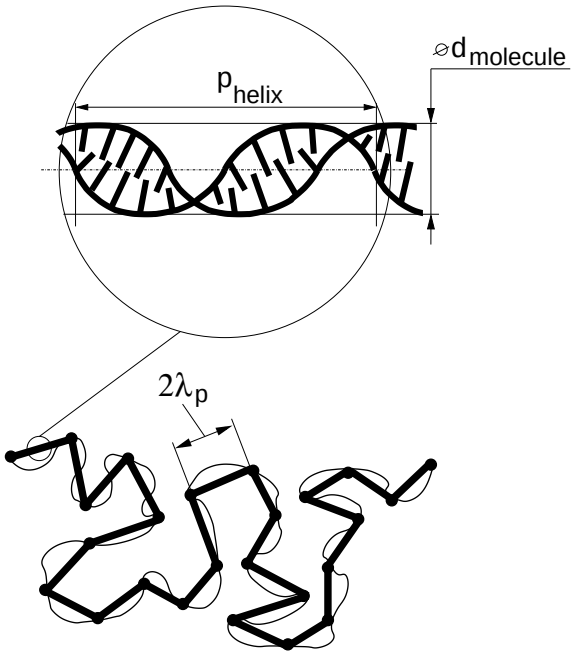

F 1.11: Random walk configuration and primary structure of dsDNA

When a moderate stretching force is applied on the ends of the molecule, the natural configurational space is bounded, therefore limiting the number of possible configurations. Such violation of the natural configurational

space results entropic changes, which gives a rise to restoring forces observed as the elastic response of the molecule on the macroscopic level [64].

Therefore, the elastic behaviour investigated below the over-stretching limit is referred as entropic elasticity of the molecule. As the molecular extension reaches and exceeds the over-stretching limit, intrinsic elasticity of the molecule becomes dominant [59].

While entropic elasticity of the molecule is originated from the orientational changes of chain subunits, intrinsic elasticity is resulted from over-stretching the Kuhn segments. Intrinsic elasticity is therefore a sub-Kuhn property of the molecule and directly related to changes in the primary molecular structure.

Over-stretching dsDNA

Smith *et al.* [59] reported results of DNA over-stretching experiments. During their investigations, single DNA molecules with polystyrene beads attached to both ends were stretched with force-measuring laser tweezers. The investigated dsDNAs were subjected to increasing stretching forces and the elastic behaviour of the molecules was registered.

A significant discontinuity in the molecule's response occurred at 65 pN. When reaching this force level, the molecule suddenly yielded, lengthened and overstretched to $\sim$ 1.7 times the molecule's contour length. The reported transition occurred in a narrow force range of $\sim$ 2 pN. The observed significant elongation was resulted from structural transition of the molecule.

A double-stranded DNA molecule consists of two long polymer chains

held together by hydrogen bonds between the complementary Watson-Crick base pairs (A-T) and (G-C). In its natural form, the strand pair forms a helical structure [63], as demonstrated on the insert of figure 1.11. The diameter of the base cylinder is $d_{molecule} \sim 2\,\text{nm}$ and the helix pitch is $p_{helix} \sim 3.4\,\text{nm}$ [63].

A chain subunit of a double-stranded DNA is therefore a helix generated by a cylinder with diameter of $\sim 2\,\text{nm}$ and the length of a Kuhn step ($\sim 106.8\,\text{nm}$). When the stretching force reaches a critical value, the helix suddenly uncoils, thus resulting a straight line. If the force is increased over this critical value, breakage of hydrogen bonds and partial separation of the strands occurs.

Early Numerical Studies of dsDNA Mechanics

Perkins *et al.* [66] observed the stretching of individual, fluorescently labelled dsDNA molecules in spatially homogeneous elongational flow generated by a cross-slit device. They have also predicted the rate of molecular extension using a simple dumbbell model. Their model consisted of two beads connected with a spring based on the Marko-Siggia WLC force law 1.10.

The beads acted as centers for the concerning drag forces and the connecting spring represented the action of the entropic restoring forces. Due to the simplicity of the applied model, the drag force was concentrated on the two ends of the molecule, instead of distributing it along the chain contour. Perkins [66] pointed out that the applied model provided accurate predictions of the molecule extension for the - so called - dumbbell dsDNA configuration, but overestimated the average measured chain dynamics.

The same simple model was extensively used in later studies to model

bulk properties of polymeric liquids, such as polymer stresses and stress-optic behaviour. Generally speaking, the simple dumbbell model accurately predicts the macroscopic behaviour of polymeric liquids, but due to its simplicity, it is unable to describe molecular conformations. Figure 1.12 shows the constitutive relation of the dumbbell mechanical model to the real molecule.

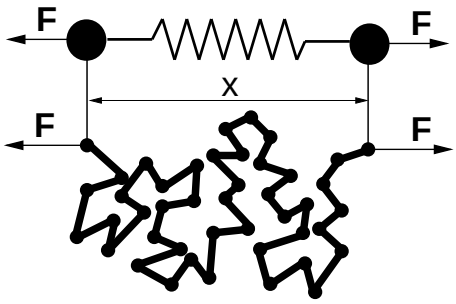

F 1.12: Relating the dumbbell elastic model to the real molecule

Dumbbell and Bead-Spring Models

Larson *et al.* [67] carried out Monte Carlo simulations of tethered DNA molecules in a uniform flow field. The applied DNA model was similar to Perkins's dumbbell model [66] with the same Marko-Siggia force law 1.10.

The behaviour of the model was governed by the molecule's entropic elasticity, the hydrodynamic drag and the Brownian forces arising from the random collisions of solvent molecules with the dsDNA. Since the molecule was tethered, there was only one free end of the chain and the appropriate model was a half-dumbbell.

To match the simulated degree of stretching with the experimentally observed molecular extension, the drag coefficient of the single bead of the half-dumbbell was 0.73 times the measured drag of the undeformed coil. This 27% drag reduction can be qualitatively understood by considering the equivalent degree of stretching produced by the concentrated drag at the chain end instead of distributing it along the entire chain contour.

In order to distribute the drag force along the chain contour, Larson [67] also considered a more complicated model by introducing extra beads. This coarse-grained representation of the real polymer is well-known from polymer science [50] and referred as the "bead-spring" model. The governing idea is to replace a segment of the chain - usually some 10-1000 Kuhn steps - with an entropic spring. Figure 1.13 illustrates the concept of coarse-graining a random-walk bead-rod polymer model to a bead-spring chain.

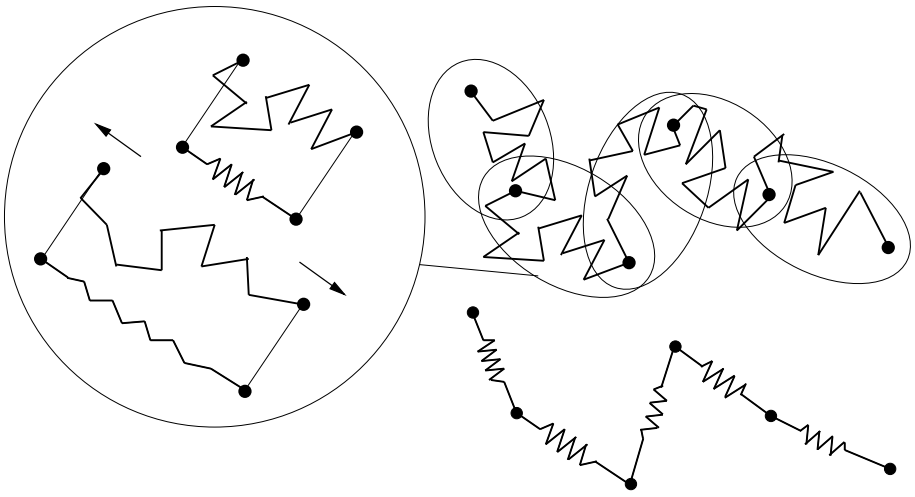

F 1.13: Coarse-graining the bead-rod polymer model into a bead-spring chain

In the first step of coarse-graining, reference points are defined along the contour of the bead-rod chain, usually coinciding with the joints of the discretised chain. These reference points will define the directions of

the springs, therefore sub-chain configurations will be screened out. In the following step, the Kuhn lengths between these reference points are systematically replaced with springs oriented by the reference points.

This model provides more detailed information on the molecular conformations than the dumbbell model, without the necessity to model each Kuhn step of the whole chain. The elastic spring force F_i for a concerning subchain is derived from 1.10 as follows:

$$F_i = \frac{k_B T}{\lambda_p^{eff}} \left(\frac{1}{4(1 - r_i/l)^2} - \frac{1}{4} + r_i/l \right), \tag{1.11}$$

where $l = L_c/(N-1)$ denotes the length of a submolecule, with N denoting the number of beads and r_i is the separation distance between bead "i" and "i+1". It is important to remark that since the spring law is based on relative extensions, this force-elongation formula for a sub-chain is - theoretically - consistent with the original Marko-Siggia 1.10 force law written for the dumbbell model.

The authors carried out Monte-Carlo simulations, using the bead-spring model and compared the calculated bead-mass distribution of the tethered dsDNA against measured distribution of molecular mass. During the bead-spring calculations, they accounted for bead-to-bead hydrodynamic interactions and considered the variation of drag force with the change of molecular extension. Average separations between the beads were used to construct the Oseen tensor and to calculate the effective hydrodynamic interactions [50, 68].

During the simulations, bead drag coefficients were treated as parameters and were obtained by requiring that the sum of the predicted bead drag forces $\sum_i \boldsymbol{F}_i^d$ equals to the total drag acting on the whole molecule. Drag coefficients of representative molecular configurations, such as coiled

and fully stretched states, were calculated from the Einstein relation [50, 65, 69] $\zeta_{coil} = k_B T/D$ and Batchelor's formula [50, 65] for a rigid rod $\zeta_{rod} = 2\pi L_c \eta / \ln(L_c/d_{molecule})$. In the formulas, D is the diffusion coefficient, η denotes the solvent viscosity and $d_{molecule}$ is the diameter of the molecule.

Although the simulated data showed good agreement with the measurements for various flow velocities, the authors reflected a very important detail regarding the bead-spring models. Larson *et al.* [67] pointed out that introduction of additional beads increases the flexibility of the molecule, since the freely rotating joints do not transmit bending moment. A common way to correct the introduced extra flexibility is to use a slightly increased persistence length, namely the effective persistence length λ_p^{eff}.

1.10 Coarse-Graining Molecule Models

The general idea of coarse-graining is to simplify the considered model in order to reduce the computational costs associated with the numerical solution. The simplified model must be able to capture representative properties with sufficient accuracy. The introduced simplifications consistently result in the loss of information, the effect of which must be considered during the coarse-graining method.

1.10.1 Derivation of Polymer Models

Focusing on mesoscopic description of polymers, a micro-structural mechanical representation of the real macromolecule has to be derived from the molecular level (full-atomistic) model. The method of coarse-graining is based on statistical mechanical considerations [70].

During this process, atomic vibrations are neglected, resulting in freely rotating bonds. Short-range pair-wise atomic interactions are also neglected, therefore elementary rigid segments along the chain - Kuhn-steps - can be defined. Kuhn steps represent an implicit measure of chain flexibility. Considering these assumptions, coarse-grained representation of a real polymer results in a chain of rigid rods connected with freely rotating bonds. This structural model is often referred as the bead-rod chain. In such a chain, beads act as drag centers and a single rod represents a Kuhn step.

As it was mentioned earlier, bead-rod models with consistently defined Kuhn steps provide accurate description of real polymer conformations. However, such models are not capable to describe the observed elastic behaviour of real chains [58]. The need to model force-elongation behaviour of real molecules initiated the development of bead-spring chains. The idea is based on the assumption of locally equilibrated motion of Kuhn

steps [70]. During this transformation, neighbouring Kuhn segments of a bead-rod model are systematically replaced with an entropic spring, resulting the loss of fine, sub-Kuhn details of the molecule configurations [64].

Coarse-graining of bead-rod models into bead-spring chains is a fundamental question of polymer dynamics. The aim of the transformation is to produce a simplified chain, but preserve characteristic properties with sufficient accuracy. This requirement arises contradicting constraints. On one hand, the coarse-grained model should be sufficiently detailed to approximate the configurations of the real polymer. Therefore, the number of springs should be increased to allow more detailed description of the molecular conformations. On the other hand, the model should provide realistic force-elongation behaviour of the chain.

1.10.2 Considerations

Force-elongation models of real molecules usually consider the polymer as a single spring with the same elastic response as the real molecule. Therefore, the number of springs in the bead-spring model should be minimised in order to reduce the artificial flexibility of the chain introduced by additional springs.

Larson *et al.* [71] carried out systematic Brownian dynamics studies of bead-spring chains and showed that force-elongation behaviour of the models change with increasing number of springs. Based on the results, they have [71] proposed the modification of the force-law by artificially stiffened springs, but did not provide guidelines for such a method.

Many studies suggested that a spring in bead-spring chains should represent a large segment of the polymer [64]. Similarly, Somasi [70] demonstrated that each spring should represent more than 10 Kuhn lengths (or 20 persistence lengths). In fact, considering purely the force-elongation behaviour of the polymer, the most accurate representation would be the dumbbell model.

However, other considerations require the opposite extrema, that the molecule should be described by as many beads as possible. Hydrodynamic behaviour of the polymer is mainly governed by viscous drag acting on the molecule. The total drag acting on the molecule is distributed amongst the beads, which act as drag centers.

In order to consistently distribute the drag along the contour of the molecule, a sufficient number of drag centers, beads are required. Another consideration supporting the large number of beads and springs is motivated purely by geometrical considerations. In case of modelling polymers in confined channels, the phenomena can only be described correctly, if the concerning length scale of the molecule is smaller than the confining channel dimension.

The challenge in consistent coarse-graining lies in the requirement of using large and small number of springs, within the same model. In order to determine the optimal level of coarse-graining, Underhill and Doyle [64] carried out detailed investigation of the force-extension behaviour of systematically coarse-grained bead-spring models.

During their investigations, both statistical mechanics and Brownian dynamics simulations have been used. They have concluded that since the springs are decoupled, force-elongation behaviour of the models depend on the number of rigid segments represented by each elastic spring. In other words, the elastic response of the bead-spring chain depends only

on the level of discretisation for each spring.

It is well-known from previous studies [71], that the introduction of additional springs into the chain modifies the elastic behaviour. The generally accepted explanation for this phenomena is based on the fact that freely rotating joints do not transmit bending moments, therefore introduction of extra springs adds extra flexibility to the chain [71]. Based on their theoretical investigations, Underhill and Doyle [64] pointed out that this explanation is not fully correct, since the mean fractional extension of the chain depends only on the discretisation level of each spring.

Focusing on the equivalence of force-extension behaviour of chains with varying level of coarse-graining, Underhill and Doyle [64] proposed the PET (polymer ensemble transformation) method. The PET method was developed to determine equivalent spring force laws, considering the coarse-graining level of each spring. Based on the PET transformation, the WLC formula (eq. 1.10) for a bead-spring chain is written as [72]:

$$F^s_{PET} = \frac{k_B T}{\lambda_p}\left\{\frac{\hat{x}}{(1-\hat{x}^2)^2} - \frac{7\hat{x}}{\chi(1-\hat{x}^2)} + \left(\frac{3}{32} - \frac{3}{4\chi} - \frac{6}{\chi^2}\right)\hat{x} + \right.$$
$$\left. + \left(\frac{(13/32) + (0.8172/\chi) - (14.79/\chi^2)}{1 - (4.225/\chi) + (4.78/\chi^2)}\right)\hat{x}(1-\hat{x}^2)\right\}, \quad (1.12)$$

with $k_B T$ thermal energy, λ_p persistence length and $\hat{x} = x/l$ fractional extension. Here, l denotes the fully extended length of a spring and χ is the number of persistence lengths represented by a spring.

1.10.3 Coarse-Graining Guidelines

Larson [73] carried out a theoretical study of bead-spring chains in order to determine general coarse-graining principles. His investigation was focused on the determination of a characteristic relaxation time by tracking

modes with different frequencies.

Larson concluded that the minimal number of springs required to represent the relaxation time of all modes depends on the Deborah number (De) [73]. The Deborah number is a dimensionless parameter used to characterise the stretching of polymers due to velocity differences of the flow field. By definition, the Deborah number is the ratio of the polymer relaxation time and the characteristic relaxation time of the fluid flow.

In practical applications, fluid flows are defined by the characteristic strain rate, which is the inverse of the fluid flow relaxation time. Therefore, the Deborah number is defined as: $\mathrm{De} = \tau_1 \varepsilon$, where τ_1 is the longest relaxation time of the polymer and ε is the strain rate.

A bead-spring chain with N beads contains $(N-1)$ modes. Considering flexible molecules, τ_i mode relaxation times ($i = 1, ..., N-1$) are proportional to the power of the mode number i: $\tau_i \sim i^{-p}$ [73], where p exponent ranges between 1.5 and 1.8 depending on the quality of the solvent. Considering the power law relation, the number of springs needed is: $(N-1) \gg (\tau_1 \varepsilon)^{1/p} \approx \mathrm{De}^{1/p}$ [73].

However, Larson [73] also considered an upper limit for the number of springs. Standard spring force laws have been derived considering that a spring represents many Kuhn steps. In practice, a spring is supposed to model at least ten Kuhn steps. Therefore, the number of springs cannot be increased above a critical point, where the number of Kuhn steps per springs drops below ten. The combination of these two criterias results the following formula:

$$10\mathrm{De}^{1/p} \leq N_s \leq N_K/10, \tag{1.13}$$

where N_s denotes the number of springs and N_K denotes the number of Kuhn steps of the chain.

Model Development

2

Model Development

Thorough analysis of the considered microchannel problem exposed significant details. Investigation of the device operation indicated that fundamental processes occurring in the investigated channel section are transport of DNA molecules and DNA base-pairing.

The parameter analysis clearly demonstrated the dominance of convective transport over the diffusive mechanism for the given parameter ranges. From the objective of the system, it is obvious that the number density of the ssDNA molecules present in the channel should be considered to be extremely low.

Analysis of the concerning scales revealed that processes relevant to bio-chemical applications cover a wide range of time and length scales. The transported substances are segments of single-stranded DNA molecules with lengths in the nanometer range, while the characteristic

length scale of microfluidic devices is in the micrometer range. This multiple scale nature of the microfluidic problem raises several difficulties.

Focusing on the design questions arising from the practical side, we are more interested in the quasi-macroscopic transport properties than detailed description of fine scale reactions. Quasi-macroscopic description of the problem provides information regarding ssDNA pathlines and residence times. This requirement defines the lower limit for the time scales of interest at the order of 10^{-6} seconds.

Considering the modelling approaches, characteristic time scales make atomistic models impractical. On the other hand, the level of details required concerning the transport process make pure continuum models inaccurate.

Meta-models [45, 57] however, provide a reasonable solution to describe problems on these scales. This modelling technique is quite efficient when molecules of interest are several orders of magnitude larger than the solvent ones and the number density of the transported solute is extremely low.

Analysing characteristic scales of the problem and considering the questions arising from the engineering side, meta-modelling has proven to be the most suitable approach to support and guide function-oriented design of microchannels.

2.1 Basic Equations of Meta-Models

The meta-modelling technique applied to describe the investigated dilute ssDNA solution is based on micro-mechanical models of real molecules. The key idea of meta-modelling is the dual numerical description of the solvent and solute molecules. The technique successfully merges the fine scale description of individual large molecules, with the cumulative ensemble averaged description of solvent molecules on the continuum-level scales.

In the meta-modelling approach, individual large molecules are represented as micro-mechanical structure models of real molecules. Parameters of the structure models are adjusted to provide correct static and dynamic behaviour. Macromolecules are typically modeled as series of beads connected with freely rotating, non-extensible rods or elastic springs. Type of the connecting element depends on elastic properties of the concerning real macromolecule under the given conditions.

In such mechanical structure models, beads act as centers for forces. Th purpose of the connecting elements is to preserve the structure of the model and mimic the elastic behaviour of real molecules. During numerical calculations, beads experience macroscopic forces and microscopic effects arising from the solvent and from the changes of the molecular configuration. Considering the micro-mechanical representation of a macromolecule, fine scale behaviour of bead n is described by the Langevin equation [45, 50]:

$$m_n \frac{d^2 \mathbf{r}_n}{dt^2} = \mathbf{f}_n \,, \tag{2.1}$$

where $\mathbf{f}_n$ represents the total force acting on particle n. Investigating the transport of macromolecule structures in dilute solution, the sum of forces

acting on a single bead is as follows:

$$\boldsymbol{f}_n = m_n\gamma_n\left(\boldsymbol{u}(\boldsymbol{r}_n) - \boldsymbol{v}_n\right) + \boldsymbol{\phi}_n + \boldsymbol{\varphi}_n(t) \tag{2.2}$$

with $m_n\gamma_n = 6\pi\eta b_n$ friction coefficient arising from the Stokes drag of a sphere with radius b_n, in a fluid with η dynamic viscosity. $\boldsymbol{u}(\boldsymbol{r}_n)$ is the fluid velocity at position $\boldsymbol{r}_n$, $\boldsymbol{v}_n$ represents the particle velocity. $\boldsymbol{\phi}_n$ represents the sum of all non-hydrodynamic forces (typically elastic spring) and will be discussed later. $\boldsymbol{\varphi}_n(t)$ is the random Brownian force, modelling the effect of solvent molecules stochastically colliding to the beads and exchanging impulse. The random force possess Gaussian distribution characterised as ([45, 50]):

$$< \boldsymbol{\varphi}_n(t) >= 0 \tag{2.3}$$

$$< \boldsymbol{\varphi}_n(t)\boldsymbol{\varphi}_n(t') >= 2\, m_n\gamma_n\, k_B T\, \delta(t - t') \tag{2.4}$$

Considering the total force acting on each particle, additional volumetric force experienced by the carrier liquid is calculated as:

$$\mathcal{F}(\boldsymbol{r}) = -\sum_n \boldsymbol{f}_n\, \delta_\epsilon(\boldsymbol{r} - \boldsymbol{r}_n) \tag{2.5}$$

with δ_ϵ smoothed Dirac function of ϵ length scale. This function incorporates division with unit volume, therefore transforms the concerning point-like force $\boldsymbol{f}_n$ into a volumetric force field.

The governing equation of the unsteady flow of incompressible carrier liquid is described by scalar components of the Navier-Stokes equations. The momentum equations alone do not form a closed system, therefore the continuity equation derived from the principle of mass conservation is used to eliminate the closure problem. The system of equations governing

fluid motion is therefore written as ([45]):

$$\frac{\partial \boldsymbol{u}}{\partial t} + (\boldsymbol{u} \cdot \nabla)\boldsymbol{u} = -\frac{1}{\rho}\nabla p + \nu \Delta \boldsymbol{u} + \frac{1}{\rho}\boldsymbol{\mathcal{F}} \tag{2.6}$$

$$\nabla \cdot \boldsymbol{u} = 0 \tag{2.7}$$

where $\boldsymbol{\mathcal{F}}$ on the right-hand side of the momentum equation represents the additional force distributed over elementary volume δV. The equations describe the motion of incompressible fluid with density ρ, pressure p, kinematic viscosity ν and velocity $\boldsymbol{u}$ according to volumetric force $\boldsymbol{\mathcal{F}}$ induced by the transport of long chain molecules.

2.2 Solution of the Fluid Flow Equations

During the simulations, the flow field was calculated using the in-house finite volume artificial compressibility solver, with inviscid fluxes approximated using the characteristics-based method (e.g. [74–79]) combined with the third order variables reconstruction ([74, 75]).

The integration in pseudo-time for the artificial compressibility formulation was performed using the fourth-order Runge-Kutta method (e.g. [74, 75]). The used software is the evolution of the incompressible version of the code CNS3D [80, 81] to incompressible flows [74, 78, 79].

In the first step of the numerical solution, the basic equations have been scaled with suitable parameters. Nondimensionalisation of the governing equations is a general practice in numerical calculation of fluid flows. Working with normalised equations is not only practical, but also increases numerical accuracy of the calculations. Scaling of the relevant quantities simplifies the detection of numerical overshoots and divergence.

2.2.1 Nondimensionalisation

Let us consider the following reference variables: L, U and ρ, denoting length scale, characteristic velocity and fluid density. According to common routine, the following nondimensional variables are derived:

$$\boldsymbol{r}^* = \frac{\boldsymbol{r}}{L}, \quad \nabla^* = L \cdot \nabla, \quad \Delta^* = L^2 \cdot \Delta, \quad \boldsymbol{u}^* = \frac{\boldsymbol{u}}{U}, \quad t^* = \frac{t\,U}{L},$$

$$p^* = \frac{p}{\rho\, U^2}, \quad \boldsymbol{v}_n^* = \frac{\boldsymbol{v}_n}{U}, \quad b^* = \frac{b}{L}, \quad \rho_n^* = \frac{m_n}{\rho\, L^3}, \quad \mathcal{F}^* = \frac{\mathcal{F} L}{\rho U^2}, \quad \mathrm{Re} = \frac{UL}{\nu}.$$

With the introduced scaled variables, nondimensional form of the constant density flow equations 2.6 and 2.7 is written as:

$$\frac{\partial \boldsymbol{u}^*}{\partial t^*} + (\boldsymbol{u}^* \cdot \nabla^*)\boldsymbol{u}^* = -\nabla^* p^* + \frac{1}{\mathrm{Re}}\Delta^* \boldsymbol{u}^* + \boldsymbol{\mathcal{F}}^* \tag{2.8}$$

$$\nabla^* \cdot \boldsymbol{u}^* = 0 \tag{2.9}$$

Consequently, the nondimensional form of the Langevin equation 2.1 is written as follows:

$$\frac{d^2 \boldsymbol{r}_n^*}{dt^{*2}} = \boldsymbol{f}_n^*, \tag{2.10}$$

with nondimensional total force acting on each bead:

$$\boldsymbol{f}_n^* = \gamma_n^* (\boldsymbol{u}^*(\boldsymbol{r}_n^*) - \boldsymbol{v}_n^*) + \boldsymbol{\phi}_n^* + \boldsymbol{\varphi}_n^*(t^*). \tag{2.11}$$

Here, the concerning variables are defined as:

$$\boldsymbol{f}_n^* = \frac{\boldsymbol{f}_n L}{m_n U^2}, \quad \boldsymbol{\phi}_n^* = \frac{\boldsymbol{\phi}_n L}{m_n U^2}, \quad \boldsymbol{\varphi}_n^* = \frac{\boldsymbol{\varphi}_n L}{m_n U^2}, \quad \gamma_n^* = \frac{\gamma_n L}{U} = \frac{6\pi b_n^*}{\rho_n^* \mathrm{Re}}.$$

At this point, we omit the concerning "$*$" upper index in order to simplify the notation system. The following model equations of this chapter (2) are written for nondimensional variables. Consequently, the considered variables are scaled ones, however their notation follows the discussed simplified schema.

2.2.2 Artificial Compressibility Formulation

In the investigated model, the fluid is considered to be ideal, viscous Newtonian and incompressible. The main challenge during numerical simulation of incompressible flows arises from the decoupling of the pressure field from the velocity and density fields. In order to couple the pressure and momentum, pressure projection methods [82], pressure correction algorithms [83] or artificial compressibility method [84] could be considered, see [2] for a review.

The applied artificial compressibility approach [84] circumvents the problem of pressure decoupling by adding a pseudo-time derivative to the continuity equation 2.7. Therefore, the resulting modified system of equations 2.12 and 2.13 can be iterated in pseudo-time, until divergence-free flow field is achieved. The method is compatible with both steady and unsteady flows. The artificial compressibility formulation of the basic equations is:

$$\frac{1}{\beta}\frac{\partial p}{\partial \tau} + \nabla \cdot \boldsymbol{u} = 0 \tag{2.12}$$

$$\frac{\partial \boldsymbol{u}}{\partial \tau} + \frac{\partial \boldsymbol{u}}{\partial t} + (\boldsymbol{u} \cdot \nabla)\boldsymbol{u} = -\nabla p + \frac{1}{\mathrm{Re}}\Delta \boldsymbol{u} + \mathcal{F} \tag{2.13}$$

As the system 2.12 and 2.13 converges to a steady state in pseudo-time, the concerning pseudo-time derivates tend to zero and the solution can proceed in real time.

The artificial compressibility formulation results in hyperbolic-parabolic equations for constant density, viscous incompressible flows. Therefore, the governing equations are solved using methods and schemes developed for compressible flows. The system of fluid flow equations can be written in a conservative form with Cartesian (distinguished by "C" upper index)

coordinates (x, y, z) [2]:

$$\frac{\partial \mathbf{U}}{\partial \tau} = -\frac{\partial \mathbf{U}_r}{\partial t} + \frac{\partial \mathbf{E}_{\mathrm{V}}^{\mathrm{C}}}{\partial x} + \frac{\partial \mathbf{F}_{\mathrm{V}}^{\mathrm{C}}}{\partial y} + \frac{\partial \mathbf{G}_{\mathrm{V}}^{\mathrm{C}}}{\partial z} - \frac{\partial \mathbf{E}_{\mathrm{I}}^{\mathrm{C}}}{\partial x} - \frac{\partial \mathbf{F}_{\mathrm{I}}^{\mathrm{C}}}{\partial y} - \frac{\partial \mathbf{G}_{\mathrm{I}}^{\mathrm{C}}}{\partial z} + \mathbf{F}^{\mathrm{C}} \quad (2.14)$$

with the following compact notation [2]:

$$\begin{aligned} \mathbf{U} &= \left(p/\beta, u, v, w\right)^T \\ \mathbf{U}_r &= \left(0, u, v, w\right)^T. \end{aligned} \quad (2.15)$$

Advective fluxes in the Cartesian system are written as:

$$\begin{aligned} \mathbf{E}_{\mathrm{I}}^{\mathrm{C}} &= \left(u, u^2 + p, uv, uw\right)^T \\ \mathbf{F}_{\mathrm{I}}^{\mathrm{C}} &= \left(v, vu, v^2 + p, vw\right)^T \\ \mathbf{G}_{\mathrm{I}}^{\mathrm{C}} &= \left(w, wu, wv, w^2 + p\right)^T, \end{aligned} \quad (2.16)$$

the concerning viscous fluxes are:

$$\begin{aligned} \mathbf{E}_{\mathrm{V}}^{\mathrm{C}} &= \left(0, \tau_{xx}, \tau_{xy}, \tau_{xz}\right)^T \\ \mathbf{F}_{\mathrm{V}}^{\mathrm{C}} &= \left(0, \tau_{yx}, \tau_{yy}, \tau_{yz}\right)^T \\ \mathbf{G}_{\mathrm{V}}^{\mathrm{C}} &= \left(0, \tau_{zx}, \tau_{zy}, \tau_{zz}\right)^T \end{aligned} \quad (2.17)$$

and the extra volume force arising from the transported solute is:

$$\mathbf{F}^{\mathrm{C}} = \left(0, \mathcal{F}_x, \mathcal{F}_y, \mathcal{F}_z\right)^T. \quad (2.18)$$

2.2.3 Geometrical Transformation

In practical channel flow problems, fluid transport occurs in ducts with arbitrary geometry. In order to simplify the flux calculations, fluid flow equations are usually transformed into a computational coordinate system (see figure 2.1). In terms of flux differentiation, the most suitable computational system is a generalised coordinate system with uniform metrics.

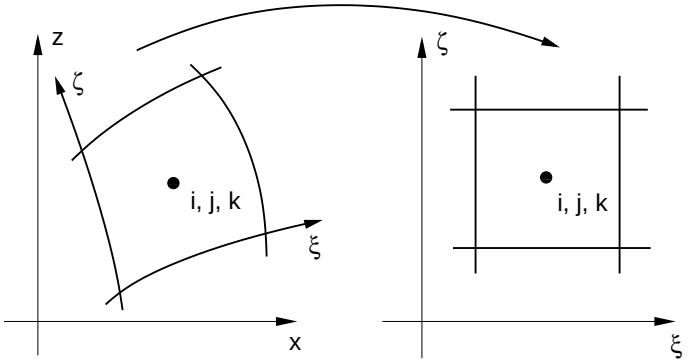

F 2.1: Cartesian (left) and generalised (right) coordinate systems

Let us consider a generalised uniform curvilinear system $(\xi, \eta, \zeta, \vartheta)$, which can be easily adapted to the geometry. In order to simplify the flux calculations, incompressible Navier-Stokes equations are transformed into this generalised coordinate system. Transformation coordinates are defined as:

$$\begin{aligned} \xi &= \xi(x, y, z) \\ \eta &= \eta(x, y, z) \\ \zeta &= \zeta(x, y, z) \end{aligned} \tag{2.19}$$

Current research work focused only on non-moving computational domains, therefore the transformed time was defined as $\vartheta = t$. According to this assumption and referring to the chain rule of differentation, first

order partial derivatives are written as:

$$\frac{\partial}{\partial x} = \left(\frac{\partial}{\partial \xi}\right)\frac{\partial \xi}{\partial x} + \left(\frac{\partial}{\partial \eta}\right)\frac{\partial \eta}{\partial x} + \left(\frac{\partial}{\partial \zeta}\right)\frac{\partial \zeta}{\partial x} \tag{2.20}$$

$$\frac{\partial}{\partial y} = \left(\frac{\partial}{\partial \xi}\right)\frac{\partial \xi}{\partial y} + \left(\frac{\partial}{\partial \eta}\right)\frac{\partial \eta}{\partial y} + \left(\frac{\partial}{\partial \zeta}\right)\frac{\partial \zeta}{\partial y} \tag{2.21}$$

$$\frac{\partial}{\partial z} = \left(\frac{\partial}{\partial \xi}\right)\frac{\partial \xi}{\partial z} + \left(\frac{\partial}{\partial \eta}\right)\frac{\partial \eta}{\partial z} + \left(\frac{\partial}{\partial \zeta}\right)\frac{\partial \zeta}{\partial z} \tag{2.22}$$

$$\frac{\partial}{\partial t} = \left(\frac{\partial}{\partial \xi}\right)\frac{\partial \xi}{\partial t} + \left(\frac{\partial}{\partial \eta}\right)\frac{\partial \eta}{\partial t} + \left(\frac{\partial}{\partial \zeta}\right)\frac{\partial \zeta}{\partial t} + \frac{\partial}{\partial \vartheta}. \tag{2.23}$$

Based on these first order derivates, higher order derivates can be derived systematically [2]. The connection between the two coordinate systems is represented by the Jacobi matrix characterising the transformations. It is formulated utilising first order cross-system derivates. Determinant of the transformation matrix is used to derive cross-derivates [2]:

$$J = \left|\frac{\partial(x, y, z)}{\partial(\xi, \eta, \zeta)}\right| \tag{2.24}$$

The system of basic equations written in curvilinear coordinates is as follows [2]:

$$\frac{\partial J\mathbf{U}}{\partial \tau} = -\frac{\partial J\mathbf{U}_r}{\partial t} + \frac{\partial \mathbf{E}_\mathrm{V}}{\partial \xi} + \frac{\partial \mathbf{F}_\mathrm{V}}{\partial \eta} + \frac{\partial \mathbf{G}_\mathrm{V}}{\partial \zeta} - \frac{\partial \mathbf{E}_\mathrm{I}}{\partial \xi} - \frac{\partial \mathbf{F}_\mathrm{I}}{\partial \eta} - \frac{\partial \mathbf{G}_\mathrm{I}}{\partial \zeta} + \mathbf{F}, \tag{2.25}$$

where the inviscid (I) fluxes are:

$$\mathbf{E}_\mathrm{I} = J\left(\mathbf{E}_\mathrm{I}^\mathrm{C}\frac{\partial \xi}{\partial x} + \mathbf{F}_\mathrm{I}^\mathrm{C}\frac{\partial \xi}{\partial y} + \mathbf{G}_\mathrm{I}^\mathrm{C}\frac{\partial \xi}{\partial z}\right) \tag{2.26}$$

$$\mathbf{F}_\mathrm{I} = J\left(\mathbf{E}_\mathrm{I}^\mathrm{C}\frac{\partial \eta}{\partial x} + \mathbf{F}_\mathrm{I}^\mathrm{C}\frac{\partial \eta}{\partial y} + \mathbf{G}_\mathrm{I}^\mathrm{C}\frac{\partial \eta}{\partial z}\right) \tag{2.27}$$

$$\mathbf{G}_{\mathrm{I}} = J\left(\mathbf{E}_{\mathrm{I}}^{\mathrm{C}}\frac{\partial\zeta}{\partial x} + \mathbf{F}_{\mathrm{I}}^{\mathrm{C}}\frac{\partial\zeta}{\partial y} + \mathbf{G}_{\mathrm{I}}^{\mathrm{C}}\frac{\partial\zeta}{\partial z}\right) \tag{2.28}$$

and viscous (V) fluxes in general curvilinear coordinates:

$$\mathbf{E}_{\mathrm{V}} = J\left(\mathbf{E}_{\mathrm{V}}^{\mathrm{C}}\frac{\partial\xi}{\partial x} + \mathbf{F}_{\mathrm{V}}^{\mathrm{C}}\frac{\partial\xi}{\partial y} + \mathbf{G}_{\mathrm{V}}^{\mathrm{C}}\frac{\partial\xi}{\partial z}\right) \tag{2.29}$$

$$\mathbf{F}_{\mathrm{V}} = J\left(\mathbf{E}_{\mathrm{V}}^{\mathrm{C}}\frac{\partial\eta}{\partial x} + \mathbf{F}_{\mathrm{V}}^{\mathrm{C}}\frac{\partial\eta}{\partial y} + \mathbf{G}_{\mathrm{V}}^{\mathrm{C}}\frac{\partial\eta}{\partial z}\right) \tag{2.30}$$

$$\mathbf{G}_{\mathrm{V}} = J\left(\mathbf{E}_{\mathrm{V}}^{\mathrm{C}}\frac{\partial\zeta}{\partial x} + \mathbf{F}_{\mathrm{V}}^{\mathrm{C}}\frac{\partial\zeta}{\partial y} + \mathbf{G}_{\mathrm{V}}^{\mathrm{C}}\frac{\partial\zeta}{\partial z}\right). \tag{2.31}$$

The additional volume force in the general curvilinear system is:

$$\mathbf{F} = J\left(0, \mathcal{F}_x, \mathcal{F}_y, \mathcal{F}_z\right)^T. \tag{2.32}$$

2.2.4 Hyperbolic Solver

Numerical solution of the basic equations 2.25 is carried out utilising a finite-volume hyperbolic solver based on the method of characteristics. Let us consider a suitable arrangement of the basic equations, accommodating the hyperbolic terms on the left:

$$\frac{\partial J\mathbf{U}}{\partial\tau} + \frac{\partial\mathbf{E}_{\mathrm{I}}}{\partial\xi} + \frac{\partial\mathbf{F}_{\mathrm{I}}}{\partial\eta} + \frac{\partial\mathbf{G}_{\mathrm{I}}}{\partial\zeta} = -\frac{\partial J\mathbf{U}_r}{\partial t} + \frac{\partial\mathbf{E}_{\mathrm{V}}}{\partial\xi} + \frac{\partial\mathbf{F}_{\mathrm{V}}}{\partial\eta} + \frac{\partial\mathbf{G}_{\mathrm{V}}}{\partial\zeta} + \mathbf{F}. \tag{2.33}$$

Considering the applied solution method, real-time derivatives, viscous terms and volume forces are treated explicitly. Practically, the hyperbolic solver concerns the following equation:

$$\frac{\partial J\mathbf{U}}{\partial\tau} + \frac{\partial\mathbf{E}_{\mathrm{I}}}{\partial\xi} + \frac{\partial\mathbf{F}_{\mathrm{I}}}{\partial\eta} + \frac{\partial\mathbf{G}_{\mathrm{I}}}{\partial\zeta} = \mathbf{0}. \tag{2.34}$$

During the numerical solution of the hyperbolic equation system 2.34, 1-D directional splits of the original 3-D problem are considered:

$$\frac{\partial J\mathbf{U}}{\partial \tau} + \frac{\partial \mathbf{E}_{\mathrm{I}}}{\partial \xi} = \mathbf{0} \tag{2.35}$$

$$\frac{\partial J\mathbf{U}}{\partial \tau} + \frac{\partial \mathbf{F}_{\mathrm{I}}}{\partial \eta} = \mathbf{0} \tag{2.36}$$

$$\frac{\partial J\mathbf{U}}{\partial \tau} + \frac{\partial \mathbf{G}_{\mathrm{I}}}{\partial \zeta} = \mathbf{0}. \tag{2.37}$$

The solution of the original 3-D problem 2.34 is achieved as the superposition of the concerning 1-D splits. The 1-D split Riemann problems were solved utilising the Characteristics-Based (CB) method developed for incompressible flows (e.g. [74, 78, 79]).

2.2.5 Characteristic-Based Scheme

Basic idea of the CB method lies is the unique definition of inviscid fluxes. In this approach, advective fluxes are constructed by specifying the primitive variables as functions of their values on the relevant characteristics [2]. In order to demonstrate the CB scheme, let us consider the following scalar hyperbolic problem written in Cartesian system, along coordinate x:

$$\frac{\partial U}{\partial t} + \frac{\partial E}{\partial x} = 0. \tag{2.38}$$

Update of the studied conservation law is given by ([2])

$$U(t + \Delta t) = U(t) - \int_t^{t+\Delta t} \frac{\partial E(U)}{\partial x} dt. \tag{2.39}$$

Here, the spatial derivative of the flux E is known at time level t, the lower bound.

Accurate determination of the integral requires a method to allow the development of the formula in time to perform a stable update. In order to determine the solution at $(x, t + \Delta t)$, a linear Taylor expansion is performed as ([2]):

$$U(x, t + \Delta t) = U(x - \Delta\xi, t) + \Delta\xi \frac{\partial U}{\partial x} + \Delta t \frac{\partial U}{\partial t}, \tag{2.40}$$

with neglecting the higher-order terms. Let us denote $U(x - \Delta\xi, t) = U_l$

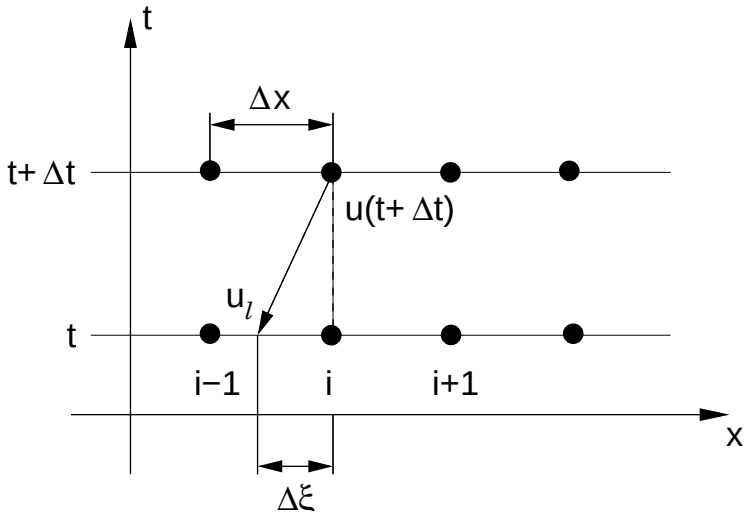

F 2.2: Calculation of $U(x, t + \Delta t) = \tilde{U}$, based on the characteristic variable U_l (schematic adapted from [2])

and $U(x, t + \Delta t) = \tilde{U}$, and introduce wave speed as $\dot{\xi} = \partial\xi/\partial t$. Utilising the definition of the wave speed $\dot{\xi}$, the relative offset of the characteristic variable is $\Delta\xi = \dot{\xi}\Delta t$. With this formula of $\Delta\xi$, the update of U (in 2.40) is written as [2]:

$$\tilde{U} = U_l + \left(\frac{\partial U}{\partial t} + \frac{\partial U}{\partial x} \dot{\xi} \right) \Delta t. \tag{2.41}$$

Here, all terms are unknown. From the hyperbolic equation 2.38, the time derivative of U is written as

$$\frac{\partial U}{\partial t} = -\frac{\partial E(U)}{\partial x}. \tag{2.42}$$

Applying the chain rule of differentiation, the spatial derivative of advective flux E is

$$\frac{\partial E(U)}{\partial x} = \frac{\partial E(U)}{\partial U}\frac{\partial U}{\partial x}. \tag{2.43}$$

Therefore, substituting $\partial U/\partial t$ into equation 2.41 results:

$$\tilde{U} = U_l + \frac{\partial U}{\partial x}\left[\dot{\xi} - \frac{\partial E(U)}{\partial U}\right]\Delta t. \tag{2.44}$$

By definition, the wave speed is an eigenvalue, $\dot{\xi} = \partial E(U)/\partial U$ [2]. Therefore, the multiplier of the spatial derivate $\partial U/\partial x$ cancels out, thus resulting

$$\tilde{U} = U_l. \tag{2.45}$$

Practically, the update $\tilde{U}$ can be obtained using the characteristic variable U_l at point $(x - \dot{\xi}\Delta t, t)$. This value belongs to the characteristic line with slope $1/\dot{\xi}$. The concerning variable U_l can be calculated using higher-order interpolation. Having $\tilde{U} = U_l$ in hand, the advective flux $E(\tilde{U})$ can be determined.

Although the CB solution strategy has been demonstrated for a simple 1-D case, the method can be extended to multi-dimensional flow problems as well [2]. In such cases, more than one characteristic line exists. Therefore, the flux $E(\tilde{U})$ would be the function of all characteristic variables lying on the lines with slopes $1/\dot{\xi}_l$, $(l = 0 - 2)$.

2.2.6 CB Reconstruction

Let us consider a three-dimensional hyperbolic flow problem for incompressible fluids. This problem concerns the following vector of characteristic variables: $\tilde{\mathbf{U}} = (\tilde{p}, \tilde{u}, \tilde{v}, \tilde{w})^T$. Calculation of the concerning variables is being performed using characteristic-based (CB) reconstruction.

Although the flow problem is three-dimensional, 1-D counterpart (along ξ) of the basic equation 2.34 has been considered [77] to demonstrate the reconstruction method:

$$\frac{\partial \mathbf{U}}{\partial \tau} + \frac{\partial \xi}{\partial x}\frac{\partial \mathbf{E}_{\mathrm{I}}^{\mathrm{C}}}{\partial \xi} + \frac{\partial \xi}{\partial y}\frac{\partial \mathbf{F}_{\mathrm{I}}^{\mathrm{C}}}{\partial \xi} + \frac{\partial \xi}{\partial z}\frac{\partial \mathbf{G}_{\mathrm{I}}^{\mathrm{C}}}{\partial \xi} = \mathbf{0}. \tag{2.46}$$

Let us introduce the following notations: $\Lambda = \sqrt{\left(\frac{\partial \xi}{\partial x}\right)^2 + \left(\frac{\partial \xi}{\partial y}\right)^2 + \left(\frac{\partial \xi}{\partial z}\right)^2}$ and $\tilde{k} = \frac{1}{\Lambda}\frac{\partial \xi}{\partial k}$, with $k = x, y, z$. Dividing equation 2.46 with Λ and utilising the simplified notations results the following conservative formulation ([77]):

$$\begin{cases} \frac{1}{\beta\Lambda}\frac{\partial p}{\partial \tau} + \tilde{x}\frac{\partial u}{\partial \xi} + \tilde{y}\frac{\partial v}{\partial \xi} + \tilde{z}\frac{\partial w}{\partial \xi} = 0 \\ \frac{1}{\Lambda}\frac{\partial u}{\partial \tau} + (u\tilde{x} + v\tilde{y} + w\tilde{z})\frac{\partial u}{\partial \xi} + \left(\tilde{x}\frac{\partial u}{\partial \xi} + \tilde{y}\frac{\partial v}{\partial \xi} + \tilde{z}\frac{\partial w}{\partial \xi}\right)u + \frac{\partial p}{\partial \xi}\tilde{x} = 0 \\ \frac{1}{\Lambda}\frac{\partial v}{\partial \tau} + (u\tilde{x} + v\tilde{y} + w\tilde{z})\frac{\partial v}{\partial \xi} + \left(\tilde{x}\frac{\partial u}{\partial \xi} + \tilde{y}\frac{\partial v}{\partial \xi} + \tilde{z}\frac{\partial w}{\partial \xi}\right)v + \frac{\partial p}{\partial \xi}\tilde{y} = 0 \\ \frac{1}{\Lambda}\frac{\partial w}{\partial \tau} + (u\tilde{x} + v\tilde{y} + w\tilde{z})\frac{\partial w}{\partial \xi} + \left(\tilde{x}\frac{\partial u}{\partial \xi} + \tilde{y}\frac{\partial v}{\partial \xi} + \tilde{z}\frac{\partial w}{\partial \xi}\right)w + \frac{\partial p}{\partial \xi}\tilde{z} = 0 \end{cases} \tag{2.47}$$

The above system of equations can be written in matrix form as:

$$\frac{1}{\Lambda}\frac{\partial \mathbf{U}}{\partial \tau} + \mathbf{A}\frac{\partial \mathbf{U}}{\partial \xi} = \mathbf{0}, \tag{2.48}$$

where matrix $\mathbf{A}$ is ([77]):

$$\mathbf{A} = \begin{pmatrix} 0 & \tilde{x} & \tilde{y} & \tilde{z} \\ \tilde{x} & \lambda_0 + \tilde{x}u & \tilde{y}u & \tilde{z}u \\ \tilde{y} & \tilde{x}v & \lambda_0 + \tilde{y}v & \tilde{z}v \\ \tilde{z} & \tilde{x}w & \tilde{y}w & \lambda_0 + \tilde{z}w \end{pmatrix}. \tag{2.49}$$

Here, $\lambda_0 = \tilde{x}u + \tilde{y}v + \tilde{z}w$ denotes the velocity normal to the given cell face. Eigenvalues of matrix $\mathbf{A}$ are given by λ_0, λ_1 and λ_2, where

$$\lambda_1 = \lambda_0 + s, \quad \lambda_2 = \lambda_0 - s \tag{2.50}$$

with s artificial speed of sound defined as:

$$s = \sqrt{\lambda_0^2 + \beta}. \tag{2.51}$$

Following the derivation of the CB scheme [74], the reconstructed variables at the cell face:

$$\tilde{\mathbf{U}} = \begin{pmatrix} \tilde{p} \\ \tilde{u} \\ \tilde{v} \\ \tilde{w} \end{pmatrix} = \begin{pmatrix} \frac{1}{\lambda_1 - \lambda_2}(p_2\lambda_1 - p_1\lambda_2 + \lambda_1\lambda_2(R_1 - R_2)) \\ u_0 + \frac{\tilde{x}}{\lambda_1 - \lambda_2}(p_1 - p_2 - \lambda_1 R_1 + \lambda_2 R_2) \\ v_0 + \frac{\tilde{y}}{\lambda_1 - \lambda_2}(p_1 - p_2 - \lambda_1 R_1 + \lambda_2 R_2) \\ w_0 + \frac{\tilde{z}}{\lambda_1 - \lambda_2}(p_1 - p_2 - \lambda_1 R_1 + \lambda_2 R_2) \end{pmatrix}, \tag{2.52}$$

with R_1 and R_2 auxiliary functions:

$$\begin{aligned} R_1 &= \tilde{x}(u_0 - u_1) + \tilde{y}(v_0 - v_1) + \tilde{z}(w_0 - w_1) \\ R_2 &= \tilde{x}(u_0 - u_2) + \tilde{y}(v_0 - v_2) + \tilde{z}(w_0 - w_2). \end{aligned} \tag{2.53}$$

The applied $1, 2$ lower indices denote variables defined from left and right states, depending on the sign of the corresponding eigenvalue:

$$\begin{cases} \mathbf{U}_0 = \frac{\mathbf{U}_L + \mathbf{U}_R}{2} - \text{sign}(\lambda_0)\frac{\mathbf{U}_R - \mathbf{U}_L}{2} \\ \mathbf{U}_1 = \mathbf{U}_L \\ \mathbf{U}_2 = \mathbf{U}_R \end{cases} \tag{2.54}$$

2.2.7 Higher-Order Interpolation

The applied CB method results in characteristic variables $(\tilde{p}, \tilde{u}, \tilde{v}, \tilde{w})$ reconstructed on cell faces. In order to calculate these reconstructed "tilde" values, we need the set of primitive variables (p_l, u_l, v_l, w_l) for each eigenvalue $(l = 0, 1, 2)$. Consider the relevant 1-D scentil presented by figure 2.3. Let us specify two states of the concerning intercell characteristic variables: left (L) and right (R) [2].

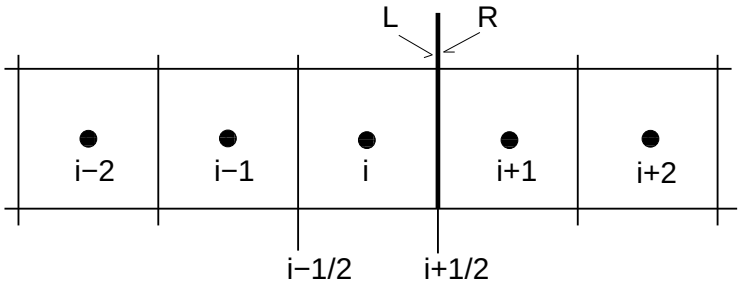

F 2.3: 1-D scentil used for higher-order interpolation (schematic adapted from [2])

Utilising third-order reconstruction scheme, the corresponding (L) and (R) states on cell face $(i + 1/2)$ are defined as ([74, 75]):

$$\mathbf{U}_{L,\,i+1/2} = \frac{5}{6}\mathbf{U}_i - \frac{1}{6}\mathbf{U}_{i-1} + \frac{1}{3}\mathbf{U}_{i+1}, \tag{2.55}$$

and

$$\mathbf{U}_{R,\,i+1/2} = \frac{5}{6}\mathbf{U}_{i+1} - \frac{1}{6}\mathbf{U}_{i+2} + \frac{1}{3}\mathbf{U}_i. \tag{2.56}$$

These interpolation formulas are directly utilised to determine the primitive variables (p_l, u_l, v_l, w_l) for each of the eigenvalues $(l = 0, 1, 2)$ of the system. The selection of the left (L) or right (R) state values depends on the sign of the local intercell eigenvalue:

$$\mathbf{U}_{l,i+1/2} = \frac{1}{2}\Big[(1 + \mathrm{sign}(\lambda_l))\mathbf{U}_{R,\,i+1/2} + (1 - \mathrm{sign}(\lambda_l))\mathbf{U}_{L,\,i+1/2}\Big]. \tag{2.57}$$

2.2.8 Flux Differencing

During the numerical calculations, both viscous (V) and intercell advective (I) fluxes were defined at the cell faces. Once the reconstructed characteristic variables $\tilde{\mathbf{U}}$ are available, the concerning advective flux can be determined as $\mathbf{E}_{\mathrm{I}\,i+1/2} = [\mathbf{E}_{\mathrm{I}}(\tilde{\mathbf{U}})]_{i+1/2}$. According to the applied notation schema, the inviscid intercell flux in ξ direction was defined in the cell center (i, j, k) and calculated as [2]:

$$\frac{\partial \mathbf{E}_{\mathrm{I}}}{\partial \xi} = \frac{(\mathbf{E}_{\mathrm{I}})_{i+\frac{1}{2},j,k} - (\mathbf{E}_{\mathrm{I}})_{i-\frac{1}{2},j,k}}{\Delta \xi}, \tag{2.58}$$

with figure 2.4 illustrating the corresponding scentil in ξ direction.

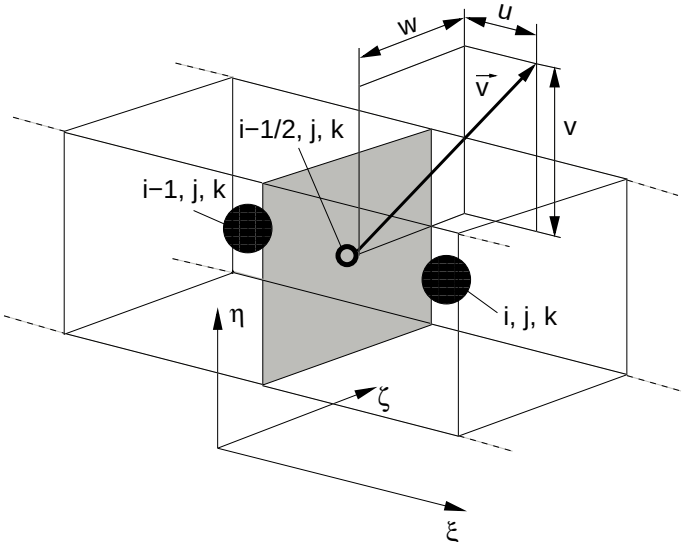

F 2.4: Scentil in ξ direction

Concerning viscous fluxes (V) were computed using the second order centered approximation. Advective fluxes (I) were calculated utilising the reconstructed characteristic-based variables ([2]), combined with the third order variables reconstruction ([74]), as discussed earlier.

2.2.9 Time Stepping

The integration in pseudo-time for the artificial compressibility formulation was performed using the fourth-order Runge-Kutta method (e.g. [74, 75]). In order to simplify the formulas, the following short-hand notation has been introduced:

$$\mathbf{RHS}(\mathbf{U}) = -\frac{\partial J\mathbf{U}_r}{\partial t} + \frac{\partial \mathbf{E}_\mathrm{V}}{\partial \xi} + \frac{\partial \mathbf{F}_\mathrm{V}}{\partial \eta} + \frac{\partial \mathbf{G}_\mathrm{V}}{\partial \zeta} - \frac{\partial \mathbf{E}_\mathrm{I}}{\partial \xi} - \frac{\partial \mathbf{F}_\mathrm{I}}{\partial \eta} - \frac{\partial \mathbf{G}_\mathrm{I}}{\partial \zeta} + \mathbf{F} \quad (2.59)$$

With the introduced simplified notation, the basic equation 2.25 is written as:

$$\frac{\partial \mathbf{U}}{\partial \tau} = \mathbf{RHS}(\mathbf{U}). \quad (2.60)$$

Therefore, algorithm for the pseudo-time stepping is as follows [2]:

$$\begin{aligned} \mathbf{U}_1 &= \mathbf{U}_n \\ \mathbf{U}_2 &= \mathbf{U}_n - \tfrac{\Delta\tau}{2}\Big(\mathbf{RHS}(\mathbf{U}_1)\Big) \\ \mathbf{U}_3 &= \mathbf{U}_n - \tfrac{\Delta\tau}{2}\Big(\mathbf{RHS}(\mathbf{U}_2)\Big) \\ \mathbf{U}_4 &= \mathbf{U}_n - \tfrac{\Delta\tau}{2}\Big(\mathbf{RHS}(\mathbf{U}_3)\Big) \end{aligned} \quad (2.61)$$

$$\mathbf{U}_{n+1} = \mathbf{U}_n - \frac{\Delta\tau}{6}\Big(\mathbf{RHS}(\mathbf{U}_1) + 2\,\mathbf{RHS}(\mathbf{U}_2) + 2\,\mathbf{RHS}(\mathbf{U}_3) + \mathbf{RHS}(\mathbf{U}_4)\Big) \quad (2.62)$$

2.3 Solution of Equations for Flexible Polymers

Polymers with no secondary structure are usually flexible and resemble weak resistance upon external stretching forces.

A typical example of flexible macromolecules is single-stranded DNA. Experimental observations of Smith and Bustamante (see [59, 61]) confirmed that single-stranded DNA's response to applied stretching force is negligible. The molecules can be extended almost to their contour lengths, without considerable resistance against the stretching forces.

Focusing on the numerical simulation of flexible molecules, the most suitable mechanical representation is the bead-rod structure model. Bead-rod models describe the macromolecule as a series of spherical particles connected with non-extensible, freely rotating rods.

Beads act as force centers, but also serve as connection points. Rods are connecting elements without any structure-specific orientation. Their bare purpose is to preserve the distance between two beads. Since these molecules experience negligible forces resulting from the molecular structure, $\boldsymbol{\phi}_n$ non-hydrodynamic force is considered to be zero in bead-rod models.

2.3.1 Bead-Rod Model Equations

Modelling polymers as bead-rod structures however raises unique requirements concerning the numerical implementation of the model. In order to preserve the molecule structure dictated by the micromechanical model, pre-defined lengths of the connecting rods must be maintained:

$$|\boldsymbol{r}_n - \boldsymbol{r}_{n-1}| = a_{n,n-1}\,, \tag{2.63}$$

with $a_{n,n-1}$ pre-defined rod length. The index n runs from the second bead of the structure to the last one.

During the numerical calculations, nondimensional governing equation 2.10 is integrated in time in order to determine bead velocities and positions. It is important to emphasise that most of the relevant quantities are nondimensional, except the particle mass m_n and the necessary scaling factors, U and L. In the absence of non-hydrodynamic forces $\boldsymbol{\phi}_n$, analytical integration of 2.10 results in the formula for bead velocity n [45, 50]:

$$\boldsymbol{v}_n(t+\Delta t) = \boldsymbol{u}(\boldsymbol{r}_n) + (\boldsymbol{v}_n(t) - \boldsymbol{u}(\boldsymbol{r}_n))\exp(-\gamma_n \Delta t) + \sigma_v \boldsymbol{R}_{v,n}(\Delta t), \qquad (2.64)$$

with $\sigma_v = \sqrt{\frac{2\gamma_n k_B T}{m_n UL}}$ [45, 50]. Having the formula for bead velocities in hand, bead positions are obtained from analytical integration of 2.64 in the form of [45, 50]:

$$\begin{aligned} \boldsymbol{r}_n(t+\Delta t) &= \boldsymbol{r}_n(t) + (\boldsymbol{v}_n(t) - \boldsymbol{u}(\boldsymbol{r}_n))\frac{(1-\exp(-\gamma_n \Delta t))}{\gamma_n} + \\ &+ \boldsymbol{u}(\boldsymbol{r}_n)\Delta t + \sigma_x \boldsymbol{R}_{x,n}(\Delta t), \end{aligned} \qquad (2.65)$$

with $\sigma_x = \sqrt{\frac{2k_B T}{\gamma_n m_n UL}}$ [45, 50], $\boldsymbol{R}_{v,n}(\Delta t)$ and $\boldsymbol{R}_{x,n}(\Delta t)$ vectors of independent random numbers drawn from Gaussian distributions with zero mean and variances:

$$\langle R_{v,n}(\Delta t)^2 \rangle = \frac{L}{2\gamma_n U}(1 - \exp(-2\gamma_n \Delta t)) \qquad (2.66)$$

$$\langle R_{x,n}(\Delta t)^2 \rangle = \frac{L}{2\gamma_n U}(2\gamma_n \Delta t - \exp(-2\gamma_n \Delta t) + 4\exp(-\gamma_n \Delta t) - 3). \qquad (2.67)$$

Basic equation 2.1 does not include rod length criteria implicitly. Therefore, bead positions 2.65 resulting from numerical integration of 2.1 do not necessarily satisfy rod length requirements.

In order to preserve dimensions of the molecule, rod lengths must be

maintained explicitly. This is usually carried out by utilising an additional algorithm to adjust the calculated bead positions. The utilised particle corrector routine ensures that bead positions satisfy the requirements regarding the molecule structure at the current time level. Application of a corrector stage results in a two-step, predictor-corrector style algorithm.

2.3.2 Particle Corrector Method

The governing idea of particle corrector methods is the introduction of artificial tension forces along the connecting elements to re-position the beads. Essentially, this approach can be interpreted as a slight modification of basic equation 2.1:

$$m_n \frac{d^2 \boldsymbol{r}_n}{dt^2} = \boldsymbol{f}_n + \boldsymbol{g}_n \,, \tag{2.68}$$

with $\boldsymbol{g}_n$ artificial constraint force arising from bond deviations defined as:

$$\sigma_{n,n-1} = (\boldsymbol{r}_n - \boldsymbol{r}_{n-1})^2 - a_{n,n-1}^2 \qquad n = 1..N, \tag{2.69}$$

where $a_{n,n-1}$ is the pre-defined bond length. When length of the $(n, n-1)^{th}$ bond $|\boldsymbol{r}_n - \boldsymbol{r}_{n-1}|$ is equal to the prescribed value, there is no constraint force acting on the n^{th} and $n-1^{th}$ beads due to this bond.

The introduced constraint forces apparently modify the Langevin equation 2.1 describing the behaviour of beads. However, their effect materialises only in the additional particle corrector step. Therefore, application of constraint forces does not effect the calculation of particle velocities 2.64 and positions 2.65 in the predictor step.

The effect of artificial tension forces is considered in the corrector step, where the calculated unconstrained particle velocities and positions are modified to satisfy the geometrical constraints. This predictor-corrector

type approach leads to the following two step algorithm:

1. Calculate $\boldsymbol{r}_n{}'(t+\Delta t)$ unconstrained positions of beads from Eq. 2.65, neglecting the effect of constraint forces.

2. Determine the correction vectors $\delta\boldsymbol{r}_n(t+\Delta t)$ and construct the constrained particle positions $\boldsymbol{r}_n(t+\Delta t) = \boldsymbol{r}_n{}'(t+\Delta t) + \delta\boldsymbol{r}_n(t+\Delta t)$

Various approaches are available for the construction of total constraint force $\boldsymbol{g}_n$. Let us assume that each constraint force component acts along the rod connecting corresponding beads. Suppose that the force magnitude is proportional to the difference between the prescribed and actual bond lengths. Based on these assumptions, the general constraint force acting on the n^{th} bead is written as [50]:

$$\boldsymbol{g}_n = -\sum_{i=1}^{N} \lambda_{n,i} \frac{\partial \sigma_{n,i}}{\partial \boldsymbol{r}_n}\,, \tag{2.70}$$

where $\lambda_{n,i}$ parameters are proportional to the force magnitude, $\frac{\partial \sigma_{n,i}}{\partial \boldsymbol{r}_n}$ determines the orientation of individual constraint forces acting on bead n and the sum runs for all bonds.

2.3.3 SHAKE Algorithm

In the widely used SHAKE particle corrector algorithm, $\lambda_{n,i}$ parameters are treated as Lagrangian multipliers ([85]). Values of the Lagrangian multipliers are determined by the requirement that the corresponding length constraints in 2.69 are satisfied exactly on each time step.

Correction vectors are resulted from definition of the constraint force

2.70 and written as [85]:

$$\delta \boldsymbol{r}_n(t + \Delta t) = -\frac{\Delta t^2}{2m_n} \sum_{i=1}^{N} \lambda_{n,i} \frac{\partial \sigma_{n,i}}{\partial \boldsymbol{r}_n}\bigg|_t \,, \tag{2.71}$$

where

$$\frac{\partial \sigma_{n,i}}{\partial \boldsymbol{r}_n}\bigg|_t = \frac{\partial \left(\left[\boldsymbol{r}_n(t) - \boldsymbol{r}_i(t) \right]^2 - a_{n,i}^2 \right)}{\partial \boldsymbol{r}_n(t)} \,. \tag{2.72}$$

As 2.72 demonstrates, direction of constraint forces in the SHAKE particle corrector is determined by bond orientations taken from the previous time step.

Such definition of correction vectors is characteristic to SHAKE algorithm and forms a significant difference compared to a similar corrector routine, FALCO. After substituting the constrained particle coordinates evaluated at $t + \Delta t$ and rearranging the terms, the constraints equation 2.69 becomes

$$2(\boldsymbol{r}_n{}' - \boldsymbol{r}_i{}') \cdot (\delta \boldsymbol{r}_n - \delta \boldsymbol{r}_i) + (\delta \boldsymbol{r}_n - \delta \boldsymbol{r}_i)^2 = a_{n,i}^2 - (\boldsymbol{r}_n - \boldsymbol{r}_i)^2 \,. \tag{2.73}$$

Equations for correction vectors 2.71 and geometrical constraints 2.73 result in a system of $N - 1$ quadratic equations for $\lambda_{n,i}$ values. In order to avoid direct numerical solution of the resulting system, SHAKE particle corrector employs an iterative solution of the following linearised system on each time step:

$$2(\boldsymbol{r}_n{}' - \boldsymbol{r}_i{}') \cdot \left(\delta \boldsymbol{r}_n^{(l)} - \delta \boldsymbol{r}_i^{(l)} \right) = a_{n,i}^2 - (\boldsymbol{r}_n - \boldsymbol{r}_i)^2 - \left(\delta \boldsymbol{r}_n^{(l-1)} - \delta \boldsymbol{r}_i^{(l-1)} \right)^2, \tag{2.74}$$

where $l - 1$ upper index refers to available corrections calculated using previous iteration step $\lambda_{n,i}^{(l-1)}$ values, and index l refers to correction vectors at the current iteration step. The solution is initialised using $\lambda_{n,i}^{0} = 0$. Once

the iterations have converged, the resulting $\lambda_{n,i}$ values are used to construct the correction vectors 2.71.

2.3.4 FALCO Algorithm

SHAKE is widely used in Molecular Dynamics simulations. However, the algorithm has a limited convergence range and may fail to converge when the initial guess is far from the corrected particle position.

While this problem usually does not occur in Molecular Dynamics simulations, it has been previously observed in meta-model simulations (see for example [45]). The complications which arise from the limited convergence range, namely the restrictions on the time step of unsteady coupled simulations prompted the development of the FALCO corrector.

In the FALCO (FAst Linear COrrector) particle corrector the particle positions are iteratively determined using the mass-weighted deviation of the current bond length from the prescribed one as follows:

$$\begin{aligned} \delta \boldsymbol{r}_n(t+\Delta t)^{(l)} \;=\; & -\frac{\epsilon}{2m_n}\Big(\min\left(m_{n-1}, m_n\right) DL_{n-1,n}^{(l-1)} \boldsymbol{n}_{n-1,n}^{(l-1)} - \\ & \min\left(m_n, m_{n+1}\right) DL_{n,n+1}^{(l-1)} \boldsymbol{n}_{n,n+1}^{(l-1)} \Big), \end{aligned} \tag{2.75}$$

where $DL_{n-1,n}^{(l-1)}$ denotes the elongation of the bond between particles n and $n-1$ at $l-1$ iteration given by:

$$DL_{n-1,n}^{(l-1)} = \sqrt{\left[\left(\boldsymbol{r}_{n-1}{}' + \delta \boldsymbol{r}_{n-1}^{(l-1)}\right) - \left(\boldsymbol{r}_n{}' + \delta \boldsymbol{r}_n^{(l-1)}\right)\right]^2} - a_{n-1,n}\,, \tag{2.76}$$

with $\boldsymbol{n}_{n-1,n}^{(l-1)}$ unit vector along the direction of the bond between particles n and $n-1$ in the $l-1^{th}$ iteration step. $\epsilon \in [0, 1]$ is the applied under-relaxation factor.

The relation of the FALCO corrector to SHAKE algorithm can be established by considering an analogy with Hooke's law [86] with the spring constant proportional to the bond length elongation. The force then is proportional to the bond elongation with the coefficient of proportionality $\lambda_{n,i}$ (2.70). If we define $\lambda_{n,i}$ to be proportional to the normalised bond elongation $DLN_{n,i}$

$$\lambda_{n,i}^{(l)} = \frac{\epsilon}{2} \cdot \min_{i \in bond} \left| \frac{m_i}{\Delta t^2} \right| \cdot DLN_{n,i} \tag{2.77}$$

$$DLN_{n,i} = \frac{\sqrt{\left[\left(\boldsymbol{r}_n{}' + \delta \boldsymbol{r}_n^{(l-1)}\right) - \left(\boldsymbol{r}_i{}' + \delta \boldsymbol{r}_i^{(l-1)}\right)\right]^2} - a_{n,i}}{\sqrt{\left[\left(\boldsymbol{r}_n{}' + \delta \boldsymbol{r}_n^{(l-1)}\right) - \left(\boldsymbol{r}_i{}' + \delta \boldsymbol{r}_i^{(l-1)}\right)\right]^2}} \tag{2.78}$$

and substitute this definition into the SHAKE correction formula 2.71, taking into account the bond constraints updated on each iteration

$$\left.\frac{\partial \sigma_{n,i}}{\partial \boldsymbol{r}_n}\right|_{t+\Delta t}^{(l)} = \frac{\partial\left(\left[\left(\boldsymbol{r}_n{}' + \delta \boldsymbol{r}_n^{(l-1)}\right) - \left(\boldsymbol{r}_i{}' + \delta \boldsymbol{r}_i^{(l-1)}\right)\right]^2 - a_{n,i}^2\right)}{\partial\left(\boldsymbol{r}_n{}' + \delta \boldsymbol{r}_n^{(l-1)}\right)}, \tag{2.79}$$

the FALCO update formula defined by 2.75 is resulted. As the formula illustrates, the FALCO algorithm updates the particle positions inside the iteration loop.

This leads to the the direction vectors being updated on each iteration as opposed to using the previous time-step direction vectors in SHAKE. This results reduced sensitivity of the particle corrector to the angular displacements of the bonds.

Figure 2.5 demonstrates the construction of corrector vectors defined by SHAKE and FALCO. According to formula 2.72, orientation of $\boldsymbol{g}_{i,j}^{SHK}$ corrector vector of the SHAKE algorithm is defined by previous time-step position vectors $\boldsymbol{r}_i(t)$ and $\boldsymbol{r}_j(t)$. Contrary to this practice, $\boldsymbol{g}_{i,j}^{FLC}$ corrector

vector of the FALCO algorithm is constructed by the most recent position vectors $\boldsymbol{r}_i\,'(t+\Delta t)$ and $\boldsymbol{r}_j\,'(t+\Delta t)$ updated in each iteration step (see formula 2.79).

The proposed FALCO formulation does not involve numerical solution of second-order equations, which leads to reduced storage requirements and increased computational efficiency.

Although SHAKE and FALCO particle correctors are closely related to each-other, dissimilarities of the numerical details result significant differences in the behaviour and performance of the two methods.

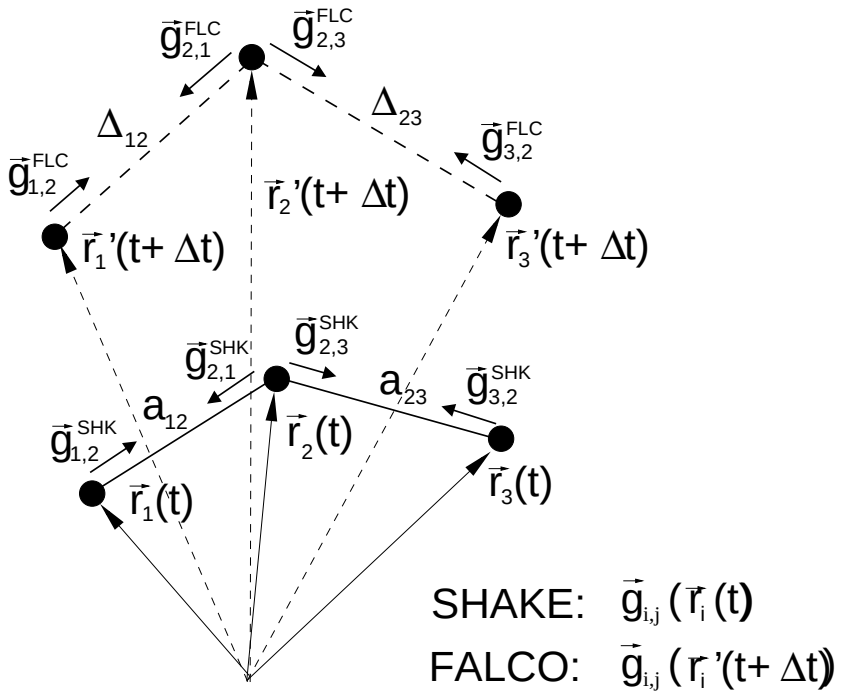

F 2.5: Construction of corrector vectors with SHAKE and FALCO

2.4 Solution of Equations for Elastic Polymers

Behaviour of macromolecules with strong secondary structure is highly influenced by inter-molecular forces arising from changes of molecular configuration. A typical example of macromolecules with considerable secondary structure is the class of double-stranded DNA molecules.

Due to their unique biological role, these macromolecules have received exceptional scientific attention. According to the mechanical measurements of dsDNAs carried out by Smith *et al.* [58], the molecules resemble structure-dependent restoring forces. The effect of the considered forces can be observed when equilibrium configuration of the molecule is violated. This typically occurs when molecules of interest are stretched by external forces.

Considering the numerical simulation of elastic macromolecules, the most accurate representation is the bead-spring model. The mechanical model is constructed from a series of beads connected with freely rotating, elastic bonds represented by springs. In such models, connecting elements are beads, also serving as force centers. Purpose of the applied springs is to model entropic elastic forces arising due to changes of the molecule structure.

2.4.1 Bead-Spring Model Equations

For the numerical calculation of bead velocities and positions, the nondimensional governing equation 2.10 is integrated in time. Considering the effect of entropic forces arising due to the molecular structure, analytical

integration of 2.10 results the formula for bead velocity n:

$$\begin{aligned} \boldsymbol{v}_n(t+\Delta t) &= \boldsymbol{u}(\boldsymbol{r}_n) + \left(\boldsymbol{v}_n(t) - \boldsymbol{u}(\boldsymbol{r}_n) - \frac{\boldsymbol{\phi}_n}{\gamma_n}\right)\exp(-\gamma_n \Delta t) + \\ &+ \frac{\boldsymbol{\phi}_n}{\gamma_n} + \sigma_v \boldsymbol{R}_{v,n}(\Delta t). \end{aligned} \tag{2.80}$$

Having the formula for bead velocities in hand, bead positions are obtained from analytical integration of 2.80 in the form of:

$$\begin{aligned} \boldsymbol{r}_n(t+\Delta t) &= \boldsymbol{r}_n(t) + \left(\boldsymbol{v}_n(t) - \boldsymbol{u}(\boldsymbol{r}_n) - \frac{\boldsymbol{\phi}_n}{\gamma_n}\right)\frac{\left(1-\exp(-\gamma_n \Delta t)\right)}{\gamma_n} + \\ &+ \left(\boldsymbol{u}(\boldsymbol{r}_n) + \frac{\boldsymbol{\phi}_n}{\gamma_n}\right)\Delta t + \sigma_x \boldsymbol{R}_{x,n}(\Delta t)\,, \end{aligned} \tag{2.81}$$

with the same notations as used for the bead-rod model equations. In equation 2.80 and 2.81, $\boldsymbol{\phi}_n$ denotes the dimensionless non-hydrodynamic force representing the effect of entropic elastic forces acting on bead n.

The overall nondimensional spring force $\boldsymbol{\phi}_n$ on bead n results from the contributions of the concerning springs $n-1$ and n connecting bead pairs $(n-1, n)$ and $(n, n+1)$, respectively. Spring forces are calculated explicitly. Considering the bead-spring model of double-stranded DNA, spring forces are described by WLC-PET 1.12 force-extension law. For the sake of the numerical calculations, WLC-PET 1.12 forces were consistently scaled with the relevant factor $L/m_n U^2$:

$$\begin{aligned} \boldsymbol{\phi}_n &= -F^{WLC-PET}(\boldsymbol{r}_{n-1}(t), \boldsymbol{r}_n(t)) \cdot \boldsymbol{n}(t)_{n-1,n} + \\ &+ F^{WLC-PET}(\boldsymbol{r}_n(t), \boldsymbol{r}_{n+1}(t)) \cdot \boldsymbol{n}(t)_{n,n+1}. \end{aligned} \tag{2.82}$$

Here, $F^{WLC-PET}(\boldsymbol{r}_{n-1}(t), \boldsymbol{r}_n(t))$ denotes the dimensionless force magnitude and $\boldsymbol{n}(t)_{n-1,n}$ denotes the relevant unit direction vector.

2.5 Implementation Details

This section is aimed to discuss technical details relevant to the implementation of meta-models. The applied modelling method is based on the dual description of the fluid-solute system. Therefore, the majority of practical questions are related to general information transfer.

However, apart from technical details of the two-way data transfer, realistic simulation of the transported mechanical structures arises questions related to near-wall treatment.

2.5.1 Euler-Lagrange Coupling

The meta-modelling technique successfully merges the continuum-based modelling of the solvent and the individual description of the transported micromechanical structures. The applied dual description of the solvent-solute system facilitated the combination of the Eulerian and Lagrangian description methods for the fluid phase and the transported structures.

Figure 2.6 demonstrates momentary positions of a Lagrangian structure on the grid of Eulerian cells. Cells filled with dark grey colour denote the cell containing the studied particle.

During the meta-model calculations, properties and flow variables of the fluid phase are calculated on the fixed arrangement of non-moving and non-deforming elementary volumes called computational cells. Pressure values, velocity components and material properties are defined in the center of each computational cell. Therefore, calculated flow parameters are assigned to fixed points of the geometrical space. This kind of representation of physical phenomena is called Eulerian description.

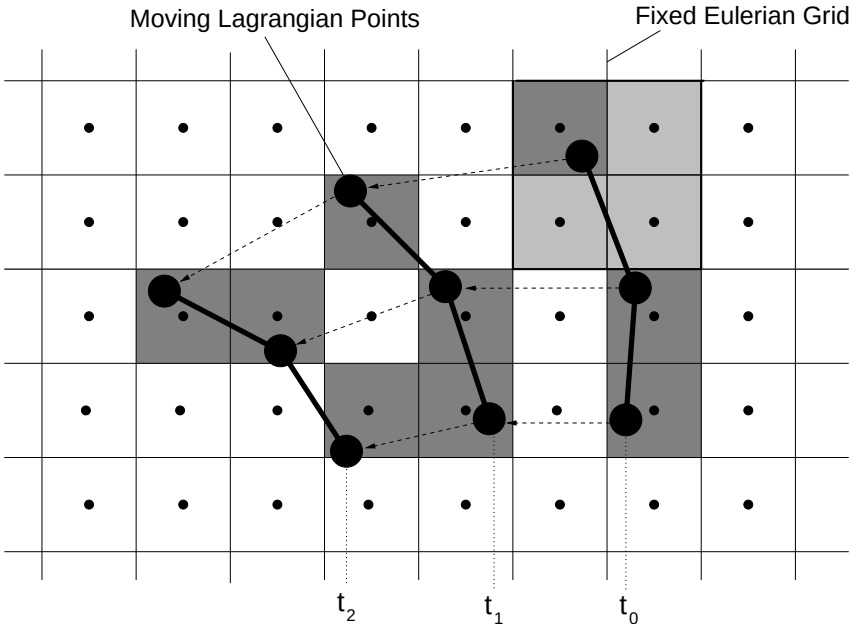

F 2.6: Moving bead-rod structure and the fixed computational cells

The considered micromechanical models are moving relative to the Eulerian cells. Parameters of the travelling structures are calculated concerning the actual coordinates of the moving beads. Contrarily to the Eulerian approach, parameters of the individual structures are not fixed in the metric space, but attached to the moving particles. This type of description is called Lagrangian approach.

Dual treatment of the carrier fluid and the transported solute requires two-way information exchange between the fixed Eulerian cells and the moving structures. Information transfer from the fluid phase to the structures is especially challenging, since particle coordinates do not necessarily coincide with cell centers. Convective velocity $\boldsymbol{u}(\boldsymbol{r}_n)$ of particle n at position $\boldsymbol{r}_n$ can be calculated utilising for example first order approximation:

$$\boldsymbol{u}(\boldsymbol{r}_n) = \boldsymbol{u}_p \,, \tag{2.83}$$

where p index denotes the cell containing the particle. Second-order approximation of particle velocity utilises fluid velocities defined at the center of neighbouring cells termed as "donors". In such case, convective ve-

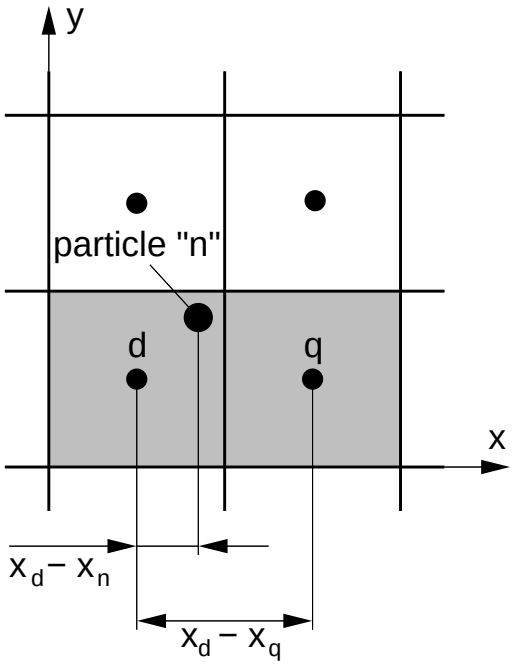

F 2.7: Scentil for second order velocity approximation

locity of particle n at position $\boldsymbol{r}_n$ is approximated as the weighted average of the concerning cell velocities:

$$\boldsymbol{u}(\boldsymbol{r}_n) = \sum_d wf_d \cdot \boldsymbol{u}_d \,, \tag{2.84}$$

with

$$wf_d = wz_d \cdot wy_d \cdot wx_d \,. \tag{2.85}$$

Here, wf_d weighting factors are the products of linear functions of spatial

coordinates:

$$
\begin{aligned}
wz_d &= \frac{|z_d - z_n|}{|z_d - z_q|} \\
wy_d &= \frac{|y_d - y_n|}{|y_d - y_q|} \\
wx_d &= \frac{|x_d - x_n|}{|x_d - x_q|}\,,
\end{aligned}
\tag{2.86}
$$

respectively. Here, index d runs over all donor cells and n corresponds to the investigated particle. Index q always denotes the concerning neighbouring cell in the relevant spatial direction.

2.5.2 Force Transfer Method

As it has been mentioned earlier, the total force acting on each bead is the sum of a hydrodynamic force - Stokes drag - and a random force originated from the Brownian motion of solvent molecules. Both forces represent the impact of the continuum phase exerted on the spherical particles of interest.

According to Newton's third law, the force acting on each bead results a counter-force acting on the fluid with the same magnitude and opposing direction. While the force experienced by individual beads is point-like by its nature, the concerning counter-force projected back to the fluid phase is distributed over the volume of surrounding cells.

From the total force acting on each particle, the additional volume force in the momentum equation is calculated as:

$$
\mathcal{F}(\boldsymbol{r}) = -\sum_n \boldsymbol{f}_n \, \delta_\epsilon(\boldsymbol{r} - \boldsymbol{r}_n) \tag{2.87}
$$

with δ_ϵ smoothed Dirac function of ϵ length scale. This function incorporates a division with the cell volume and therefore transforms the concerning point-like force $\boldsymbol{f}_n$ into a volumetric force field. During the numerical

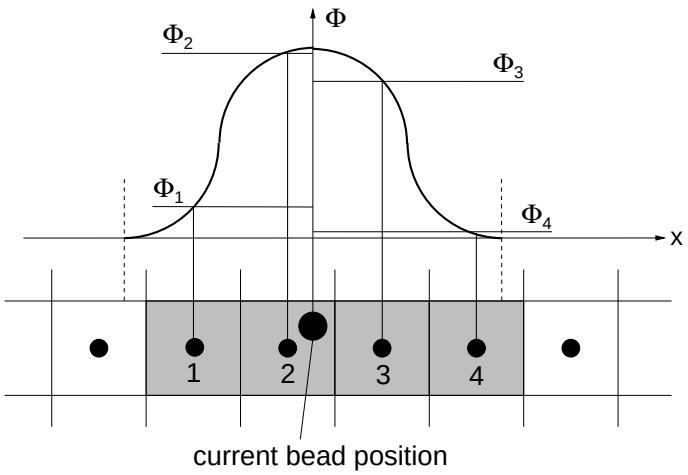

F 2.8: Schematic figure of the transfer function

calculations, discretised version of the Dirac function introduced by Zhu and Peskin [87] is applied to facilitate force transfer to the cell centers. Figure 2.8 demonstrates the involved cells and the applied function along coordinate x. Definition of the discrete Dirac function is given as [87]:

$$\delta_\epsilon(\boldsymbol{r}-\boldsymbol{r}_n)=\frac{1}{\Delta x\Delta y\Delta z}\Phi\left(\frac{x_{cc}-x_n}{\Delta x}\right)\Phi\left(\frac{y_{cc}-y_n}{\Delta y}\right)\Phi\left(\frac{z_{cc}-z_n}{\Delta z}\right) \tag{2.88}$$

where Δx, Δy and Δz are the dimensions of the actual cell, x_{cc}, y_{cc} and z_{cc} are the corresponding cell center coordinates and x_n, y_n and z_n represent the Cartesian coordinates of bead n. Φ transfer function is defined as a monotonically decreasing trigonometric relation with a cutoff distance. For x spatial direction, Φ is written as:

$$\Phi\left(\frac{x_{cc}-x_n}{\Delta x}\right)=\begin{cases}\frac{1}{4}\left(1+\cos\left(\frac{\pi}{2}\frac{(x_{cc}-x_n)}{\Delta x}\right)\right) & \text{if } \frac{(x_{cc}-x_n)}{\Delta x}\leq 2\\ 0 & \text{otherwise}\end{cases} \tag{2.89}$$

Transfer functions for the *y* and *z* spatial dimensions are constructed in the same fashion, respectively.

2.5.3 Wall Treatment

Another important topic is the behaviour of particles advancing towards a solid wall. It may occur that the trajectory $\boldsymbol{r}_n(t) \rightarrow \boldsymbol{r}_n(t + \Delta t)$ carries bead *n* across the boundary of the fluid domain. In reality, particles cannot penetrate solid obstacles, therefore such events must be avoided during the numerical calculations too.

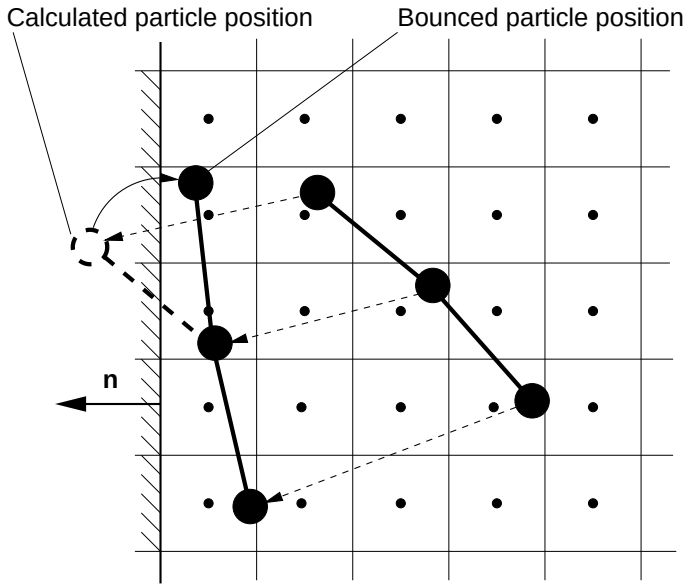

F 2.9: Schematic figure of wall bouncing

In the numerical implementation, we assume perfectly elastic particle bounce-off from the wall. Calculated particle trajectories are continuosly monitored as time progresses. When a collision is forecast, the impact position $\boldsymbol{r}_{n\,\mathrm{impact}}$ and collision time $\Delta t_{\mathrm{impact}}$ is calculated in the first step. As perfect elastic particle bounce-off is assumed, new particle velocity and

position is calculated as follows:

$$\boldsymbol{v}_n(t + \Delta t) = \boldsymbol{v}_n - 2\,(\boldsymbol{n} \cdot \boldsymbol{v}_n) \cdot \boldsymbol{n} \tag{2.90}$$

$$\boldsymbol{r}_n(t + \Delta t) = \boldsymbol{r}_{n\,\text{impact}} + (\Delta t - \Delta t_{\text{impact}}) \cdot \boldsymbol{v}_n(t + \Delta t) \tag{2.91}$$

where $\boldsymbol{n}$ in the unit wall normal vector pointing outwards from the computational domain. Figure 2.9 demonstrates the elastic particle bounce-off mechanism. The reflected particle positions normally do not satisfy the length constraints 2.63. Therefore, particle correction algorithm is applied after the wall-bounce event to enforce these conditions.

2.5.4 Random Generator

Brownian motion occurs when fine scale behaviour of a microscopic particle in solvent is considered. The phenomenon can be observed in cases when the size of the investigated particle is several orders larger than the surrounding solvent molecules.

Brownian motion of a micro size particle is induced by carrier liquid molecules, randomly colliding against the considered particle. Figure 2.10 illustrates the collission of solvent molecules and the resulting stochastic motion of the transported particle. Every single collission results momen-

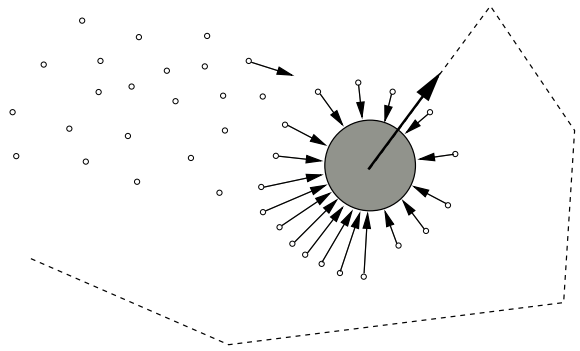

F 2.10: Sketch of the Brownian motion of a microscopic particle

tum exchange between the smaller solvent molecules and the larger particle. Due to the high, but limited number of collisions, the net momentum transferred to the particle per unit time will not be zero. This results in the acceleration of the particle.

The final effect is that the bigger particle immersed in liquid is subjected to erratic motion, similar to thermal agitation. Although molecule collissions are rapid and therefore time sales are very short, the resulting fine scale motion of a larger immersed particle is a much slower process. The investigated phenomenon describes longer time statistics of a large number of collissions.

Since rapid individual molecule collissions are stochastic, statistical average of such spontaneous events also results random motion on longer time scales. The effect of solvent molecules stochastic motion on the immersed particle is represented by the random force component $\varphi_n(t)$ in the governing equations for the Langevin beads. The action of such stochastic force is modelled using a random number generator.

Numerical implementation of the random generator is based on the polar version of the Box-Muller transformation [88, 89]. This algorithm provides transformation of numbers with normal distributions into Gaussian distributions. Pseudo-algorithm of the polar Box-Muller transformation is as follows:

```
   ! Source: http://www.taygeta.com/random/gaussian.html
do
{
      ! Generate normal distribution random numbers
      y1 = 2.0 * rand() - 1.0
      y2 = 2.0 * rand() - 1.0
      ! Calculate w
      w = (y1*y1) + (y2*y2)
}
! Stability requirement
while (w .GE. 1.0)

w = sqrt ( ( -2.0 * ln(w) ) / w )
! Gaussian random numbers with 0 mean and variance 1.0
z1 = y1 * w
z2 = y2 * w

! Transform numbers into prescribed mean and variance
x = delta * z1 + mu
```

where "x" is a random number possessing Gaussain distribution around "mu" mean and "delta" variance.

Figure 2.11 shows the Gaussian distribution of $1,000,000$ samples with zero mean and variance of $\delta = 10.0$, generated with the polar Box-Muller algorithm. In order to avoid numerical over- and undershoots, an upper cutoff limit for the generated radom numbers is defined as $\lim_{\text{up}} = 3\delta$ and the lower limit of the values is defined as $\lim_{\text{low}} = -3\delta$.

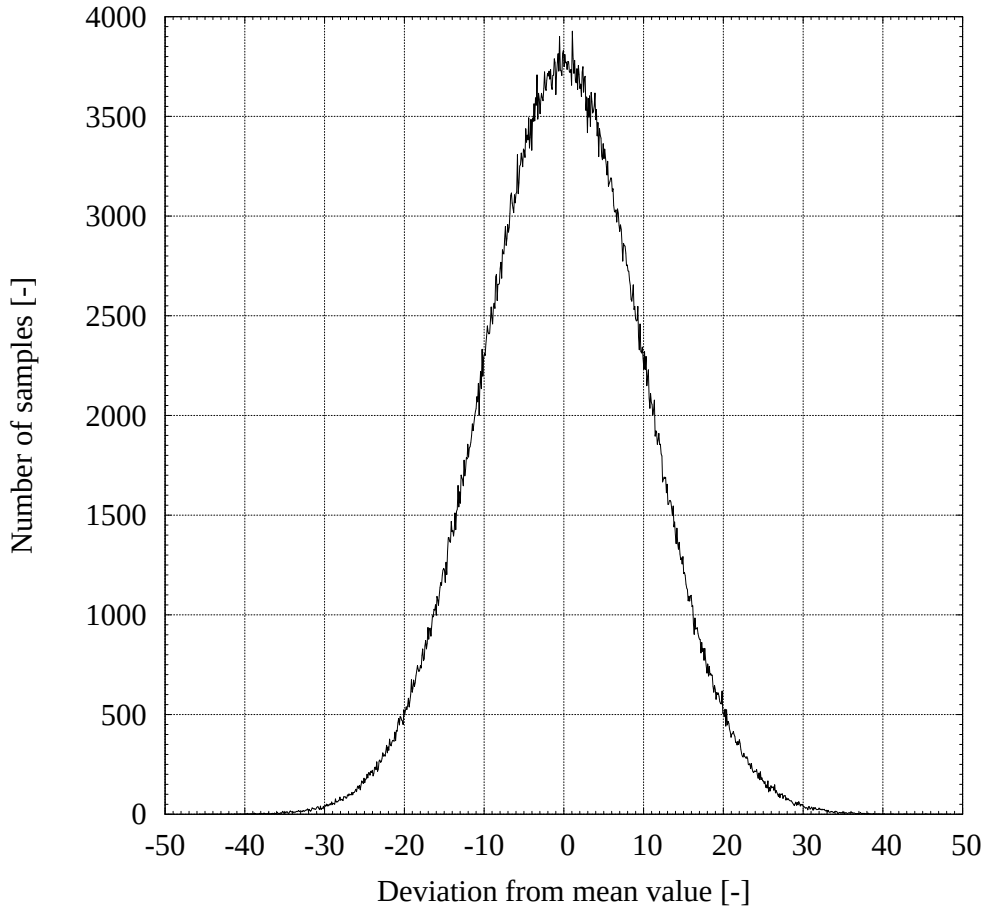

F 2.11: Gaussian distribution of 1,000,000 samples generated by polar Box-Muller method

Model Verification Studies

3

Model Verification Studies

In chapter 1, detailed investigation of the available modelling approaches has been carried out. The study concluded that meta-modelling technique is the most suitable numerical tool to describe processes in the considered sensor device. In order to utilise the developed modelling tool to support engineering design, extensive verification and validation of the method is necessary.

This chapter is aimed to provide thorough validation of the introduced meta-modelling technique. During the investigations, a series of numerical tests have been carried out to verify and validate specific parts of the models, stand-alone algorithms and the overall modelling approach. The considered studies have been performed in a systematic way to ensure consistency.

The performed investigations involved the verification of both bead-rod and bead-spring structure models. During the bead-rod model tests, numerical performance of the developed FALCO particle corrector method has also been investigated. Results of the FALCO algorithm have been compared against the widely used SHAKE method.

3.1 Verification of Bead-Rod Structure Models

This section is aimed to validate the developed FALCO particle corrector method [90] and verify its numerical implementation. Particle corrector methods are utilised when macromolecules are modeled using bead-rod mechanical structures.

In the considered meta-modelling technique, behaviour of bead-rod structures is described by the Langevin equation 2.1. It is important to emphasise that basic equation 2.1 models the motion of microbeads according to concerning macroscopic and microscopic forces. The Langevin equation alone does not provide the description of the considered micromechanical structures.

Description of the bead-rod models requires constraints to preserve the molecule structure. To this aim, particle corrector methods are utilised. Sole purpose of the applied particle corrector algorithm is to ensure that prescribed rod lengths are maintained during the numerical simulations.

Let us consider particle corrector methods as stand-alone algorithms. Their objective is to re-position two points of the metric space in such a way, that the obtained new positions satisfy pre-defined length constraints.

In order to validate the FALCO particle corrector and illustrate its superior stability, two different tests have been performed. Initially, the validation of the algorithm is carried out for a rotating dumbbell problem [91]. For this problem, the analytic solution is readily available. In this test case, the mechanical model is forced to rotate by a steady vortex.

The second test case considers a more complicated scenario of a biomolecule transport in a lid-driven cavity flow. For the this case, FALCO results are compared with the results obtained with the SHAKE particle corrector.

3.1.1 Rotating Dumbbell Problem

Theorem of zero net hydrodynamic force [91] declares that rotation of an asymmetric body about any axis going through its center of hydrodynamic torque C results in zero net hydrodynamic force. Hydrodynamic torque center C is defined as a point where the torque $\boldsymbol{T}_C$ vanishes in case of placing a fixed dumbbell into a uniform homogeneous velocity field.

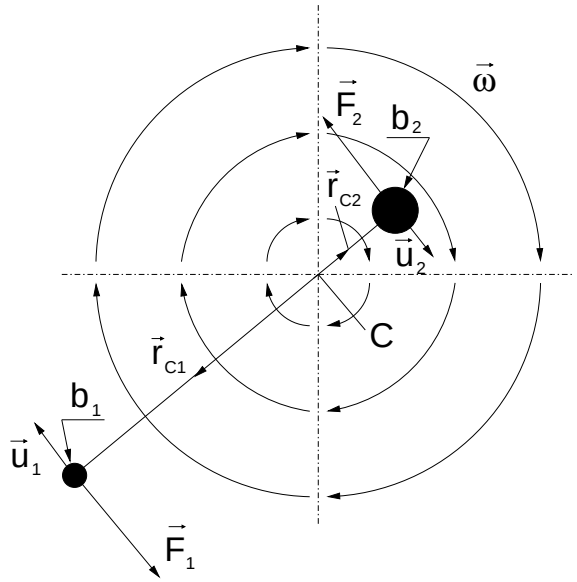

F 3.1: Schematic of the rotating dumbbell problem

Consider an asymmetric dumbbell in a fixed vortex with angular velocity $\boldsymbol{\omega}$ about an axis passing through C (Figure 3.1). The generated flow field imposes bead 1 and 2 to move through the surrounding fluid with velocities $\boldsymbol{u}_1$ and $\boldsymbol{u}_2$ respectively. Due to the motion, the beads experience Stokes drag forces

$$\boldsymbol{F}_i = -6\pi\eta b_i \boldsymbol{u}_i, \qquad i = 1, 2 \tag{3.1}$$

acting through their centers. Here, η denotes the dynamic viscosity and b_i

is the concerning bead radius. The velocities are given by

$$\boldsymbol{u}_i = \boldsymbol{\omega} \times \boldsymbol{r}_{Ci}, \qquad i = 1, 2 \tag{3.2}$$

with total force

$$\boldsymbol{F} = -6\pi\eta\boldsymbol{\omega} \times (b_1 \boldsymbol{r}_{C1} + b_2 \boldsymbol{r}_{C2}) \,. \tag{3.3}$$

The location of the hydrodynamic torque center C is calculated from the following relation

$$\boldsymbol{r}_{C1} = -\frac{b_2}{b_1} \boldsymbol{r}_{C2}. \tag{3.4}$$

Substitution of this relation into the formula for the total force 3.3 leads to $\boldsymbol{F} = \boldsymbol{0}$, in accordance with the general theorem.

An initially resting dumbbell placed into a steady vortex should start rotating around its hydrodynamic torque center C. Angular velocity of the structure should gradually increase until reaching the flow velocity. The steady state is reached when the angular velocity of the dumbbell matches the rotational velocity of the generating flow.

The simulation of this problem validates the implementation of the rigid bond constraint. In the absence of the bond constraint, drag forces would result in spiral particle pathlines. Furthermore, inconsistent or biased particle corrector algorithm would result in distorted particle trajectories.

To verify the FALCO algorithm, the accelerating dumbbell problem has been computed for the beads with the radius ratio $b_2/b_1 = 2.0$ and constant density coresponding to bead mass ratio of $m_2/m_1 = 8.0$. The angular velocity of the clockwise rotating vortex was set to 1.0. The bond length was equal to 0.2. The bead orbits determined by 627 time steps formed two concentric circles (Figure 3.2).

The integration error for the time step of $\Delta t = 0.01$ lead to the orbit

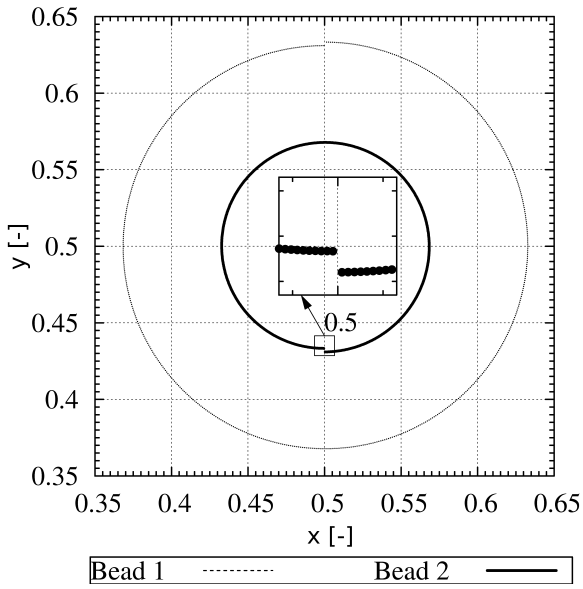

F 3.2: Calculated trajectories of the rotating dumbbell beads

displacement of 1% after a complete circle. Figure 3.3 shows the deviation of the calculated bond length from the exact value, normalised by the prescribed bond length (DLN_{12}). While FALCO proven to be stable during this test, we were unable to perform the same study using SHAKE corrector, even if the time step was reduced by 7 orders of magnitude, resulting $\Delta t = 10^{-9}$.

3.1.2 Comparison of SHAKE versus FALCO

In order to demonstrate the stability of the new corrector method, numerical simulation of an ssDNA strand is performed in a square lid-driven cavity flow. Using the bead-rod model, the ssDNA segment is represented by 3 beads connected with rigid and freely rotating rods. Simulations were performed for two different values of the time step with both the SHAKE and the FALCO particle correctors.

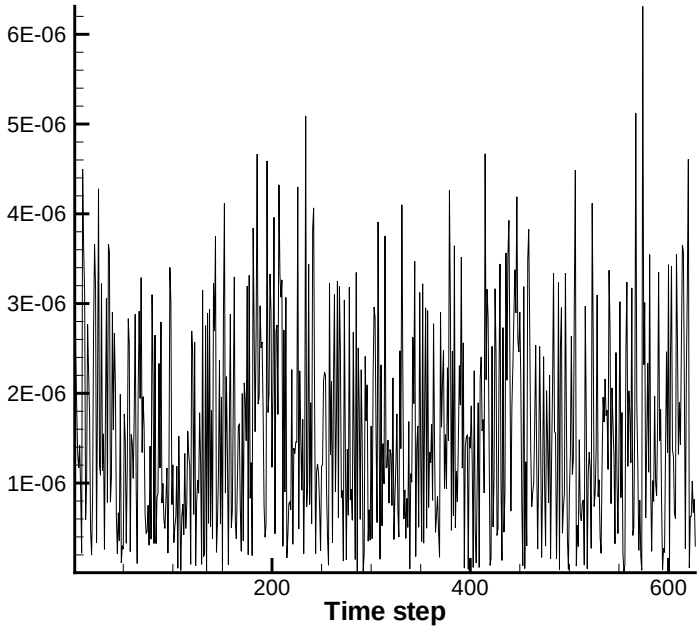

F 3.3: Normalised bond length deviation from the prescribed dumbbell length

At time $t = 0$ the ssDNA strand was injected into a developed micro-cavity flow with the Reynolds number of 10 based on the cavity depth L and lid velocity U. The ssDNA was aligned vertically, downwards from the starting point of $x_0 = 0.5, y_0 = 0.2$.

Since the primary aim of the test case was to evaluate the convergence range of the algorithm, the force exerted on the fluid flow by the ssDNA was neglected in order to simplify the problem. Estimates performed for the conditions indicate that this external force is $O\left(10^4 - 10^7\right)$ smaller than the convective and viscous terms.

The stochastic Brownian force acting on the beads of the mechanical model (see, for example, [45]) was neglected in order to enable direct comparison of the results obtained with different particle correctors. Considering motion of the investigated Brownian particles in fluid at room temperature, stochastic forces are $O\left(10^6\right)$ smaller compared to viscous drag

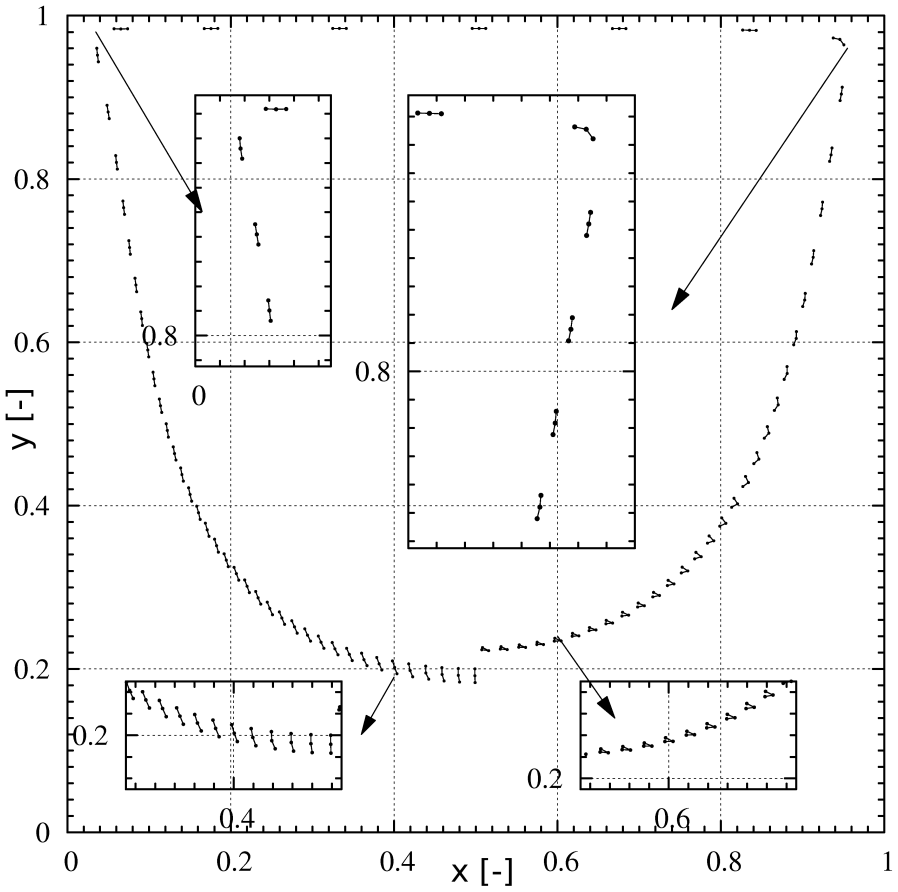

F 3.4: ssDNA positions obtained with FALCO, $\Delta t = 0.01$

forces.

Under these assumptions the equations determining the motion of the beads without constraint forces reduce to

$$m_n \frac{d^2 \boldsymbol{r}_n}{dt^2} = 6\pi\eta b_n \left(\boldsymbol{v}(\boldsymbol{r}_n) - \boldsymbol{u}_n\right) \qquad n = 1..3 \tag{3.5}$$

The corresponding length constraints are given by

$$|\boldsymbol{r}_n - \boldsymbol{r}_{n+1}| = a_{n,n+1} \, . \tag{3.6}$$

The density of the beads, bond lengths and bead radii were obtained

from the experimental data published by Tothova *et al.* [92], which yields the following bead parameters normalised by the fluid density ρ at room temperature and the cavity depth of $L = 1\mu m$

$$\rho_{1-3} = 1.22 \cdot 10^{-8},\ b_{1-3} = 3.9 \cdot 10^{-3},\ a_{12} = a_{23} = 8.3 \cdot 10^{-3}. \qquad (3.7)$$

The flow was computed on a uniform orthogonal grid comprising 64×64 computational cells. The force acting on the ssDNA beads was obtained based on the volume-averaged flow velocity in the corresponding flow cell. No-slip boundary conditions were imposed on the cavity walls. The computations were performed with $\Delta t = 0.05$ and $\Delta t = 0.01$.

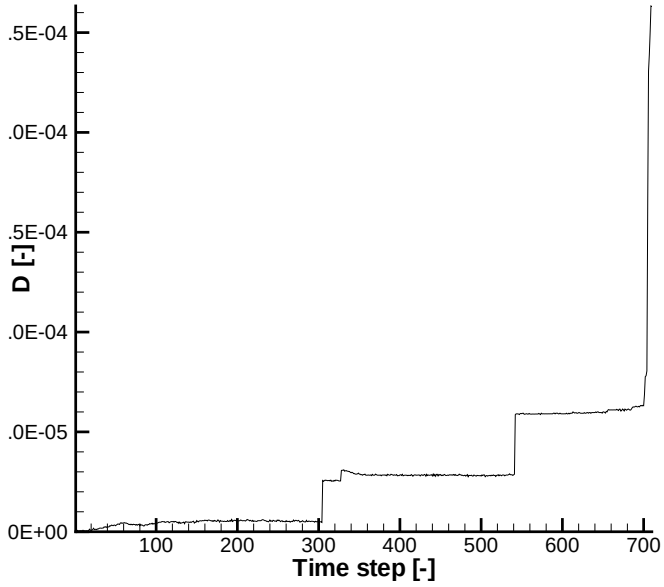

F 3.5: Average difference between SHAKE and FALCO particle positions, $\Delta t = 0.01$

Initial simulations were performed using the small time step $\Delta t = 0.01$. The simulations ran for 10000 time steps. Figure 3.4 shows the particle positions obtained with the FALCO particle corrector. Positions are displayed with $\delta t = 0.2$ sampling frequency, up to the time step 1200. Figure

3.5 shows the average difference between the bead positions obtained with both correctors defined as:

$$D = \frac{1}{3}\sum_{i=1}^{3}\left|\boldsymbol{r}^{i}_{SHAKE} - \boldsymbol{r}^{i}_{FALCO}\right| \tag{3.8}$$

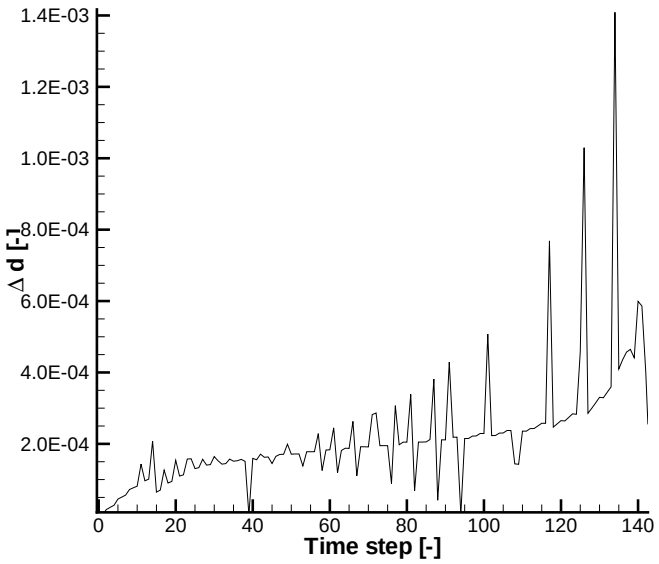

F 3.6: Average bond length deviation during SHAKE, $\Delta t = 0.05$

Here the data is shown prior to the first collision with the solid wall. After the collision, the particle starts to rotate and the average deviation increases. This can be expected since FALCO updates the directions in the correction process and SHAKE does not, hence the rotational motion would have a significant effect on the results. However prior to the wall collision and the fast spinning of the particle it initiates, the difference between the results obtained with the SHAKE and the FALCO correctors was negligible.

When the time step was increased to $\Delta t = 0.05$, the simulation using the SHAKE corrector diverged after 145 steps whereas the simulation using

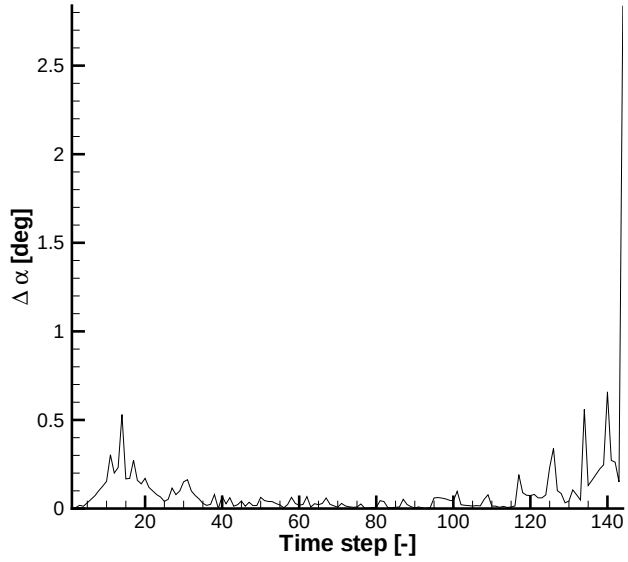

F 3.7: Average angular displacement during SHAKE, $\Delta t = 0.05$

the FALCO corrector completed successfully. The results clearly demonstrate that the time step magnitude has an impact on the stability of the SHAKE corrector.

A possible explanation which can be proposed is based on the fact that the SHAKE corrector utilises previous time step bond directions. As a result, it is sensitive to the angular displacement of the bonds. The combination of angular deflections and large deviations from the prescribed bond length leads to the divergence of the particle corrector.

The validity of this hypothesis can be demonstrated by analysing the evolution of the initial guess for the particle corrector. The quality of the initial guess can be quantified using the average deviation of the unconstrained bond length from the prescribed bond length

$$\Delta d = \frac{1}{2}\left(\left|a_{12}^{unc} - a_{12}\right| + \left|a_{23}^{unc} - a_{23}\right|\right) \tag{3.9}$$

and the average angular displacement given by

$$\Delta\alpha = \frac{1}{2}(\alpha_{12} + \alpha_{23}) \tag{3.10}$$

where α_{12} and α_{23} denote the angles between the bond orientation at time level t and $t + \Delta t$ for bonds 12 and 23 respectively.

Figures 3.6 and 3.7 show the evolution of Δd and $\Delta\alpha$ for the SHAKE corrector simulation with $\Delta t = 0.05$. As the simulation progresses, the initial guess gets worse for both measures. Both measures increase when the SHAKE simulation diverges with the average angular deviation equal to 2.83° and the average bond length deviation equal to 0.99%. However, whereas for the average angular deviation the divergence point corresponds to a maximum, the same is not true for the average bond length deviation.

Figures 3.8 and 3.9 show the evolution of Δd and $\Delta\alpha$ measures for the FALCO corrector simulation with $\Delta t = 0.05$. Figure 3.8 indicates that during the FALCO corrector run, Δd reaches the value of 1.22% which is higher than the value of Δd at SHAKE's divergence point. The periodically occurring peaks of the Δd measure clearly indicate the wall bounce events as the structure approaches the upper (moving) wall of the cavity. As the figure suggests, the studied structure completes 6 full circles during the 2000 time steps.

During the FALCO simulation, $\Delta\alpha$ reaches the value of 16.3° at time step 134, which overshoots the critical value concerning to SHAKE's divergence point.

The results indicate that it is possible to obtain a converged solution with the FALCO corrector even when the initial guess is much worse ($\Delta\alpha_{,FALCO} = 16.3°$) than that leading to the breakdown of SHAKE ($\Delta\alpha_{,SHAKE} = 2.83°$).

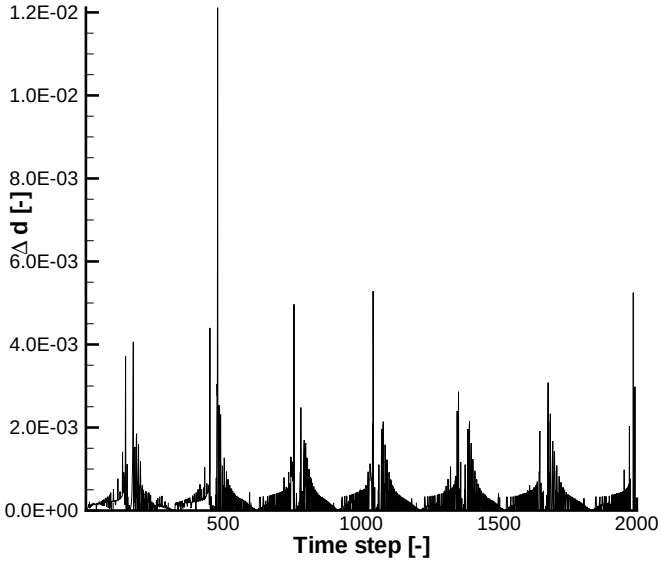

F 3.8: Average bond length deviation during FALCO, $\Delta t = 0.05$

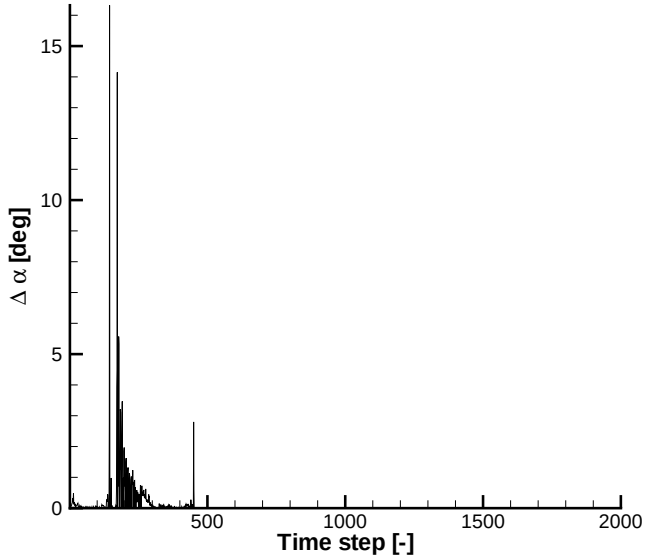

F 3.9: Average angular displacement during FALCO, $\Delta t = 0.05$

3.2 Verification of the Bead-Spring Model

Equation 2.80 and 2.81 describes dynamic behaviour of large molecules modeled as microscopic multi-spring mechanical systems with damping.

In order to verify the numerical model of such a multi-spring mechanical system, dynamic simulation of a simple mechanical model has been carried out. The investigated model consisted of two beads connected with a single spring. The performed numerical study considered the relaxation of this linearly elastic structure from the extended state.

The elastic dumbbell was considered to be symmetric, since the beads attached to the ends of the spring possessed the same mass and radius. Initially, the spring was extended from its resting length and the beads were held in place by anchors. The simulation started, when the anchors were released and the structure was allowed to relax in viscous fluid.

Numerical simulation of this dumbell relaxation study was compared against the analytical solution of the problem. The calculations were carried out considering both over-damped and critically damped harmonic systems, relevant to realistic DNA models. Mathematical model of the investigated one-dimensional harmonic spring problem is as follows:

$$m_n \frac{d^2 x_n}{dt^2} + m_n \gamma_n \frac{dx_n}{dt} + kx = 0 \tag{3.11}$$

with the concerning initial conditions: $x_1(t_0) = -L$, $x_2(t_0) = +L$, $v_1(t_0) = 0$ and $v_2(t_0) = 0$.

The studied harmonic system is considered to be over-damped [93] if $m_n\gamma_n^2 - 4k > 0$ and critically damped [93] if $m_n\gamma_n^2 - 4k = 0$. During the numerical studies, bead masses were set to $m_1 = m_2 = 7.196807 \times 10^{-3}$ kg and the damping factors were set to $m_1\gamma_1 = m_2\gamma_2 = 1.69668 \times 10^{-1}$ Ns/m.

Initial position of the beads was $x_1 = -1$ m, $x_2 = +1$ m. Two cases, over-damped and critically damped - with spring coefficients $k = (m_n\gamma_n^2)/4 = 0.5$ and 1.0 N/m - were investigated, respectively.

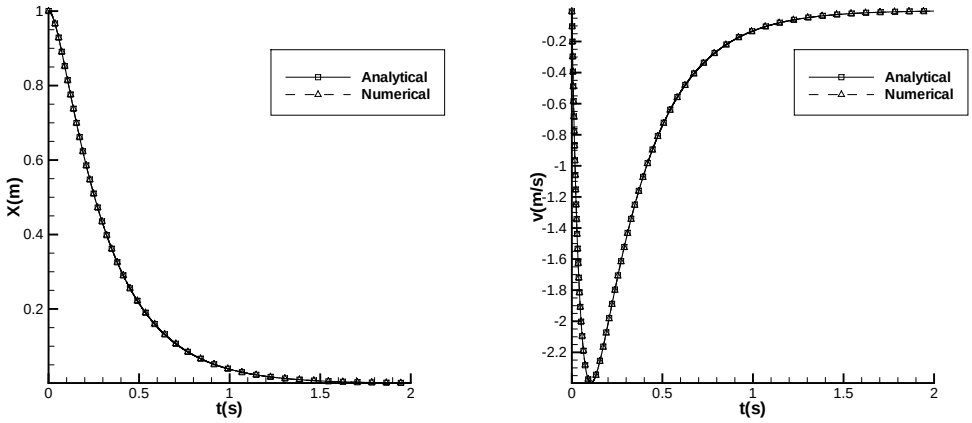

F 3.10: Position and velocity of bead "2" over time, k=0.5 N/m

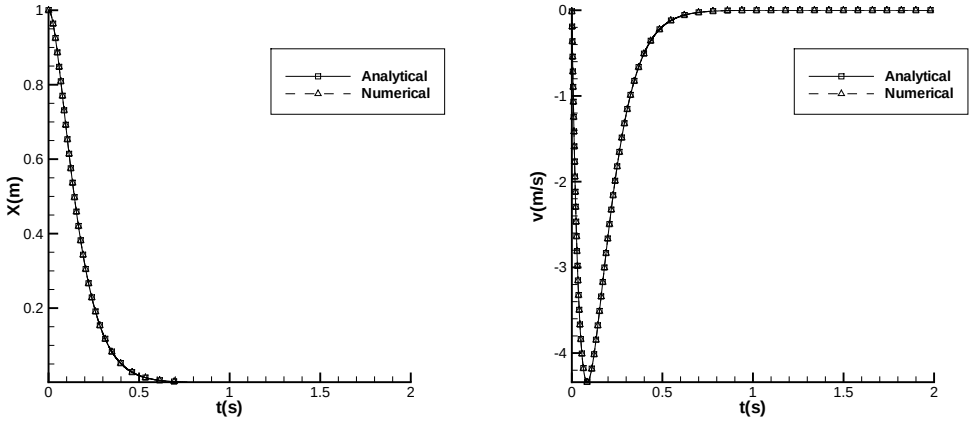

F 3.11: Position and velocity of bead "2" over time, k=1.0 N/m

First, the over-damped case with $k = 0.5$ N/m have been investigated. Figure 3.10 shows the position and velocity of bead "2", resulting from the analytical solution of 3.11 ([93]) and numerical calculations utilising 2.80

and 2.81. Figure 3.11 shows the same results for the critically damped case, with $k = 1.0$ N/m.

During the calculations, maximum relative deviation between the analytical and numerical solution for bead positions was 0.02% for $k = 0.5$ and 0.04% for the $k = 1.0$ case. Maximum relative velocity differences between the analytical and numerical solutions were 0.03% for $k = 0.5$ and 0.07% for the $k = 1.0$ case.

Simulation of DNA Mechanical Behaviour

4

Simulation of DNA Mechanical Behaviour

The considered meta-modelling approach was developed to describe the microscale behaviour of large molecules. The previous section provided detailed verification of the applied numerical techniques and algorithms. Based on the results of the verification studies, the implemented modelling tool has proven to be stable, efficient and reliable.

Having the numerics verified, validation of the modelling approach can be carried out. The goal of the validation studies is to demonstrate the ability of the modelling approach to capture and describe the relevant physical phenomenon with required accuracy. Validation of the modelling method has been carried out by comparing numerical simulation results against available experimental data.

This section presents the performed numerical studies to validate the modelling approach. The tests were targeted to describe both the macroscopic transport phenomenon and the related micromechanical behaviour of the considered molecule structures. During the performed studies, macromolecules have been represented as bead-rod and bead-spring structures, depending on the nature of the investigated problem.

4.1 Experimental Validation of the Bead-Rod Model

The numerical studies in the previous section provided extensive verification and detailed analysis of the applied particle corrector method. Based on these studies, the considered FALCO algorithm has proven to be an efficient and reliable method to preserve the structure of bead-rod micromechanical models. Having a verified particle corrector in hand, validation of the modelling approach has to be carried out.

This section is aimed to demonstrate that the meta-modelling approach is an accurate and reliable numerical tool to describe the transport of individual macromolecules. During this study, macromolecules represented as bead-rod structures have been considered. Numerical simulation results of the investigated transport phenomenon have been compared against available experimental data.

Focusing on the transport of macromolecules, Stein *et al.* [94] carried out detailed experimental studies. During their investigations, the transport of double-stranded DNA molecules in pressure-driven micro- and nanoflows has been observed using fluorescence microscopy.

The investigated λ-DNA molecules have been labelled with fluorescent dyes and individual molecules have been imaged by epifluorescence microscopy. Trajectories of the molecule's center-of-mass have been reconstructed by tracking the labeled DNA over a series of images. The experimental data was recorded with 5 Hz frequency, resulting data points in every 0.2 s [94]. Ensemble average velocity of a small number of molecules was calculated analysing the recorded images.

During the experiments, high aspect ratio rectangular microchannel had been used. Width of the channel was $w_c = 50\,\mu$m, channel height was $h_c = 0.25\,\mu$m and the length was $l_c = 4\,$mm. The flowing solution was aqueous

buffer, containing extremely low number of labeled DNA molecules.

In the channel, constant flow rate was maintained by applied pressure gradient, resulting steady Poisseuille flow. The applied $\nabla p = 1.44 \times 10^{-6}$ Pa/m pressure difference resulted parabolic profile with maximum of $u_{max} = 10.7\,\mu$m/s across the channel height. In the transverse direction, the flow was plug-like across the width, decreasing sharply within a distance of h_c at the near-wall region.

The flowing fluid was aqueous buffer with dynamic viscosity of $\eta = 1.05 \times 10^{-3}$ Pas and density of $\rho = 10^3$ kg/m^3 [94]. Kinematic viscosity of the solution was $\nu = 1.05 \times 10^{-6}$ m^2/s. Based on the maximum velocity u_{max} and the channel height h_c, the calculated Reynolds number was Re $= 2.54 \times 10^{-6}$.

The experiments have been carried out using 48.5 kbp λ-DNA molecules, with $L_c = 22\,\mu$m contour length. The observed DNA molecules resembled random coil configurations with the concerning equilibrium coil size $R_g = 0.73\,\mu$m [94]. The resulting Weissenberg number was below 5, which is the critical value for molecular elongation to start [94]. The applied steady Poisseuille flow did not impose stretching of the transported molecules [94]. Therefore, no entropic elastic behaviour of the dsDNA molecules was expected.

Considering the channel height of $h_c = 0.25\,\mu$m, the investigated DNA molecules have been strongly confined ($h_c < R_g$). Due to the intense confinement and the absence of strong velocity gradients, the conformational changes of the macromolecules were insignificant during the transport process [94].

In the numerical simulation, DNA molecules have been represented as bead-rod structures. Although the studied molecules were double-stranded DNA molecules, the applied flow conditions resulted in no stretching of

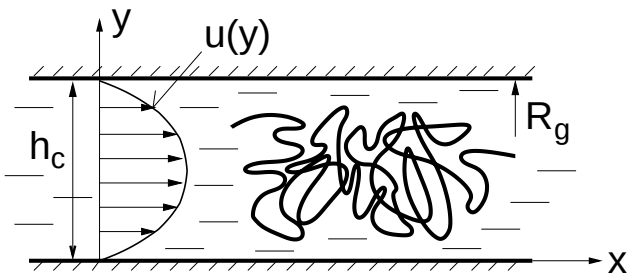

F 4.1: Sketch of the microchannel and the confined λ-DNA

the macromolecules [94]. Consistently, the elastic bead-spring model was irrelevant to the investigated problem.

Parameters of the considered bead-rod structure have been determined from real data. Rod lengths have been determined based on the persistence length λ_p of a stained DNA, resulting a segment length of $a = 2\lambda_p = 2 \times 67.15\,\text{nm} = 134.3\,\text{nm}$. This way, the considered macromolecule has been represented by 165 beads connected with 164 rods, respectively.

Bead radii have been determined considering the drag coefficient of a coiled molecule, calculated from the Einstein relation [50, 69]. This resulted equal bead radii of $b = 10.225\,\text{nm}$. Molecule mass of a 48.5 kbp λ-DNA is approximately $m_{DNA} = 5.81 \times 10^{-20}\,\text{kg}$ [42]. The molecular mass has been distributed equally along the beads, with a resulting bead mass of $m = 3.52 \times 10^{-22}\,\text{kg}$.

The numerical calculation has been carried out in a three-dimensional channel geometry. According to the experimental conditions [94], a parabolic velocity profile along the channel height was prescribed at the inlet. Along the channel width, the flow field was considered to be plug-like. At the outlet, the fluid was considered to enter into a constant-pressure reservoir. Here, constant pressure was prescribed as the boundary condition and fluid velocities were extrapolated from the computational domain.

Considering Stein ’s opinion regarding the preferred positions of macromolecules in pressure-driven flows [94], the DNA model has been initially placed to the half channel height at the inlet, resembling random coil conformation. Position and velocity of the structure was calculated in each step with $\Delta t = 2.33 \times 10^{-6}$ s real time step size.

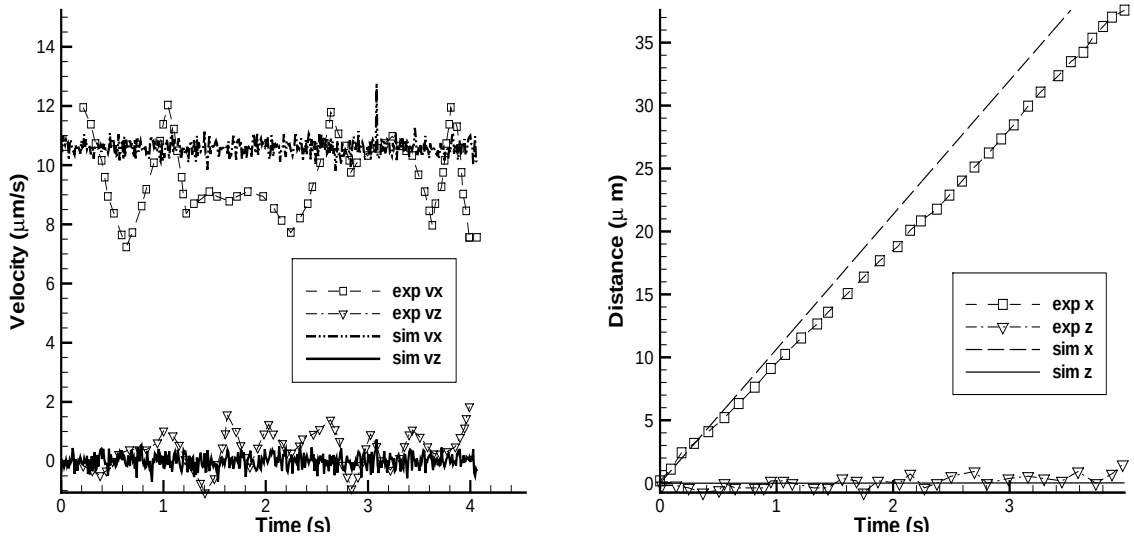

F 4.2: Experimental and calculated velocity and displacement

Figure 4.2 demonstrates the experimentally observed and the calculated velocity components and displacements of the molecule’s center-of-mass. The experimental data shows significant fluctuations in both x and z velocity components. Contrary to this behaviour, the fluctuations in the calculated velocity components are much weaker. A possible explanation of this effect may be the lack of correlation between the random Brownian forces acting on individual beads in the model.

Considering the streamwise (x) component of the center-of-mass velocity v_x, the numerical calculation slightly over-predicted the experimental mean value. In accordance, the simulated streamwise displacement consistently over-predicted the measured value. The calculated transverse (z)

velocity component v_z resembled the same zero mean value as the measured one, with weaker fluctuations compared to the measured data. The resulting transverse displacements are therefore slighter than the experimental values.

The transport phenomenon has been investigated in confined channels. According to Stein *et al.*'s work [94], majority of the molecules favours the middle region of the channel height. Consistently, the DNA model has been initially positioned to the middle of the channel. As the bead-rod model travelled towards the outlet, the structure stayed in the middle region of the channel height, in accordance to Stein *et al.* [94].

However, Stein *et al.* also argued that a small number of molecules may occur away from the channel mid-plane [94]. During the performed experiments, y position of the molecules along the channel height was not registered. It is possible, that some of the tracked molecules have randomly drifted away from the middle region of the channel, entering into a zone with relatively lower convective velocity. This is a possible explanation of the slight deviation between the calculated and experimentally observed streamwise velocity.

4.2 Experimental Validation of the Bead-Spring Model

Having the bead-spring mechanical model verified (see section 3), investigation of the relaxation dynamics of real DNA molecules has been carried out. The performed numerical calculations were aimed to validate the introduced model against experimental data resulting from single molecule experiments of Perkins *et al.* ([62]).

In their experiments, Perkins *et al.* studied the relaxation of single DNA molecules by optical microscopy. During the investigations, optically trapped DNA molecules were stretched to full extension by fluid flow. After stopping the fluid flow, the molecules were allowed to relax in the resting fluid.

Relaxation of the stained DNA molecules was recorded by video-enhanced fluorescence microscopy and the visible length of the molecules was measured for every frame. The experiments were carried out for long ($L_c = 39.1\,\mu m$), medium ($L_c = 21.1\,\mu m$) and short ($L_c = 7.7\,\mu m$) molecules.

During the DNA relaxation simulations, the molecules were modeled as bead-spring structures consisting 38, 21 and 8 beads representing long, medium and short DNA chains, respectively. The elastic elements were considered to consume 10 Kuhn steps and resembled nonlinear force-elongation behaviour described by the WLC-PET law 1.12.

The mass of the beads was determined by uniformly distributing the concerning molecular mass over the beads of the structure. Bead radii were calculated from the Batchelor formula ([95]). Therefore, mass of a single bead was $m_{(1)} = 3.61 \times 10^{21}$ kg in the large, $m_{(2)} = 3.52 \times 10^{21}$ kg in the medium and $m_{(3)} = 3.37 \times 10^{21}$ kg in the short DNA chain model. Bead radii were $b_{(1)} = 3.47 \times 10^{-8}$ m, $b_{(2)} = 3.61 \times 10^{-8}$ m and $b_{(3)} = 3.88 \times 10^{-8}$

m for the different chain models, respectively.

During the numerical calculations, equation 2.80 and 2.81 was utilised to describe the dynamic behaviour of the models. Figure 4.3 and 4.4 shows the upper and lower bound of the experimental results reported by Perkins *et al.* [62] for the long ($L_c = 39.1\,\mu m$) and medium ($L_c = 21.1\,\mu m$) DNA chains, along with the simulated relaxation curve.

Figure 4.5 demonstrates the same data, relevant to the short ($L_c = 7.7\,\mu m$) molecules. The figures demonstrate good agreement of the simulated relaxation curves with the experimental data.

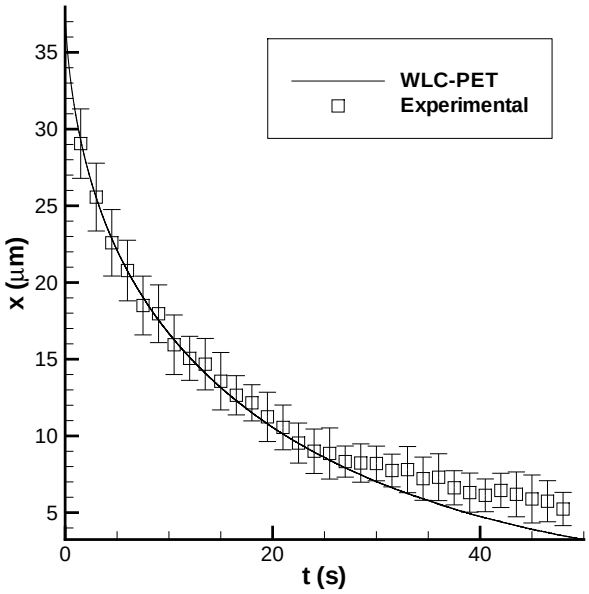

F 4.3: Relaxation of DNA molecule with contour length of 39.1 μm

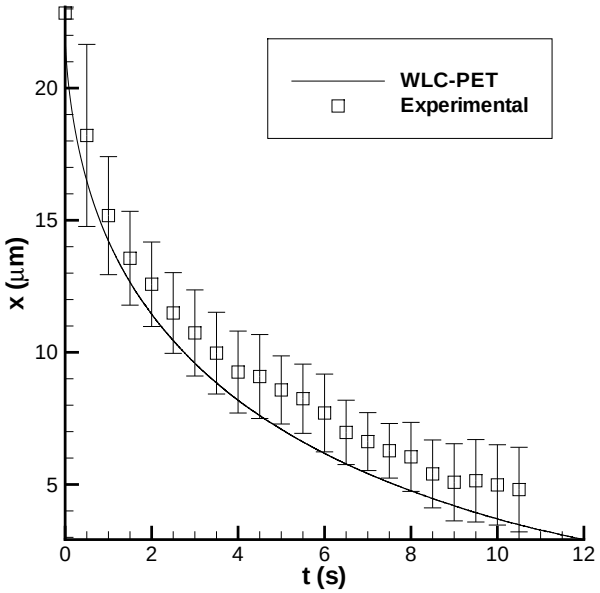

F 4.4: Relaxation of DNA molecule with contour length of 21.1 μm

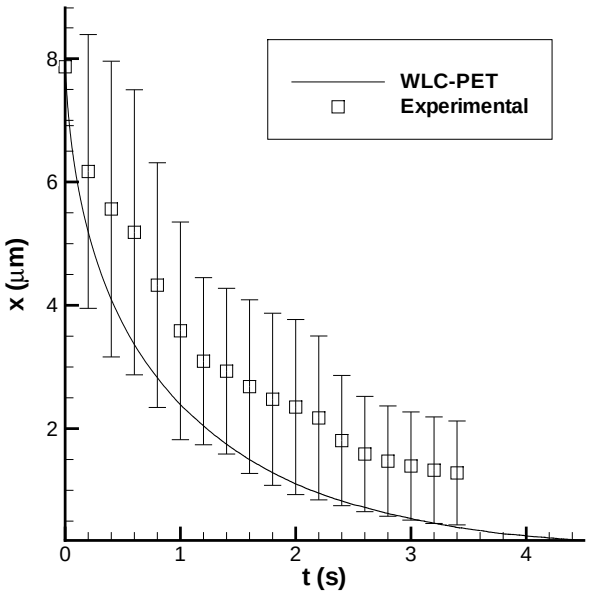

F 4.5: Relaxation of DNA molecule with contour length of 7.7 μm

4.3 Relaxation and Stretching of dsDNA Molecules

This section is devoted to the investigation of the micromechanical behaviour and motion of dsDNA molecules in fluid flow. Results of the performed numerical simulations have been compared against relevant experimental data.

Based on the comparison of calculated and experimentally measured behaviour of the molecules, a novel correction to the elastic force acting on dsDNA segments has been suggested. The corrected elastic force offers significant improvement in the prediction of dsDNA length in comparison with published models.

The simulation results indicate that the dynamic elastic properties of dsDNA may differ from those determined from static measurements. The analysis of contributions to the overall force acting on the dsDNA molecules demonstrates that the experimentally observed dynamics of dsDNA extension was dominated by the hydrodynamic drag force.

The simulations reported in this section follow the experimental results obtained by Wong *et al.* [96], who conducted studies of dsDNA relaxation in no-flow conditions and dsDNA stretching using hydrodynamic focusing. In their experiments, 164 kbp T2 DNA stained with YOYO-1 dye were used, and the highest reported Deborah number was equal to 0.8. The staining changed the contour length of the dsDNA molecules from $\sim 56\,\mu$m to $\sim 71\,\mu$m and the persistence length from 53.4 nm to 67.15 nm ([97]).

Following the coarse-graining considerations of Larson ([73]), a single spring of our DNA model represented 10 Kuhn steps of the molecule. Therefore, bead-spring models containing 54 beads and 53 springs were used to describe the T2 DNA molecules. The total mass was uniformly

distributed along the beads, resulting in bead mass of $m = 3.6384 \cdot 10^{-21}$ kg. Drag coefficient of the molecule was approximated by Batchelor's formula ([95]), which resulted the hydrodynamic bead radius of $b_n = 3.37 \cdot 10^{-8}$ m.

The results of the performed initial simulations suggested that both the standard WLC and WLC-PET forces lead to over-prediction of elastic forces in the high stretch regime and under-prediction of forces in the low stretch regime of the DNA relaxation process. Hence an adjusted version WLC-PET was proposed to counterbalance these effects as follows

$$F^{WLC-PETA} = 8 \cdot \left(0.5 - \frac{(0.5\hat{x})}{(0.5 + 0.5\hat{x})}\right) \cdot F^{WLC-PET} \tag{4.1}$$

The suggested correction for the DNA relaxation and stretching is evaluated for a single experimental setup reported by Wong *et al.* [96].

4.3.1 Relaxation of dsDNA in Free Solution

In Wong *et al.*'s experiment, the T2 DNA molecules were initially stretched by the stream-wise velocity gradient generated by hydrodynamic focusing. After the flow was stopped, the DNA molecules were allowed to relax freely in the resting buffer solution with viscosity of $\eta = 21.5$ cP.

It is important to note at this stage that experimental conditions in this relaxation study differed from previous experiments (e.g. [62]), where molecules were attached to fixed latex microspheres by one end resulting in constrained dynamics of the relaxation process.

The initial condition for the relaxation simulations corresponded to a resting state with end-to-end distance of $x/L = 0.8$, digitised from the experimental data. The chain was then allowed to relax freely in resting buffer solution.

The relaxation process started with a short, sub-continuum scale

($\sim 10^{-12}$ s) transient phase. This period was dominated by elastic forces, since drag forces acting on the initially resting beads were negligible. In this transient phase, bead velocities increased rapidly resulting in sufficient drag to balance the action of spring forces.

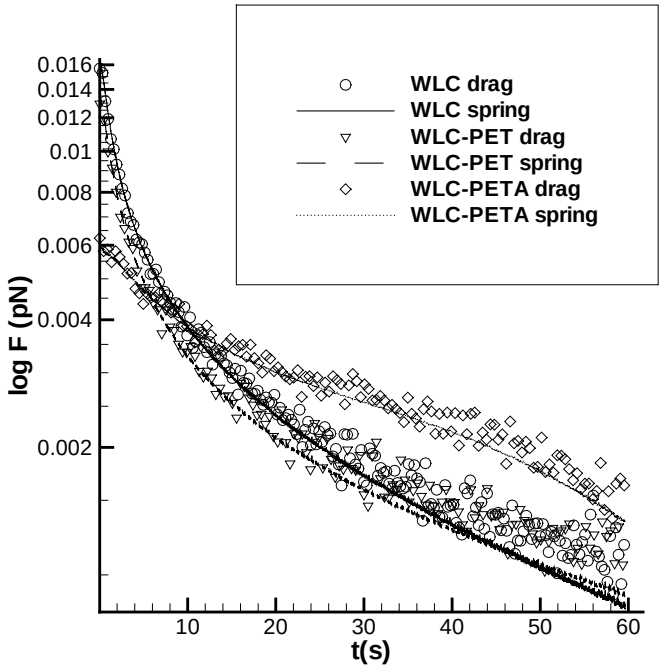

F 4.6: Average drag and spring forces during relaxation

As bead velocities reached their peak, the transient phase finished and the relaxation process advanced into the quasi-balanced phase. At subsequent stages, dynamics of the relaxation process was governed by mainly drag and elastic forces, with slight perturbations due to Brownian effects.

Figure 4.6 illustrates average spring and drag forces calculated in the quasi-balanced phase of the simulations. The averages were taken in the ensemble represented by all beads and springs in all dsDNA molecules. The computed ratio of the magnitude of the Brownian force φ to the drag force in these simulations was $O\left(10^{-1}\right)$.

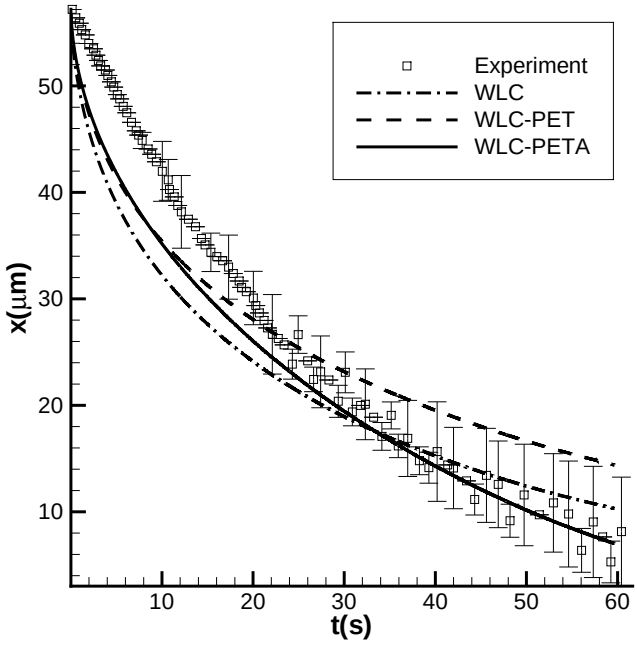

F 4.7: dsDNA length during relaxation

Both WLC and WLC-PET models lead to a significant decrease of the average elastic force with time. After an initial period of ~ 30 s, the magnitude of the drag force exceeded the magnitude of the spring force, resulting in acceleration of the beads. This process cannot be considered to be quasi-static. By comparison, the adjusted WLC-PETA elastic force lead to a lower spring force and similar drag force for the entire duration of the relaxation process.

The comparison between computational results and experimental data of [96] for the dsDNA molecules length is presented in Figure 4.7. Here, the error bars on the experimental data represent the variation between different dsDNA molecules. The proposed elastic force yields better agreement with the experimental data, particularly at the late stages of the relaxation process.

Further, the dsDNA relaxation time was computed following [62] by fitting the square of the calculated end-to-end distance x^2 to

$$f(t) = Aexp(-t/\tau_1) + B, \tag{4.2}$$

taking into account only the data points corresponding to $x/L < 0.3$. The relaxation time obtained with the WLC-PETA force was equal to 14.84 s, which provided the closest fit to the experimental relaxation time of 15.0 s. Simulations utilising WLC and WLC-PET yielded relaxation times of 23.98 s and 31.67 s, respectively.

A possible explanation of the obtained results can be provided if one recalls that the experiments by Smith *et al.* [58, 59] were performed under static conditions. These measurements resulted in the data for the derived fits of the elastic force given by equations 1.10 and 1.12.

The observed difference between the simulated and experimental relaxation curves for the dynamic process and improvement obtained with the modified elastic force may suggest that elastic forces resulting from static measurements do not provide an adequate description of the dynamic phenomena.

In order to verify this hypothesis, the computations of the DNA stretching in a highly non-uniform flow field were conducted. Unmodified WLC elastic forces are excluded from further discussion as the results obtained with this force for the dsDNA relaxation process demonstrate least favourable comparison with the experiment.

4.3.2 Extension of dsDNA via Hydrodynamic Focusing

In the experimental dsDNA extension study by Wong *et al.* [96], a dsDNA-laden stream was constrained and stretched by two focusing streams in a

converging channel (Figure 4.8).

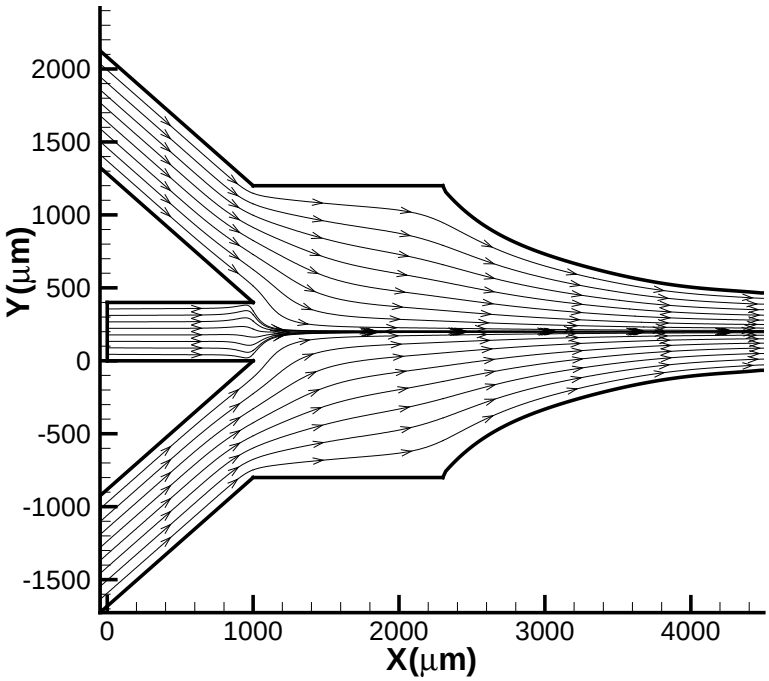

F 4.8: Fluid streamlines in the focusing device

As the DNA stream reached the focusing section, the upper and lower sheath flows merged into it, forcing the transported DNAs into a narrow region at the centreline. In this region, the molecules were exposed to a strong streamwise velocity gradient. The strain rate was controlled by adjusting the flow rates of the focusing side streams.

The viscosity of the fluid was equal to 1.14 cP, the flow rate of the DNA solution was equal to $0.5\,\mu\mathrm{l\,min^{-1}}$ and the corresponding Deborah number was ~ 0.8. The case presented in this section corresponds to the strain rate $\varepsilon = 1.006\,\mathrm{s^{-1}}$, which resulted from the sheath flow rate of $21.8\,\mu\mathrm{l\,min^{-1}}$ in the focusing streams.

Initially the fully developed 2-D flow field was computed, the streamlines of the developed fluid flow in the focusing device are illustrated on figure 4.8.

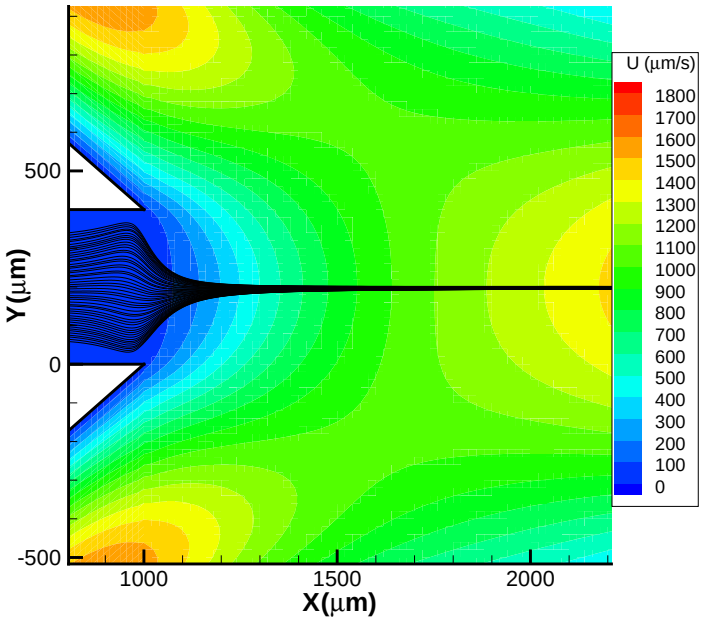

F 4.9: Velocity contours and dsDNA pathlines

The baseline grid in these simulations comprised 20x50 cells in the main inlet, 40x70 cells in the sheath inlets and 100x170 cells in the main channel. The grid convergence was ascertained by doubling the number of grid cells which lead to the average relative velocity difference of 0.78% and 0.58% in the first and second refining stage, respectively. The relative velocity differences were calculated along the centreline of the extension region spanning between $x = 1000\,\mu$m and $x = 1500\,\mu$m.

Once the developed flow has been obtained, dsDNA simulations were conducted using both standard and adjusted WLC-PET models for 50 ds-DNAs released at $t = 0$ in the upstream section of the middle inlet.

The release points were uniformly distributed across the channel width. Figure 4.9 shows the focusing section with contours of the x-velocity component and computed pathlines of the centres of mass of 50 individual

dsDNA molecule models. The dsDNA molecules essentially follow fluid streamlines, which is in good qualitative agreement with photographs of the dsDNA concentration reported by Wong *et al.* [96].

dsDNA elastic forces obtained with WLC-PET and WLC-PETA models have been compared with the experimental data in Figure 4.10. Similarly to the approach taken in the experimental study, the simulation results were averaged for dsDNA molecules located close to the centreline of the focusing channel in the region of minimal shear stress. The error bar on the experimental data represents the variation between individual molecules.

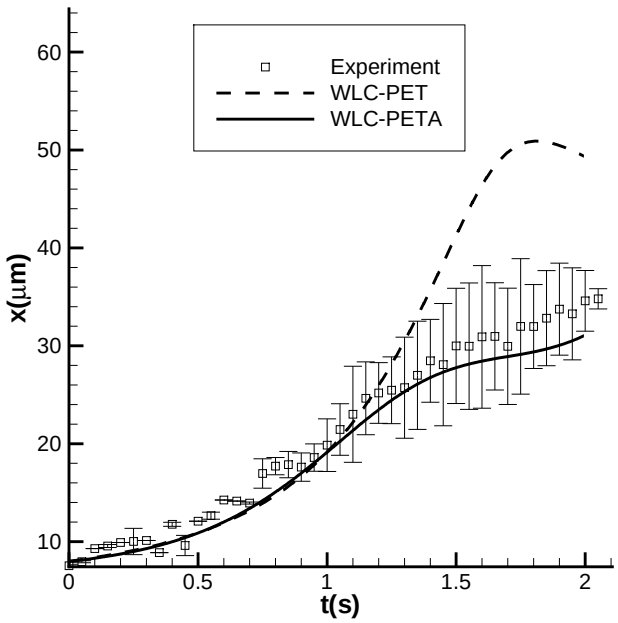

F 4.10: dsDNA length during extension

Good agreement is obtained with both elastic forces at the early stages of the stretching process ($t < 1.15\,\mathrm{s}$). At this stage the elongation is relatively small ($x < 25\,\mu\mathrm{m}$) and the molecules undergo affine deformation with the extension following the fluid stretch.

At later times ($t > 1.15$ s) of the process, the standard WLC-PET model deviated significantly from the experimental results. Similar tendency was previously reported by [71, 98] and [99] for Brownian Dynamics simulations performed in extensional flows at low Deborah number (De = 2.0). By comparison, the proposed WLC-PETA model demonstrated good agreement with the experimental data at the later stages of the dsDNA stretching process as well. For the overall process, the average relative difference between the experimental mean values and the calculated DNA stretch was 0.074%.

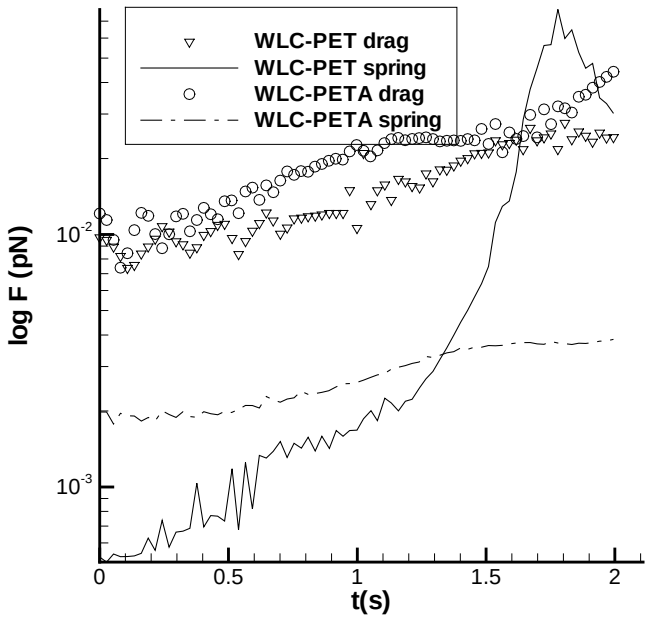

F 4.11: Average drag and spring forces during extension

Figure 4.11 illustrates average drag and elastic forces acting on beads of the dsDNA model in the hydrodynamic extension process. At the early stage ($t < 1.15$ s), the two models predicted almost identical molecule end-to-end distances, however the WLC-PET model lead to lower average

elastic forces. This is in agreement with the behaviour observed at late times of the relaxation process.

In comparison with the modified WLC-PETA, the original WLC-PET model lead to systematically lower values of drag, however the difference between the drag forces is relatively small. The overshoot of the experimental data obtained with WLC-PET is thus due to faster dsDNA stretching arising from lower elastic forces. It is also worth noting that the results suggest that the dsDNA extension process is dominated by the drag force for the whole duration of the simulation.

The developed meta-model has proven to be a valuable tool for the investigation of dsDNA dynamics in the fluid flow. The results obtained with conventional elastic force models demonstrate reasonable comparison with the experiment.

However, the proposed modification for the elastic force offers significant improvement for both dsDNA relaxation process under no-flow conditions and dsDNA extension in a complex flow field. Investigation of the relative impact of forces acting on dsDNA molecules led to the suggestion that the hydrodynamic drag force dominates the dsDNA extension process in the hydrodynamic focusing experiments of Wong *et al.* [96].

Conclusions and Future Work

5
Conclusions

The work completed in this thesis considered the numerical modelling of microscale processes. Motivated by a joint research cooperation funded by the European Commission, a novel modelling approach has been developed. The developed modelling tool was designed to provide an accurate description of the macroscopic transport and the micromechanical behaviour of large molecules, such as DNA.

In the frame of this Ph.D. work, systematic verification of the applied numerical methods and thorough validation of the modelling approach have been carried out. During cooperative research with the project partners, the developed novel modelling tool has been successfully utilised to simulate DNA transport and mechanical behaviour in microchannels.

5.1 Conclusions of the Research

A novel modelling approach was formulated to provide an accurate description of phenomenon occurring on microscopic length and time scales. The developed meta-modelling method successfully merges the continuum-based model of the solvent and the more sophisticated, micromechanical structure-based description of the transported macromolecules. The introduced modelling technique is especially advantageous, when molecules of interest are several orders of magnitude larger than the solvent ones and the solution is dilute.

The approach can be related to the Brownian Dynamics method, since both utilise the Langevin equation to describe fine scale phenomenon. However, the proposed meta-modelling method features significant differences compared to the Brownian Dynamics technique. While numerical implementation of the BD method neglects inertia terms of the Langevin equation, the meta-model calculations account for these inertia effects. Due to the implicit solvent concept of the Brownian Dynamics method, the concerning fluid fluid phase is not modeled. Contrary to this strategy, continuum-level description of the solvent is provided by the meta-modelling technique. Simplifications of the BD method limits its applicability, especially when complex and unsteady flow fields are considered.

Macromolecules exhibiting no elastic behaviour under the given conditions can be represented with bead-rod structure models. The behaviour of such bead-rod micromechanical structures can be described utilising a two-step, predictor-corrector type solution algorithm. Considering the typical time steps involved in meta-model simulations, the SHAKE method

developed for Molecular Dynamics calculations has proven to be inefficient. The limitations on time step size arising from the limited convergence range of SHAKE initiated the formulation of a new particle corrector method. Based on the results of the performed numerical tests, the FALCO particle corrector developed in this Ph.D. work has proven to be a reliable and robust algorithm. Comparison of SHAKE and FALCO clearly demonstrated that FALCO resulted converged solution, even when the initial guess for the particle positions was much worse than the critical, which led to the breakdown of SHAKE.

Evaluation of the bead-rod model against experimental data revealed that calculated streamwise velocity of the center-of-mass slightly overpredicted the experimentally measured value. This deviation however, might have been resulted from DNA molecules randomly drifting away from the high convective velocity region in the middle of the channel, during the experiments. Also, the calculated random Brownian noise was weaker than the experimentally observed values in both streamwise and cross-stream directions.

Micromechanical behaviour of large molecules resembling entropic elasticity can be described by the bead-spring structure model. Utilising the PET transformation provided by Underhill and Doyle [72] and considering the coarse-graining guidelines of Larson [73], bead-spring mechanical structures resembling consistent force-elongation behaviour can be constructed. Systematically derived models provide accurate description of the experimentally observed elastic behaviour, provided that entropic forces have been measured under the same conditions as the considered experiment. However, in cases when conditions of the investigated problem differ significantly from the conditions of the force-elongation experiments, suitable adjustment of the measured spring forces is necessary.

Such situations have been extensively investigated when relaxation of an extended dsDNA in free solution and extension of DNA molecules via hydrodynamic focusing has been considered. During these studies, unconstrained free dynamics of the considered dsDNA molecules has been investigated numerically. Relaxation simulations based on force-extension laws resulting from static experiments predicted faster contraction of the molecule for large extensions and slower relaxation dynamics for small extensions. The proposed correction of the elastic forces resulted significant improvement in the determination of dsDNA length in comparison with published models. Detailed analysis of the forces demonstrated that the first half of the relaxation process was governed by the quasi-balance of elastic and hydrodynamic drag forces, while the second half of the process was characterised by the slight dominance of the drag forces.

The performed hydrodynamic extension studies resulted similar findings in regard to the calculated dsDNA lengths. In the early stages of the process, the molecular extension followed the fluid stretch, therefore good agreement with the experimental results was obtained for both the standard and the adjusted force models. At the later stages of the extension process, molecule extension calculated by the standard force model deviated significantly from the experimental values, while the adjusted force model demonstrated excellent agreement with the measured data. Investigation of the forces demonstrated the dominance of hydrodynamic drag forces during the majority of the extension process. Considering both the relaxation and extension studies, the proposed adjustment of the elastic force resulted significant improvement in the calculation of dsDNA lengths.

5.2 Future Work

The presented mesoscale modelling approach carries significant potential to become the major simulation tool for mesoscale phenomenon. Further development of the method will enable the description of multi-physics mesoscale processes relevant to individual macromolecules.

The modelling tool has been successfully applied to demonstrate the capabilities to model polymer migration phenomenon, considering Saffman lift force and Faxen drag correction. However, validation of the migration model was impossible, due to the lack of available experimental data.

The numerical approach provides the ability to consider the action of additional forces on the beads of the relevant micromechanical models. Depending on the investigated physical phenomenon, the effect of electrostatic forces, magnetic forces and other external fields on the tracked macromolecule structures can be modeled.

As a further development possibility, mesoscale modelling of biochemical reactions, such as DNA hybridisation and protein binding reactions can also be investigated.

List of Publications

1. M. Benke, D. Drikakis, E. Shapiro: New simulation tool for bio-nanofluidics, Cranfield Multi-Strand Conference, 6-7 May 2009

2. M. Benke, E. Shapiro, D. Drikakis: FALCO - Fast Linear Corrector for Modelling DNA-laden flows, 6th International Conference on Nanochannels, Microchannels and Minichannels, 23-25 June 2008, Darmstadt, Germany

3. N. Asproulis, M. Benke, M. Lai, E. Shapiro, D. Drikakis, D. Brown, M. Dawson, G. Pollard, P. Ioannou, V. Poulopoulos: Modelling approaches for micro- and nanoscale diffusion phenomena, International Conference on Process Intensification and Nanotechnology, 15-18 Sept 2008, Albany, New York, USA

4. M. Benke, E. Shapiro, D. Drikakis: An efficient multi-scale modelling approach for ssDNA motion in fluid flow, Journal of Bionic Engineering 5, 2008

5. M. Benke, E. Shapiro, D. Drikakis: Modelling the polymer migration phenomena in DNA-laden flows, 2nd Micro and Nano Flows Conference, 1-2 September 2009

6. M. Benke, E. Shapiro, D. Drikakis: Mechanical behaviour of DNA

molecules - elasticity and migration, Submitted to: Medical Engineering & Physics

7. M. Benke, E. Shapiro, D. Drikakis: Description of a novel mesoscopic simulation technique, In progress, targeted journal: Journal of Computational Physics

8. M. Benke, E. Shapiro, D. Drikakis: Dynamic modeling of dsDNA molecules in fluid flow, Submitted to: Journal of Fluid Mechanics

9. D. Drikakis, N. Asproulis, E. Shapiro, M. Benke: Computational Strategies for Micro- and Nanofluid Dynamics, book chapter in Microfluidic Devices in Nanotechnology: Fundamental Concepts, 2010, John Wiley & Sons, In press

References

[1] D. Drikakis and M. Kalweit. *First Handbook in Theoretical and Computational Nanotechnology*, chap. Chapter 11: Computational Modelling of Flow and Mass Transport Processes in Nanotechnology (American Scientific Publishers, 2006).

[2] D. Drikakis and W. Rider. *High-Resolution Methods for Incompressible and Low-Speed Flows* (Springer, 2004).

[3] W. Ehrfeld, V. Hessel, and H. Lowe. *Microreactors: New Technology for Modern Chemistry* (Wiley-VHC: Weiheim, 2000).

[4] N. Nguyen and Z. Wu. *Micromixers - a review*. J. Micromech. Microeng. **15**, R1 (2005).

[5] A. D. Stroock, S. K. W. Dertinger, A. Ajdari, I. Mezic, H. A. Stone, and G. M. Whitesides. *Chaotic mixer for microchannels*. Science **295**, 647 (2002).

[6] R. Bashir. *Biomems: state-of-the-art in detection, opportunities and prospects*. Advanced Drog Delivery Reviews **56(11)**, 1565 (2004).

[7] Y. Zhang, R. W. Barber, and D. R. Emerson. *Part separation in microfluidic devices - splitt fractionation and microfluidics*. Current Analytical Chemistry **1**, 345 (2005).

[8] G. Whitesides. *The origins and the future of microfluidics*. Nature **442**, 368 (2006).

[9] T. M. Squires and S. R. Quake. *Microfluidics: Fluid physics at the nanoliter scale*. Reviews of Modern Physics **77**(3), 977 (2005).

[10] H. Stone, A. Stroock, and A. Ajdari. *Engineering flows in small devices: Microfluidics toward a lab-on-a-chip*. Ann. Rev. Fluid Mech. **36**, 381 (2004).

[11] P.-A. Auroux, D. Iossifidis, D. R. Reyes, and A. Manz. *Micro total analysis systems 1 introduction, theory and technology*. Analytical Chemistry **74**, 2623 (2002).

[12] P.-A. Auroux, D. Iossifidis, D. R. Reyes, and A. Manz. *Micro total analysis systems 2 analytical standard operations and applications*. Analytical Chemistry **74**, 2637 (2002).

[13] G. M. Mala, D. Li, and J. D. Dale. *Heat transfer and fluid flow in microchannels*. International Journal of Heat and Mass Transfer **40**, 3079 (1997).

[14] D. Mayness and B. W. Webb. *Fully-developed thermal transport in combined pressure and electro-osmotically driven flow in microchannels*. Journal of Heat Transfer **125**, 889 (2003).

[15] J. Koo. *Computational nanofluid flow and heat transfer analyses applied to micro-systems*. Ph.D. thesis, North Carolina State University (2005).

[16] J. Gargiuli, E. Shapiro, H. Gulhane, G. Nair, D. Drikakis, and P. Vadgama. *Microfluidic systems for* in situ *formation of nylon 6,6 membranes*. J. Mem. Sci. **282**, 257 (2006).

[17] P.-C. Wang, J. Gao, and C. S. Lee. *High-resolution chiral separation using microfluidics-based membrane chromatograph*. Journal of Chromatography A **942**, 115 (2002).

[18] Y. N. Shi, P. C. Simpson, J. R. Scherer, D. Wexler, C. Skibola, M. T. Smith, and R. A. Mathies. *Radial capillary array electrophoresis microplate and scanner for high-performance nucleic acid analysis*. Analytical Chemistry **71**, 5354 (1999).

[19] J. W. Simpson, M. C. Ruiz-Martinez, G. T. Mulhern, J. Berka, J. R. Latimer, J. A. Ball, R. J. M., and G. T. Went. *A transmission imaging spectrograph and microfabricated channel system for dna analysis*. Electrophoresis **21**, 135 (2000).

[20] S. A. Pasas, N. A. Lacher, D. M. I., and S. M. Lunte. *Detection of homocysteine by conventional and microchip capillary electrophoresis/electrochemistry*. Electrophoresis **23**, 759 (2002).

[21] J. C. Fanguy and C. S. Henry. *The analysis of uric acid in urine using microchip capillary electrophoresis with electrochemical detection*. Electrophoresis **23**, 767 (2002).

[22] S. W. J.M. Ottino. *Introduction: mixing in microfluidics*. Phil. Trans. R. Soc. Lond. A **362**, 923 (2004).

[23] *Biological detection system technologies - technology and industrial base study*. Tech. rep., TRW Systems and Information Technology Group (2001).

[24] T. Cass and C. Toumazou. *State-of-science review: Biosensors and biomarkers*. Tech. rep., Imperial College, London (2006).

[25] C. M. Ho. *Micro-electro-mechanical-systems (mems) and fluid flow*. Annual Review of Fluid Mechanics **30**, 579 (1998).

[26] G. Karniadakis, A. Beskok, and N. Aluru. *Microflows and Nanoflows: Fundamentals and Simulation* (Springer, New York, 2005).

[27] C. M. Megaridis, A. Guvenc, J. A. Libera, and Y. Gogotsi. *Attoliter fluid experiments in individual closed-end carbon nanotubes: Liquid film and fluid interface dynamics*. Physics of Fluids **14(2)**, L5 (2002).

[28] C. L. M. H. Navier. *MÂ´emoire sur les lois du mouvement des fluides*. MÂ´e moires de lÂ´AcadÂ´emie Royale des Sciences de lÂ´Institut de France **6**, 389 (1823).

[29] N. V. Churaev, V. D. Sobolev, and A. N. Somov. *Slippage of liquids over lyophobic solid surfaces*. Journal of Colloid and Interface Science **97**, 574 (1984).

[30] D. C. Tretheway and C. D. Meinhart. *Apparent fluid slip at hydrophobic microchannel walls*. Physics of Fluids **14**, L9 (2006).

[31] C.-H. Choi, K. J. A. Westin, and K. S. Breuer. *Apparent slip flows in hydrophilic and hydrophobic microchannels*. Physics of Fluids **15**, 2897 (2003).

[32] E. Ruckenstein and P. Rajora. *On the no-slip boundary condition of hydrodynamics*. Journal of Colloid and Interface Science **96**, 488 (1983).

[33] P. G. de Gennes. *On fluid/wall slippage*. Langmuir **18**, 3413 (2002).

[34] E. Lagua and H. A. Stone. *Effective slip in pressure-driven stokes flow*. Journal of Fluid Mechanics **489**, 55 (2003).

[35] D. C. Tretheway and C. D. Meinhart. *A generating mechanism for apparent fluid slip in hydrophobic microchannels*. Physics of Fluids **16**, 1509 (2004).

[36] J. I. Molho, A. E. Herr, T. W. Kenny, M. G. Mungal, M. G. Garguilo, P. H. Paul, M. Deshpande, J. R. Gilbert, P. M. StJohn, T. M. Woudenberg, and C. Connell. *Fluid transport. mechanisms in microfluidic devices*. In *MEMS ASME DSC 66* (1998).

[37] J. Hahm. *Numerical simulation of electrokinetically driven flows*. Ph.D. thesis, Texas A&M University (2005).

[38] X. Xuan and D. Li. *Electroosmotic flow in microchannels with arbitrary geometry and arbitrary distribution of wall charge*. Journal of Colloid and Interface Science **289**, 291 (2005).

[39] M. R. Brown and C. D. Meinhart. *Ac electroosmotic flow in a dna concentrator*. Microfluidics and Nanofluidics **2**, 513 (2006).

[40] F. Baldessari and J. G. Santiago. *Electrophoresis in nanochannels: brief review and speculation*. Journal of Nanobiotechnology **4**, doi:10.1186/1477 (2006).

[41] Y.-C. Chung, Y.-C. Lin, Y.-L. Hsu, W.-N. T. Chang, and M.-Z. Shiu. *The effect of velocity and extensional strain rate on enhancing dna hybridization*. J. Micromech. Microeng. **14**, 1376 (2004.).

[42] G. Lukacs, P.Haggie, O. Seksek, D. Lechardeur, N. Freedman, and A. Verkman. *Size-dependent dna mobility in cytoplasm and nucleus*. J. Biol. Chem. **275**(3), 1625 (2000).

[43] M. G. el Hak. *Liquids: The holy grail of microfluidic modeling*. Phys. Fluids **17**, 100612 (2005).

[44] P. S. Doyle and P. T. Underhill. *Handbook of Materials Modeling, Brownian Dynamics Simulations of Polymers and Soft Matter* (Springer, 2005).

[45] D. Trebotich, G. H. Miller, P. Colella, D. T. Graves, D. F. Martin, and P. O. Schwartz. *A tightly coupled particle-fluid model for dna-laden flows in complex microscale geometries*. In *Computational Fluid and Solid Mechanics 2005*, pp. 1018–1022 (2005).

[46] G. S. Ayton and G. A. Voth. *Simulation of biomolecular systems at multiple length and time scale*. International Journal for Multiscale Computational Engineering **2(2)**, 291 (2004).

[47] G. S. Ayton, W. G. Noid, and G. A. Voth. *Multiscale model of biomolecular systems: in serial and parallel*. Current Opinion in Structural Biology **17**, 192 (2007).

[48] G. M. Wang and W. C. Sandberg. *Non-equilibrium all-atom molecular dynamics simulations of free and tethered dna molecules in nanochannel shear flows*. Nanotechnology **18**(13) (2007).

[49] W. Wang, K. A. Kistler, K. Sadeghipour, and G. Baran. *Molecular dynamics simulation of afm studies of a single polymer chain*. Physics Letters A **372**, 7007 (2008).

[50] M. Doi and S. Edwards. *The theory of polymer dynamics* (Oxford: Clarendon, 1986).

[51] P. S. Doyle and S.-G. Shaqfeh, E. *Dynamic simulation of freely-draining, flexible bead-rod chains: Start-up of extensional and shear flow*. Journal of Non-Newtonian Fluid Mechanics **76**, 43 (1998).

[52] P. S. Doyle, E. S. G. Shaqfeh, G. H. McKinley, and S. H. Spiegelberg. *Relaxation of dilute polymer solutions following extensional flow*. Journal of Non-Newtonian Fluid Mechanics **76**, 79 (1998).

[53] J. Hur, E. Shaqfeh, and R. Larson. *Brownian dynamics simulations of single dna molecules in shear flow*. Journal of Rheology **44**(4), 713 (2000).

[54] R. M. Jendrejack, D. C. Schwartz, J. J. de Pablo, and M. Graham. *Shear-induced migration in flowing polymer solutions: Simulation of long-chain dna molecules*. Journal of Chemical Physics **120**, 2513 (2004).

[55] A. Mohan and P. S. Doyle. *Unraveling of tethered polymer chain in uniform solvent flow*. Macromolecules **40**, 4301 (2007).

[56] C. Gonzalaez-Perez and B. Henderson-Sellers. *Metamodelling for Software Engineering* (John Wiley and Sons, 2008).

[57] M. Benke, E. Shapiro, and D. Drikakis. *Falco - fast linear corrector for modelling dna-laden flows*. In *ASME ICNMM 2008, 6th International Conference on Nanochannels, Microchannels and Minichannels* (2008).

[58] S. Smith, L. Finzi, and C. Bustamante. *Direct mechanical measurements of the elasticity of single dna molecules by using magnetic beads*. Science **271**, 1122 (1992).

[59] S. Smith, Y. Cui, and C. Bustamante. *Overstretching b-dna: the elastic response of individual double-stranded and single-stranded dna molecules*. Science **271**(5250), 795 (1996).

[60] C. Bustamante, J. F. Marko, E. Siggia, and S. Smith. *Entropic elasticity of λ - phage dna*. Science **265**, 1599 (1994).

[61] C. Bustamante, S. Smith, J. Liphard, and D. Smith. *Single-molecule studies of dna mechanics*. Current opinion in structural biology **10**, 279:285 (2000).

[62] T. T. Perkins, S. R. Quake, D. E. Smith, and S. Chu. *Relaxation of a single dna molecule observed by optical microscopy*. Science **264**, 822 (1994).

[63] G. Bao. *Mechanics of biomolecules*. Journal of Mechanics and Physics of Solids **50**, 2237 (2002).

[64] P. T. Underhill and P. S. Doyle. *On the coarse-graining of polymers into bead-spring chains*. Journal of Non-Newtonianl Fluid Mechanics **122**, 3 (2004).

[65] E. S. G. Shaqfeh. *The dynamics of single-molecule dna in flow*. Journal of Non-Newtonian Fluid Mechanics **130**, 1 (2005).

[66] T. T. Perkins, D. E. Smith, and S. Chu. *Single polymer dynamics in an elongational flow*. Science **276**, 2016 (1997).

[67] R. G. Larson, T. T. Perkins, D. E. Smith, and S. Chu. *Hydrodynamics of a dna molecule in a flow field*. Physical Review E **55**, 1794 (1997).

[68] R. B. Bird, O. Hassager, R. C. Armstrong, and C. F. Curtiss. *Dynamics of polymeric liquids, Vol 2* (John Wiley & Sons, 1977).

[69] B. H. Zimm. *Dynamics of polymer molecules in dilute solution: viscoelasticity, flow birefringence and dielectric loss*. The Journal of Chemical Physics **24**, 269 (1956).

[70] M. Somasi, B. Khomami, N. J. Woo, J. S. Hur, and E. G. Shaqfeh. *Brownian dynamics simulations of bead-rod and bead-spring chains: numerical algorithms and coarse-graining issues*. Journal of Non-Newtonian Fluid Mechanics **108**, 227 (2002).

[71] R. G. Larson, H. Hu, D. E. Smith, and S. Chu. *Brownian dynamics simulations of a dna molecule in an extensional flow field*. Journal of Rheology **43**, 267 (1999).

[72] P. T. Underhill and P. S. Doyle. *Accuracy of bead-spring chains in strong flows*. Journal of Non-Newtonian Fluid Mechanics **145**, 109 (2007).

[73] R. G. Larson. *Principles for coarse-graining polymer molecules in simulations of polymer fluid mechanics*. Molecular Physics **102**(4), 341 (2004).

[74] D. Drikakis, P. Govatsos, and D. Papantonis. *A characteristic-based method for incompressible flows*. International Journal for Numerical Methods in Fluids **19**, 667 (1994).

[75] E. Shapiro and D. Drikakis. *Artificial compressibility, characteristics-based schemes for variable density, incompressible, multi-species flows. part i. derivation of different formulations and constant density limit*. J. Comp. Phys. **210(2)**, 584 (2005).

[76] D. Drikakis, O. Iliev, and D. Vassileva. *A nonlinear multigrid method for the three-dimensional incompressible Navier-Stokes equations*. Journal of Computational Physics **146**(1), 301 (1998).

[77] E. Shapiro and D. Drikakis. *Non-conservative and conservative formulations of characteristics-based numerical reconstructions for incompressible flows*. Int. J. Num. Meth. Eng. **66(9)**, 1466 (2006).

[78] D. Drikakis, E. Schreck, and F. Durst. *Performance analysis of viscous flow computations on various parallel architectures*. ASME Journal of Fluids Engineering **116**, 835 (1994).

[79] D. Drikakis. *A parallel multiblock characteristic-based method for 3d incompressible flows*. Advances in Engineering Software **26**, 111 (1996).

[80] D. Drikakis and S. Tsangaris. *On the solution of the compressible navier-stokes equations using improved flux vector splitting methods*. Applied Mathematical Modeling **17**, 283 (1993).

[81] D. Drikakis and S. Tsangaris. *Multigrid scheme for the compressible euler equations*. Journal of Applied Mathematics & Mechanics (Zeitschrift fÃ¼r Angewandte Mathematik Mechanik; ZAMM) **70**, 619 (1990).

[82] J. B. Bell, P. Colella, and H. M. Glaz. *A second-order projection method of the incompressible Navier-Stokes equations*. Journal of Computational Physics **85**, 257 (1989).

[83] S. V. Patankar and D. B. Spalding. *A calculation procedure for heat, mass and momentum transfer in three-dimensional parabolic flows*. International Journal of Heat Mass Transfer **15**, 1787 (1972).

[84] A. Chorin. *A numerical method for solving incompressible viscous flow problems*. Journal of Computational Physics **2**, 12 (1967).

[85] J. P. Ryckaert, G. Ciccotti, and H. J. C. Berendsen. *Numerical integration of the cartesian equations of motion of a system with constraints: Molecular dynamics of n-alkanes*. J. Comput. Phys. **23**, 327 (1977).

[86] H. Goldstein. *Classical mechanics* (Addison-Wesley,, 1959).

[87] L. Zhu and C. S. Peskin. *Simulation of a flapping flexible filament in a flowing soap film by the immersed boundary method*. Journal of Computational Physics Fluids **179**, 452 (2002).

[88] W. H. Press, S. A. Teukolsky, W. T. Vetterling, and B. P. Flannery. *Numerical Recipes in Fortran* (Cambridge, 1986).

[89] R. Rubinstein. *Simulation and the Monte Carlo method* (John Wiley & Sons, 1981).

[90] M. Benke, E. Shapiro, and D. Drikakis. *An efficient multi-scale model approach for ssdna motion in fluid flow*. Journal of Bionic Engineering **5**, 299 (2008).

[91] J. Happel and H. Brenner. *Low Reynolds number hydrodynamics* (Hague : Martinus Nijhoff Publishers, 1983).

[92] L. V. Tothova J., Brutovsky B. *Addendum to "monomer motion in single- and double-stranded dna coils"*. arXiv: cond-mat/0509399 (2005).

[93] M. Braun. *Differential equations and their applications* (Springer-Verlag, 1975).

[94] D. Stein, F. H. J. van der Heyden, W. J. A. Koopmans, and C. Dekker.

Pressure-driven transport of confined dna polymers in fluididc channels. PNAS **103**, 15853 (2006).

[95] G. K. Batchelor. *The stress generated in a non-dilute suspension of elongated parcles by pure straining motion*. Journal of Fluid Mechanics **46**, 813 (1971).

[96] P. K. Wong, Y. K. Lee, and C. M. Ho. *Deformation of dna molecules by hydrodynamic focusing*. Journal of Fluid Mechanics **497**(497), 55 (2003). Cited By (since 1996): 20.

[97] D. E. Smith, T. T. Perkins, and S. Chu. *Dynamical scaling of dna diffusion coefficients*. Macromolecules **29**, 1372 (1996).

[98] R. M. Jendrejack, J. J. de Pablo, and M. D. Graham. *Stochastic simulations of dna in flow: Dynamics and the effects of hydrodynamic interactions*. Journal of Chemical Physics **116**, 7752 (2002).

[99] C.-C. Hsieh, L. Li, and R. G. Larson. *Modeling hydrodynamic interaction in brownian dynamics simulations of extensional flows of dilute soultions of dna and polystyrene*. Journal of Non-Newtonian Fluid Mechanics **113**, 147 (2003).